Shock wave propagation in composites and electro-thermomechanical coupling of ferroelectric materials

Thesis by
Vinamra Agrawal

In Partial Fulfillment of the Requirements for the
Degree of
Doctor of Philosophy

CALIFORNIA INSTITUTE OF TECHNOLOGY
Pasadena, California

2016
Defended May 20, 2016

Vinamra Agrawal
ORCID: 0000-0002-1698-1371

ACKNOWLEDGEMENTS

First, I would like to thank my advisor Prof. Kaushik Bhattacharya for his guidance, support and many insightful discussions over the years. Prof. Bhattacharya has been a great mentor. I learned a lot about doing research, choosing problems and asking good questions. I am very thankful to Prof. Gurswami Ravichandran for being the chair of my thesis advisory committee and for many fruitful discussions throughout the course of my graduate studies. I am also thankful to Prof. Ravichandran for his guidance and advice at critical points of my career. I would like to thank Prof. Chris Lynch for his useful insights on the behavior of ferroelectric materials, experimental observations and challenges associated with conducting experiments on ferroelectric materials. I would also like to thank Prof. Dennis Kochmann for always taking the time to meet with me, giving valuable advice and feedback during the final years of my graduate studies. I am very grateful to Prof. Nadia Lapusta for being on my thesis committee and providing valuable feedback on my work.

Being a member of Prof. Bhattacharya's group has been a great learning experience. I especially enjoyed the joint Kaushik-Ravi group meetings and the discussions on diverse topics such as mechanics of materials, pure and applied mathematics, applied physics, experimental techniques and computational methods. I would like to thank the past and present members of Prof. Bhattacharya and Prof. Ravichandran's research group: Mauricio Ponga, Likun Tan, Zubaer Hossain, Owen Kingstedt, Xin (Cindy) Wang, Srivatsan Hulikal, Lincoln Collins, Dingyi Sun, Paul Plucinsky, Jin Yang, Paul Mazur, Chun-Jen (Ren) Hsueh, Mike Rauls, Louisa Avellar and others for many helpful discussions, and for their support and friendship.

I had the privilege of becoming friends with many loving and exceptionally brilliant people during my time at Caltech. I would like to thank Gaurav Sinha for his friendship and our countless discussions over the years on mathematics, computer science, physics, mechanics, politics, movies and other aspects of life. Along the same lines, I would like to thank Vikas Trivedi for his friendship and support. I also want to thank Likun Tan, Brandon Runnels, Xin (Cindy) Wang and Charles Wojnar for their friendship and valuable discussions over the years.

I was extremely fortunate to have become a part of the Los Angeles chapter of the National Stuttering Association. I would like to thank Prof. Gail Lew who helped me work on my stuttering over the years. I want to thank all the people I met through

the National Stuttering Association, past and current members of my chapter and my friends John Gomez, Josh and Jen Marcus for their love and support.

Finally and most importantly, I am indebted to my parents and my brother for their unconditional love and support throughout my undergraduate and graduate studies.

ABSTRACT

How is material behavior at the macro scale influenced by its properties and structure at the micro and meso-scales? How do heterogeneities influence the properties and the response of a material? How does nonlinear coupling of electro-thermo-mechanical properties influence the behavior of a ferroelectric material? How can design at the micro-scale be exploited to obtain selective response? These questions have been topics of significant interest in the materials and mechanics community. Recently, new materials like multifunctional composites and metamaterials have been developed, targeted at selective applications. These materials find applications in areas like energy harvesting, damage mitigation, biomedical devices, and various aerospace applications. The current thesis explores these questions with two major thrusts: (i) internal reflects of shocks in composite media and (ii) shocks in ferroelectric media.

Under the application of high-pressure, high strain rate loading, such as during high velocity impact, shock waves are generated in the material. They can cause the material to achieve very high stress states, and if transmitted without mitigation, can lead to failure of key components. An important question here is 'Can we design materials which can successfully mitigate damage due to shocks?' In a heterogeneous material, like a layered composite, the traveling waves undergo scattering due to internal reflections. In order to understand internal reflections, an idealized problem that focuses on nonlinear shocks and ignores less important elastic waves was formulated and studied in detail. The problem is studied by classifying all possible interactions in the material and then solving corresponding Riemann problems. Using dynamic programming tools, a new algorithm is designed that uses these solutions to generate a complete picture of the impact process. Different laminate designs are explored to study optimal design, by varying individual layer properties and their arrangement. Phenomena like spallation and delamination are also investigated.

Upon high strain rate loading, ferroelectric materials like lead zirconate titanate (PZT) undergo ferroelectric to anti-ferroelectric phase transition leading to large pulsed current output. These materials have thus found applications as pulsed power generators. The problem of shock induced depolarization and the associated electro-thermo-mechanical coupling of ferroelectric materials is studied in this thesis using theoretical and numerical methods. A large deformation dynamic analysis of such

materials is conducted to study phase boundary propagation in the medium. The presence of high electrical fields can lead to formation of charges in the material, such as surface charge on the phase boundary. Using conservation laws and the second law of thermodynamics, a set of governing equations are formulated that dictate the phase boundary propagation in isothermal and adiabatic environments. Due to the possibility of surface charges on the phase boundary, the curvature of the phase boundary starts to play a role in the driving force acting on the phase boundary. The equations of motion and driving force see the contribution of nonlinear electro-thermomechanical coupling in the material. Using the equations derived, a canonical problem of impact on a ferroelectric material is studied. A new finite-volume, front-tracking method is developed to solve these equations. Finally, results from numerical simulations are compared to the experimental results.

PUBLISHED CONTENT AND CONTRIBUTIONS

[1] Vinamra Agrawal and Kaushik Bhattacharya. “Impact induced depolarization and electro-thermomechanical coupling of ferroelectric materials”. In: (2016). (To be submitted).

[2] Vinamra Agrawal and Kaushik Bhattacharya. “Shock wave propagation through a model one dimensional heterogeneous medium”. In: *International Journal of Solids and Structures* 51.21–22 (2014), pp. 3604–3618. ISSN: 0020-7683. DOI: http://dx.doi.org/10.1016/j.ijsolstr.2014.06.021. URL: http://www.sciencedirect.com/science/article/pii/S0020768314002534.

TABLE OF CONTENTS

Acknowledgements . . . iii
Abstract . . . v
Published Content and Contributions . . . vii
Table of Contents . . . viii
List of Illustrations . . . ix
List of Tables . . . xiv
Chapter I: Introduction . . . 1
1.1 Shock waves in heterogeneous materials . . . 2
1.2 Shock waves and phase transitions . . . 4
1.3 Outline of thesis . . . 5
Chapter II: Fundamentals of shock waves . . . 7
2.1 Governing equations . . . 7
2.2 Plate impact . . . 8
2.3 Hugoniot curves . . . 10
2.4 Scattering and structured shock waves . . . 12
Chapter III: Shock wave scattering in layered materials . . . 21
3.1 Problem Description . . . 21
3.2 Governing equations . . . 22
3.3 Shock wave interaction at a material interface . . . 25
3.4 Semi-infinite medium . . . 28
3.5 Finite heterogeneous medium: Method . . . 28
3.6 Finite heterogeneous medium: Results . . . 37
3.7 Extensions and relaxing assumptions . . . 49
3.8 Conclusions and discussions . . . 51
Chapter IV: Pulsed power generation in ferroelectric medium . . . 55
4.1 Ferroelectric materials and pulsed power generation . . . 55
4.2 Continuum formulation . . . 61
4.3 Simplified one-dimensional analysis . . . 76
4.4 Shock wave propagation in ferroelectric materials . . . 78
4.5 Conclusions . . . 101
Chapter V: Summary and future directions . . . 104
Bibliography . . . 107

LIST OF ILLUSTRATIONS

Number *Page*

1.1 Different material response under different loading regimes. The general domain for shock waves is shown inside the red circle. 2

1.2 Examples of heterogeneous materials. From left to right: concrete core, polycrystalline steel and sand from Gobi desert 3

2.1 Schematic of plate impact experimental setup. Flyer plate is launched at high speeds through the launch tube. Particle velocity measurements are done on the right end of the target through laser interferometry. 9

2.2 Schematic of shock transition states across a propagating shock. . . . 10

2.3 $\sigma - v$ Hugoniot for Aluminum 2024 alloy (material constants taken from [23]). The states S^+ and S^- are connected by a Rayleigh line R. The slope of the Rayleigh line can be used to obtain the speed of the shock. 11

2.4 $\sigma - v$ Hugoniot for Aluminum 2024 alloy. 12

2.5 $U_s - v$ Hugoniot for Aluminum 2024 alloy. 13

2.6 (a) Shock waves are idealized as moving discontinuity. However, a smooth, structured profile is observed (depicted in bold red) in experiments. The shock is preceded by an elastic precursor traveling at speed U_e. (b) Modified $\sigma-\epsilon$ Hugoniot curve to depict the Hugoniot Elastic Limit (HEL). The response is linear till σ_{HEL} is achieved. . . 14

2.7 Schematic of the experimental setup used by Zhuang [89]. Particle velocity profiles were captured for different combination of impact speeds, layer thickness, material, layer arrangement and number of layers. 15

2.8 (a) Variation of particle velocity profiles with impedance mismatch in the periodic laminate. The impedance mismatch in PC74/Al37 is lesser than PC74/SS37, which means that shock is transmitted better in PC74/Al37. As such the profile is steeper in this case. (b) Variation of particle velocity profiles with number of interfaces in the laminate. The profile with more interfaces has more ripples corresponding to more scattering in the system. The profile steepens due to inherent nonlinearity in the system [89]. 16

2.9 Schematic of the experimental setup used by Rauls [65]. A powder gun accelerates an Aluminum impact to impact a two phase composite specimen. Measurements were done using PDV at the right end of the target. 17
2.10 A cross section of the two phase composite sample used in [65] made from PMMA matrix and glass beads as inclusions 18
2.11 Particle velocity profiles for bead size (a) 100 μm and (b) 1000 μm for 40% volume fraction. Profiles are measured at three points of the sample to account for spatial heterogeneity. The profile for 1000 μm beads has less steep slope with rounded structures towards the leading and trailing edges of the shock. Additionally, the overshock is greater for the 100 μm bead size due to greater number of beads, hence greater number of interfaces, leading to contributions from secondary reflections. 19
3.1 Schematic representation of plate impact 22
3.2 (a) Illustration of elastic and shock waves in the stress-strain curve. The difference between the areas P3Q and P21 denotes the dissipation across the shock front. 24
3.3 (a) $X - t$ diagram for the shock interaction problem at the A-B material interface. The impinging shock U_A interacts with the material interface to produce the elastic waves and a shock U_B. 25
3.4 Schematic diagram of the elastic wave interaction at A-B interface . . 30
3.5 Elastic wave interaction leading to a compression shock 31
3.6 Elastic wave interaction leading to an unloading shock 31
3.7 Compression shock wave entering a purely elastic material 32
3.8 Compression shock wave entering a purely elastic material 32
3.9 Unloading shock wave entering another piecewise affine material . . 33
3.10 Interaction of elastic wave with compression shock 34
3.11 Interaction of elastic wave and compression shock traveling in opposite directions resulting in two possible solutions - (b) unloading shock wave and (c) compression shock wave. 34
3.12 Interaction of two elastic waves forming a pair of unloading shocks . 35
3.13 Interaction of two elastic waves forming a pair of compression shocks 35
3.14 Interaction of two compression shock waves forming a pair of elastic waves 36

3.15 Interaction of two elastic waves forming a compression shock in the piecewise affine layer 37
3.16 Interaction of two elastic waves forming a compression shock in the piecewise affine layer 37
3.17 Impact problem for $L_0 = 1m$ and ε_c decreasing linearly. (a) $X - t$ diagram of the impact problem. The red lines correspond to the elastic waves while the black line is the propagating shock wave. (b) Particle velocity profiles at $X = 0$ (left edge of the flyer), $X = 1$ (flyer-target interface) and $X = 2$ (right edge of the target). (c) Stress profile at the flyer-target interface. The sudden drop in stress denotes the arrival of the release wave from the free edge of the flyer. 39
3.18 Impact problem for $L_0 = 1m$ and ε_c increasing linearly. (a) $X - t$ diagram of the impact problem. (b) Particle velocity profiles at $X = 0$ (left edge of the flyer), $X = 1$ (flyer-target interface) and $X = 2$ (right edge of the target). (c) Stress profile at the flyer-target interface. The sudden drop in stress denotes the arrival of the release wave from the free edge of the flyer. 40
3.19 Variation of arrival times T with number of layers N for different layer profiles 41
3.20 Variation of particle velocity profile at the free edge of the target with N for an alternate linear and nonlinear material. The first layer is chosen to be nonlinear with (a) $\varepsilon_2 = 0.2$ and (b) $\varepsilon_c = 0.6$. 42
3.21 Variation of particle velocity profiles with N for (a) linearly decreasing and (b) linearly increasing ε_c profile. Profiles for constant $\varepsilon_c = 0.2, 0.6$ are plotted for comparison. 44
3.22 Variation of particle velocity profiles with the exponent n for (a) ε_c decreasing and (b) ε_c increasing profiles. 45
3.23 Variation of particle velocity profiles with λ for (a) ε_c decreasing and (b) ε_c increasing profiles. 46
3.24 Variation of particle velocity profiles with N for alternate layering of (a) $\varepsilon_c = 0.6$ and 0.2 (b) $\varepsilon_c = 0.2$ and 0.6. 47
3.25 $X-t$ diagram for the impact process on a layered target with (a) $N = 2$ and (b) $N = 20$, where the ε_c increases linearly for both cases. A pair of tensile shocks is observed in both cases, with stronger shocks for $N = 2$. 48

3.26 Variation of total dissipation in the material with N for different ε_c arrangement. The flyer length is chosen to be large to avoid the effect of release waves. The dissipation is higher for the layer arrangement with ε_c decreasing linearly along the length. 49
3.27 Potential solutions for initial impact on a layered composite with the modified piecewise affine stress-strain curve. For small impact speeds, the maximal dissipation kinetics ensures (a), (b) a two wave structure. For high impact speeds (c), (d) a single shock wave is sufficient for a unique solution. 50
4.1 Characteristic curve of a ferroelectric material. At zero electric field, the material exhibits a non-zero polarization ($\approx 33\,\mu C/cm^2$ in this case). 56
4.2 (a) Experimental setup for loading a PZT sample hydrostatically, and measuring $D - E$ loops. (b) Variation in the characteristic curve of a ferroelectric material upon application of hydrostatic pressure (Figures from [78]). 57
4.3 Schematic of ferroelectric generators providing shock loading to the material through (a) plate impact and (b) blast loading 58
4.4 (a) Schematic of the experimental setup used by Furnish et al. [34]. (b) Charge profiles obtained through the external circuit. The numbers on top of the individual profiles denote different experimental runs. Parameters for each experimental run are available in [34]. . . . 60
4.5 Continuum representation of the problem. The material is subjected to a generalized electromechanical loading in the deformed frame. A phase boundary propagates causing FE-AFE phase transition. 61
4.6 Schematic of the canonical uniaxial impact problem. A phase boundary propagates in a one dimensional system after being impacted by a flyer. The two ends of the ferroelectric material are connected through a resistor R. Current flowing through R is tracked. 79
4.7 (a) H_ε energy landscape of the ferroelectric material. The energy wells change based on temperature, but ε_T is unchanged. (b) Schematic of Cauchy stress σ_c profile for the ferroelectric material. . 81
4.8 (a) Riemann problem at the node $\tilde{x}_i$ other than at a phase boundary or at either of the ends of the material. The problem is solved keeping the temperature constant. (b) Temperature update at the node following conservation of energy equations. 85

4.9 (a) Riemann problem to be solved at the phase boundary. The speed of the phase boundary is also unknown. This is where the kinetic relation comes into equation. (b) Temperature update at the phase boundary. 87
4.10 (a) Conservation of momentum problem at the flyer target interface. (b) Temperature update using the conservation of energy equations. . 89
4.11 Schematic of the mesh update procedure [64]. As the phase boundary gets closer to a node, the node is removed and the mesh is resized. Once the phase boundary gets further away, the node is reinserted. . . 90
4.12 (a) Linear kinetic relation. (b) $X - t$ diagram of the impact problem. The colors correspond to the strain in the flyer and the ferroelectric target. The speed of the impact is 75 m/s. 93
4.13 (a) Current profile obtained flowing through the resistor R for an impact speed of 75 ms^{-1}. (b) $X - t$ diagram of the impact problem. The colors correspond to the temperature in the flyer and the ferroelectric target. 94
4.14 (a) Variation of current profile with increasing impact speeds. (b) Variation of current profiles with changing values of d_s for impact speed of 75 m/s. 95
4.15 (a) Variation of current profile with increasing impact speeds. (b) Variation of current profiles with changing values of d_s for impact speed of 75 m/s. 96
4.16 Variation of current profiles with R in the external circuit for the same impact speed 75 ms^{-1}. 96
4.17 (a) Combination of Stick-slip and Linear kinetic relation. (b) $X - t$ diagram of the impact problem. The colors correspond to the strain in the flyer and the ferroelectric target. The speed of the impact is 75 m/s. 97
4.18 (a) Comparison of current profiles for Linear and Stick-Slip Linear Kinetic relation. (b) $X - t$ diagram of the impact problem. The colors correspond to the temperature in the flyer and the ferroelectric target. 98
4.19 (a) Stick-exponential slip kinetic relation (b) Comparison of charge profiles from experiments and simulations 100
4.20 Shock speed vs Particle speed Hugoniot of the ferroelectric material for different R in the external circuit. The figure shows a clear difference between short-circuit and open-circuit case. 101

LIST OF TABLES

Number *Page*

4.1 Choice of ferroelectric material parameters 91
4.2 Choice of flyer material parameters 91
4.3 Choice of parameters in setting up the problem 91
4.4 Setup and material parameters in experiments by Furnish [34] 99
4.5 Choice of material and setup parameters for simulations 99
4.6 Variation of Hugoniot parameters of the ferroelectric material for different values of R in the external circuit. The Hugoniot, and hence the material behavior, shows strong dependence on the external circuit which is consistent with experimental observations. 101

Chapter 1

INTRODUCTION

High velocity impacts are very common in nature as well as day to day life. For example, in an automobile accident, the structural elements of the vehicle undergo very rapid loading and large deformations. The impact speed involved, in an extreme case, is around 60 ms^{-1} with pressures reaching up to 1 GPa in a time frame of a few milliseconds. Another very important scenario is that of a bird strike on an airplane. In this case, the impact happens at speeds of the order of 100 ms^{-1}, and can cause tremendous damage to life and property. Moving towards military and defense scenarios, the pressure and time scales involved can be orders of magnitude different. A ballistic impact or a blast loading involve loading speeds up to $1-5$ kms^{-1} and $6-10$ kms^{-1} with pressure increase ranging from $1-10$ GPa within a few microseconds. The pressure increase and impact speeds typically increase as the applications move away from earth and into space. Orbital debris is present at various altitudes, with sizes ranging from $1-10$cm. The debris can achieve speeds greater than 10 kms^{-1}. Dealing with orbital debris has proven to be a major challenge, and many objects of size larger than 5 cm are tracked to avoid any possible collisions. Impact involving small astronomical objects, such as small meteorites, can happen at speeds of up to 10 kms^{-1}, while an impact involving larger astronomical objects can happen at speeds of up to $20-50$ kms^{-1}.

High velocity impact leads to high pressures and high strain rates, and this in turn can lead to shock waves. Figure 1.1 shows a schematic of different material responses over a range of applied pressure and strain rate loading. The loading regime for shock behavior is circled in red. Under shock loading, the material experiences extreme environments undergoing large temperature and pressure changes over a very short period of time. If these waves are left to travel unmitigated, they can cause significant damage in the material.

Due to such broad applications, understanding material behavior in high strain rate conditions is very important. Studies pertaining to shock waves in solids started during the early 1900s, and generated significant interest during the 1940s and 1950s because of numerous military applications. In order to characterize and predict material response in highly dynamic situations, many experimental, theoretical

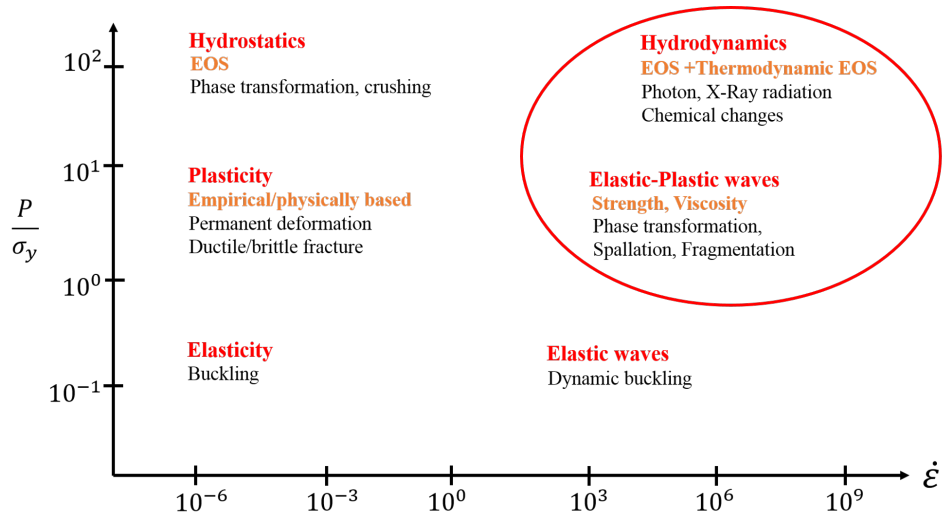

Figure 1.1: Different material response under different loading regimes. The general domain for shock waves is shown inside the red circle.

and numerical investigations have been undertaken. Over the years, the focus of investigation has expanded from metals and metallic alloys to ceramics, polymers, composites and even soft materials. Further, the focus has also expanded from studying just wave interactions to understanding shock induced chemical changes, phase transformations, metallurgical defects and fragmentation.

1.1 Shock waves in heterogeneous materials

Heterogeneous materials cover a broad spectrum of materials such as composites, polycrystalline materials, polymers, etc. In fact, except for perfect single crystals, every material is heterogeneous at some length scale. Composite materials are now widely used due to their superior effective properties over their constitutive materials. For example, concrete - a two phase composite with matrix and inclusions - is a common structural material with high compression strength and low thermal expansion coefficient. Kevlar is another such example of a composite which has found wide applications ranging from armors to durable tires because of its high tensile-strength-to-weight ratio. Polycrystalline materials like steel have found applications in automotive and structural industries due to their broad range of yield stress and elastic modulus depending on different manufacturing processes. The manufacturing processes essentially control the microstructure such as grain size and orientation in the material. Sand is another class of heterogeneous materials with many different compositions, granular structures and grain distributions depending upon the geographical location of occurrence. It is being used in applications ranging from

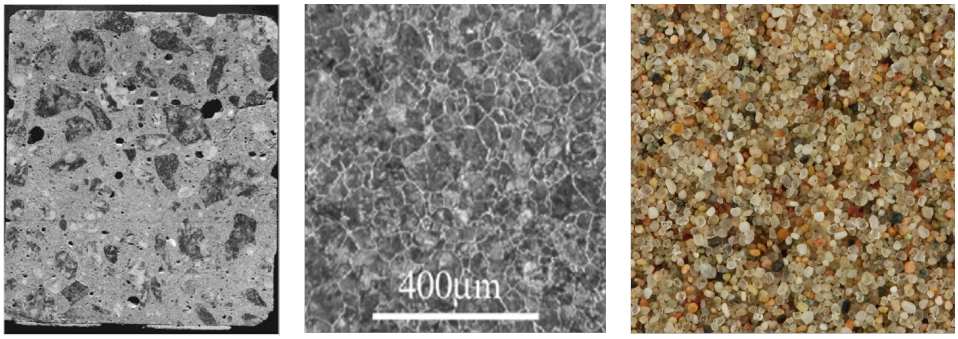

Figure 1.2: Examples of heterogeneous materials. From left to right: concrete core, polycrystalline steel and sand from Gobi desert

defense to agriculture and construction.

Due to such widespread applications, it is important to understand shock behavior of heterogeneous materials and the role of heterogeneity in the response. Wave propagation in heterogeneous materials has been a topic of interest in the community for many decades. Most of the work in the early years had been focused on wave dispersion of small amplitude waves in linear elastic periodic materials [74], [61]. Experiments conducted by Barker and others [13] on periodic laminates showed exponential decay of stress waves with distance to achieve a structured steady profile above a critical stress amplitude. Other experiments [50], [63] on layered materials show resonance phenomena. In recent years, many shock studies have been conducted on heterogeneous materials to understand the role of heterogeneity (see [29], [65], [80], [81], [89] and references therein).

Much less is known regarding the theoretical side of shock wave propagation in heterogeneous materials. The formation of structured shock waves was studied extensively in homogeneous metals ([75], [58]) and the primary mechanism was attributed to viscoelastic and viscoplastic behavior of these materials. These theoretical models worked very well in predicting the steady shock width in metals. For heterogeneous materials, Grady [35] presented scattering of nonlinear waves as an alternate explanation for structured waves. The complexity of the physics behind wave propagation in a heterogeneous material can be illustrated by looking at the interplay between the length scale of heterogeneity and the shock width and the associated response. The following equation

$$\rho(x)u_{tt} = \left(\sigma\left(u_x, \frac{x}{h}\right)\right)_x - \gamma\left(\frac{x}{h}\right) u_{xxxx} + \nu\left(\frac{x}{h}\right) u_{xxt}\,, \tag{1.1}$$

represents a one-dimensional augmented wave equation for a heterogeneous material [3]. Here ρ, u, γ and ν represent density, displacement, coefficient for strain gradient

and coefficient of viscosity of the material. It can be seen from the above equation that there are two length scales in the problem - size of the heterogeneity h and the width of the wave $l = \sqrt{\gamma/\rho}$. The asymptotic behavior can be summarized as follows:

1. $l \gg h$: In this case, the wave width is much larger than the size of the heterogeneity. As such, the wave sees an effective environment as it propagates through the medium [76].

2. $l \ll h$: In this case, the wave width is much smaller than the sixe of the heterogeneity. Here, as the wave propagates, it sees material interfaces and different material environments across the interface and reacts accordingly. Here the motion is dominated by reflections and scattering.

In the first half of this thesis the phenomena of scattering ($l \ll h$) of shock waves is explored. A canonical problem of plate impact on a layered, not necessarily periodic, material is taken into consideration. The layered material is impacted upon by a flyer traveling at high speed. The fundamental problems such as wave-wave interaction and wave-interface interaction are studied to develop an overall picture of shock wave propagation.

1.2 Shock waves and phase transitions

Under shock loading, the ground state of a material can be driven from one energy minimum to another, resulting in dynamic crystal reorientation over a short period of time. The process of shock induced phase transitions in metals has been extensively studied, including nucleation and kinetics (see [56], [28], [8], [33], [43] and references therein). In case of special materials like ferroelectric and ferromagnetic materials, characterized by a strong nonlinear electro-magneto-thermomechanical coupling, shock loading can induce electrical or magnetic phase transitions. This phase transition is accompanied by large pulse of power under certain electromagnetic boundary conditions. As such, these materials have found applications as pulsed power generators [7]. In this thesis the focus will be placed on ferroelectric materials. It should be noted that, at a continuum level, the analysis for ferromagnetic materials proceeds in a similar fashion.

Experimental investigations into the dynamic loading behavior of ferroelectric materials date back to 1959 [14]. Since then many experimental studies have been conducted ([37], [21], [52], [54], [27], [34], [69] and others) to further understand

the shock response of these materials under different configurations and boundary conditions. Plate impact experiments have been a standard method for these experiments due to their ease of setup and control over various parameters. Almost all studies are conducted on either axially poled, normally poled or unpoled samples. The poling configuration corresponds to the alignment of polarization direction with the direction of loading. It has also been found that behavior is different under short-circuit and open-circuit boundary conditions. Further, experiments have been conducted for different compositions of Lead Zirconate Titanate (PZT) specimens, and it has been found that PZT 95/5 doped with 2% Niobium can be depolarized at low shock speeds.

While there are many experimental studies, relatively less is known about the theoretical aspects of shock induced phase transitions and power generation. In this thesis, the theoretical aspects of shock induced phase transitions in a ferroelectric material are studied.

1.3 Outline of thesis

This work is organized as follows. Chapter 2 covers the fundamentals of shock wave propagation. A detailed derivation of governing equations for the motion of a jump surface (across which quantities like deformation gradient, traction, particle velocity, etc. are discontinuous) is presented. A brief introduction and description of the standard plate impact experiment is provided along with the simplification it brings to the analysis. The idea of Hugoniot curves is introduced next and the well known linear shock speed - particle speed relationship is discussed. Finally, a detailed discussion on scattering and the formation of structured shock waves is presented.

Chapter 3 deals with a canonical problem of a plate impact on a model layered, not necessarily periodic, material. In order to deal with only Riemann problems, the Hugoniot is approximated by a piecewise linear stress-strain curve. A maximally dissipative kinetic relation is introduced to obtain a unique solution. This can also be seen as an equivalent relation to Lax entropy criteria in shocks. The complex wave problem is broken down into classes of fundamental interactions and analytical solutions are obtained for each of these classes. These solutions are then stitched together to obtain a complete picture of the wave propagation. Next, a broad parameter study is conducted to study the influence of material interfaces, layer arrangement, layer properties, target length, flyer length, etc. Finally, comments are

made on the optimal design of a material for shock attentuation.

In chapter 4, shock wave propagation in a ferroelectric material is studied. Ferroelectric materials under shock loading undergo ferroelectric to antiferroelectric phase transition to produce a large pulsed power output. The nonlinear electro-thermomechanical coupling of ferroelectric material plays a central role in this process. A continuum analysis for large deformation dynamic behavior of a ferroelectric material is presented. Governing equations as well as an expression for driving force acting on the phase boundary are derived using conservation laws, Maxwell equations and the second law of thermodynamics. Next, the canonical problem of plate impact on a ferroelectric material is studied. Numerical simulations are conducted to study the current output through the resistance R in the external circuit. Finally current profiles are compared with experiments and the shock-speed particle-speed Hugoniot of the material is generated for short and open circuit boundary conditions.

Chapter 2

FUNDAMENTALS OF SHOCK WAVES

In this chapter, the basic theory behind shock waves will be presented, which will be useful in subsequent chapters. For detailed derivations and interpretation the reader is directed to [23] and [10] and the references therein. Ideally, shock waves are characterized as a moving discontinuity of stresses, strains, density, particle velocity, temperature, etc.

2.1 Governing equations

In this section, equations and jump conditions that govern the motion of a body under large dynamic deformation with a propagating phase boundary are derived. For reference, this derivation can be found in [2].

Consider a deformation map $\mathbf{y}(\mathbf{x}, t)$ mapping a body B in its reference configuration to its deformed configuration. The body also contains a propagating regular surface $S_0(t)$ across which different quantities might be discontinuous. This map is assumed to be continuous everywhere, but first and second derivatives can be discontinuous. The deformation gradient $\mathbf{F}$ and particle velocity are defined as $\mathbf{F}(\mathbf{x}, t) = \text{Grad}\, \mathbf{y}(\mathbf{x}, t)$ and $\mathbf{v}(\mathbf{x}, t) = \partial \mathbf{y}(\mathbf{x}, t)/\partial t$, where $\mathbf{x}$ refers to the coordinates in the reference frame. At any given point $\mathbf{x}$ in the reference frame, let $\rho(\mathbf{x})$ denote the density, $\mathbf{b}(\mathbf{x}, t)$ be the body force per unit mass and $\sigma(\mathbf{x}, t)$ be the nominal stress tensor. The integral form of conservation of linear and angular momentum in any arbitrary subdomain $D \subset B$ can be written as

$$\int_{\partial D} \sigma \hat{\mathbf{n}}\, dA + \int_D \rho \mathbf{b}\, dV = \frac{d}{dt} \int_D \rho \mathbf{v}\, dV, \tag{2.1}$$

$$\int_{\partial D} \mathbf{y} \times \sigma \hat{\mathbf{n}}\, dA + \int_D \mathbf{y} \times \rho \mathbf{b}\, dV = \frac{d}{dt} \int_D \mathbf{y} \times \rho \mathbf{v}\, dV. \tag{2.2}$$

Further, the conservation of energy for the arbitrary subdomain D can be written as

$$\int_{\partial D} \sigma \hat{\mathbf{n}} \cdot \mathbf{v}\, dA + \int_D \rho \mathbf{b} \cdot \mathbf{v}\, dV + \int_{\partial D} \mathbf{q} \cdot \hat{\mathbf{n}}\, dA + \int_D \rho r\, dV = \frac{d}{dt} \int_D \left(\rho \varepsilon + \frac{1}{2} \rho \mathbf{v} \cdot \mathbf{v} \right) dV, \tag{2.3}$$

where $\mathbf{q}(\mathbf{x}, t)$, $r(\mathbf{x}, t)$ and $\varepsilon(\mathbf{x}, t)$ denote the nominal heat flux vector, heat supply per unit mass and internal energy per unit mass respectively. Absolute temperature $\theta(\mathbf{x}, t)$ and entropy per unit mass $\eta(\mathbf{x}, t)$ can be used to calculate the rate of entropy

production as,

$$\Gamma_D(t) \coloneqq \frac{d}{dt}\int_D \rho\eta \, dV - \int_{\partial D} (\mathbf{q}\cdot\hat{\mathbf{n}}/\theta)\, dA - \int_D \rho r/\theta \, dV. \tag{2.4}$$

Here, θ is assumed continuous with piecewise continuous derivatives and η is piecewise continuous with piecewise continuous derivatives. The Clausius-Duhem inequality for arbitrary $D \subset B$ and for all time t enforces

$$\Gamma_D(t) \geq 0. \tag{2.5}$$

Next, Coleman-Noll type arguments can be implemented to localize the above equations to get following equations at any point not on $S(t)$.

$$\operatorname{Div}\sigma + \rho\mathbf{b} = \rho\dot{\mathbf{v}}, \tag{2.6}$$

$$\sigma\mathbf{F}^T = \mathbf{F}\sigma^T, \tag{2.7}$$

$$\sigma\cdot\dot{\mathbf{F}} + \operatorname{Div}\mathbf{q} + \rho r = \rho\dot{\varepsilon}, \tag{2.8}$$

$$\operatorname{Div}(\mathbf{q}/\theta) + \rho r/\theta \leq \rho\dot{\eta}. \tag{2.9}$$

Additionally, at any point on $S(t)$ the following jump equations can be obtained:

$$[\![\sigma\hat{\mathbf{n}}]\!] + \rho V_n [\![\mathbf{v}]\!] = 0, \tag{2.10}$$

$$[\![\sigma\hat{\mathbf{n}}\cdot\mathbf{v}]\!] + [\![\rho(\varepsilon + \mathbf{v}\cdot\mathbf{v}/2)]\!]V_n + [\![\mathbf{q}\cdot\hat{\mathbf{n}}]\!] = 0, \tag{2.11}$$

$$[\![\mathbf{q}\cdot\hat{\mathbf{n}}/\theta]\!] + [\![\rho\eta]\!]V_n \leq 0, \tag{2.12}$$

where $[\![\cdot]\!]$ denotes the jump in quantities across the surface $S(t)$. Further, $V_n = \mathbf{V}\cdot\hat{\mathbf{n}}$ is the normal velocity of $S(t)$, conventionally taken to be positive in the direction of the normal.

In addition to the above equations, certain kinematic compatibility equations are enforced across $S(t)$ to ensure continuity of $\mathbf{y}$. Let $\hat{\mathbf{t}}$ be the tangent vector at any point $S(t)$. The compatibility equations are given by

$$[\![\mathbf{F}]\!]\hat{\mathbf{t}} = 0, \tag{2.13}$$

$$[\![\mathbf{v}]\!] + V_n[\![\mathbf{F}]\!]\hat{\mathbf{n}} = 0. \tag{2.14}$$

2.2 Plate impact

The plate impact experiment is the most common and widely used method to investigate shock propagation in a material. The experiment involves accelerating a plate flyer to very high speeds and impacting it onto a plate target. Usually, the plates

are circular disks of very small thickness compared to their diameter. Measures are taken to ensure that the plates have smooth surfaces. This ensures that the impact is uniform and the momentum is transferred evenly to the target surface. Typical target thickness ranges from 1 mm to 1 inch. A typical setup for the plate impact experiment is represented in Figure 2.1.

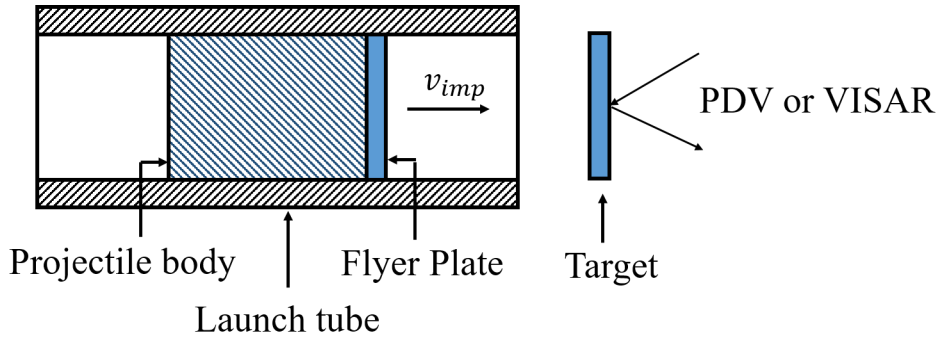

Figure 2.1: Schematic of plate impact experimental setup. Flyer plate is launched at high speeds through the launch tube. Particle velocity measurements are done on the right end of the target through laser interferometry.

Plate impact experiments are designed to produce uniaxial loading conditions from the moment of impact until the release wave from the left end (and typically the free end) of the flyer. Since shock experiments happen at very short time scales, there is no time for the system to exchange heat. This makes the plate impact experiments adiabatic. Further, there are no external volumetric heat sources. This means $\mathbf{q} = 0$ and $r = 0$. As such, the jump equations from Section 2.1 reduce to a set of one-dimensional equations as below:

$$[\![\sigma]\!] + \rho_0 U_s [\![v]\!] = 0, \tag{2.15}$$

$$[\![v]\!] + U_s [\![\epsilon]\!] = 0, \tag{2.16}$$

$$[\![\sigma v]\!] + \rho_0 U_s [\![\varepsilon + v^2/2]\!] = 0, \tag{2.17}$$

where ρ_0, ϵ, σ and U_s denote the reference density, uniaxial strain, uniaxial stress and the speed of the propagating shock. The schematic for shock transition states is represented by Figure 2.2. The states S^- and S^+ represent the state of the material before and after the shock wave has propagated. Typically the target is at rest in a stress-free state. Hence, $v^- = 0$, $\sigma^- = 0$ and $\epsilon^- = 0$. For reference, the energy state ε^- is taken to be zero.

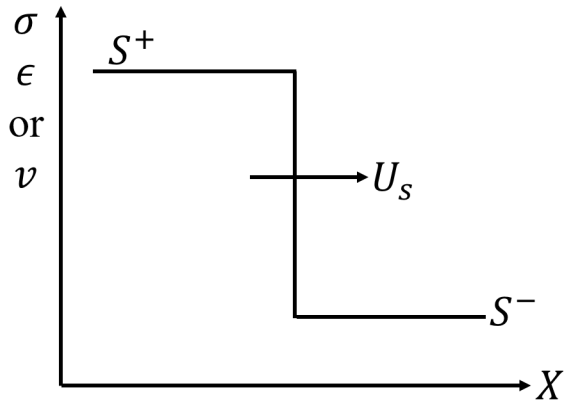

Figure 2.2: Schematic of shock transition states across a propagating shock.

2.3 Hugoniot curves

Shock jump equations (2.15)-(2.17) are not enough to completely determine the final states and the speed of the shock. Further, the equations do not contain material information to distinguish one material from another. If the state S^- in Figure 2.2 is kept fixed and stronger shocks are introduced in the system, a locus of states S^+ can be generated. This locus is called a *Hugoniot* centered around S^-. The Hugoniot, a characteristic curve of a material, contains the minimum amount of information required to solve the shock propagation problem to obtain the final state S^+. However, the Hugoniot curves do not provide the complete thermodynamical material description. This is where an equation of state (EOS) is needed. An EOS is a comprehensive material model that takes various thermodynamic parameters into account. As such, Hugoniot relations can be obtained from an EOS after mechanical and thermodynamical analysis. For a detailed review on various EOS and their analysis, the reader is referred to [23].

Given an initial state, the S^+ states σ, ϵ, v, ε and U_s together form 10 pairs of Hugoniot. In case of zero initial particle velocity and stress free state, the Hugoniot is called a *principal Hugoniot* curve. Using an EOS, Hugoniot centered around other initial states can also be determined. Due to ease of measurement, specific volume v is measured instead of strain. Among these, the mostly commonly used Hugoniot curves are $\sigma - v$, $\sigma - v$ and $U_s - v$ curves. The $\sigma - v$ curve provides valuable thermodynamic information about the material, the $\sigma - v$ relation provides direct measurements of stresses given particle velocity profiles obtained from experiments, and the $U_s - v$ relation enables direct measurement of propagating shock speed.

Figure 2.3 shows the $\sigma - v$ Hugoniot of Aluminum 2024 alloy. The stress strain

relation can be obtained from this by using $\epsilon = 1 - (v/v_0)$, where v_0 is the reference specific volume given by $v_0 = 1/\rho_0$. The line R connecting the states S^- and S^+ is called the Rayleigh line, the slope of which related to the speed of the shock U_s. This means that a faster shock would lead to steeper R and consequently higher stress states. Further, using (2.17), it can be shown that the area under the Rayleigh line in Figure 2.3 denotes the jump in specific internal energy of the material during the shock.

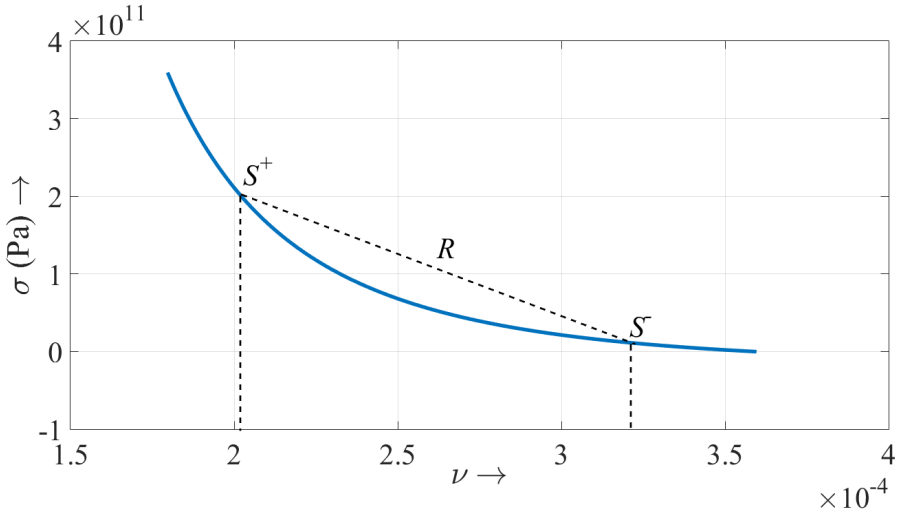

Figure 2.3: $\sigma - v$ Hugoniot for Aluminum 2024 alloy (material constants taken from [23]). The states S^+ and S^- are connected by a Rayleigh line R. The slope of the Rayleigh line can be used to obtain the speed of the shock.

Figure 2.4 shows the $\sigma - v$ Hugoniot curve for Aluminum 2024 alloy corresponding to the shock propagating in the $+x$ direction. This curve is becomes very useful while solving impact problems to directly obtain stress states. One of the most common observations of plate impact experiments is that the velocity of the shock is proportional to the particle velocity of the material upon impact. This observation is consistent with many solids over a wide range of impact speeds. These experiments are typically conducted at room temperature ($\sim 300K$) on unstressed sample with zero initial particle velocity. The linear law is given by

$$U_s = C + S\,v^+, \tag{2.18}$$

where C and S are material constants computed from the experiments. Typically, C is found to be close to the bulk sound speed in the material. S is a dimensionless constant which typically ranges from 1-2 for most materials. A list of Hugoniot curves of various materials and the associated constants is presented in [55]. Plugging

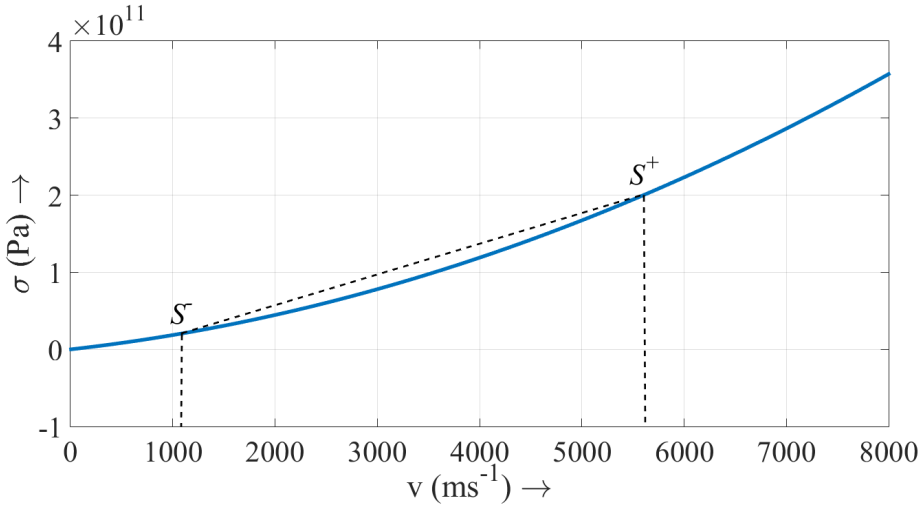

Figure 2.4: $\sigma - v$ Hugoniot for Aluminum 2024 alloy.

(2.18) into the jump equations (2.15) and (2.16) with reference initial conditions, we get

$$\sigma^+ = \frac{(\rho_0 C)^2 (v_0 - v^+)}{(1 - \rho_0 S(v_0 - v^+))^2}, \tag{2.19}$$

$$\sigma^+ = \rho_0 (C + S v^+) v^+. \tag{2.20}$$

Figure 2.5 shows the $U_s - v$ Hugoniot of Aluminum 2024 alloy, where the y-intercept corresponds to C. For Aluminum 2024, following values were used [55]

$$\rho_0 = 2785 \text{ kgm}^{-3}, \ C = 5328 \text{ ms}^{-1}, \ S = 1.338. \tag{2.21}$$

2.4 Scattering and structured shock waves

Although shock waves are ideally characterized as moving discontinuities, it has been observed that they have a structure. The stress states, instead of being discontinuous, vary smoothly and sharply over a small region connecting S^+ and S^-. This is represented in Figure 2.6a by Δx. Further, the shock wave is preceded by an elastic precursor traveling at speed U_e. This means the Hugoniot response doesn't kick in until a threshold state is achieved. Formally this means that the $\sigma - v$ Hugoniot curve is preceded by a linear relation which is valid up to a certain limit as shown in Figure 2.6b. This is called the Hugoniot Elastic Limit (HEL) of the material [23]. In case of Aluminum 2024, it was observed by [66] that σ_{HEL} was linearly related to the yield strength of the material.

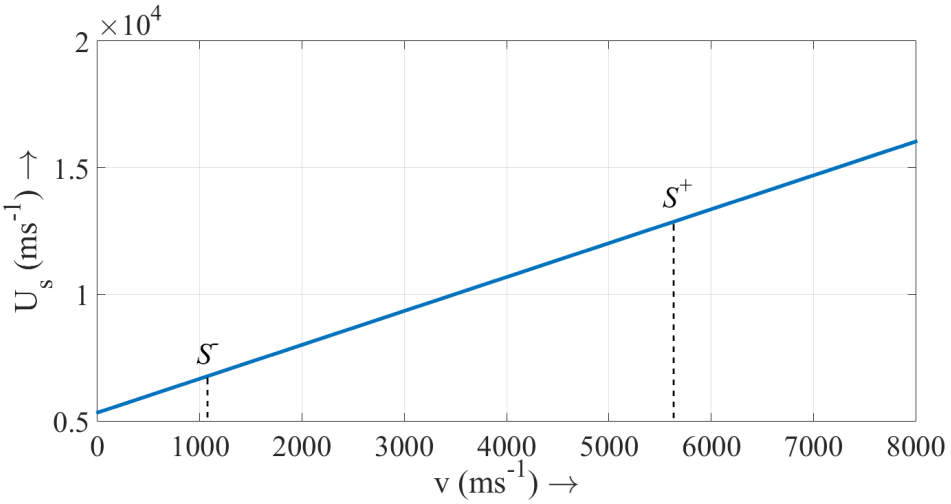

Figure 2.5: $U_s - v$ Hugoniot for Aluminum 2024 alloy.

The processes behind the formation of a structured shock wave has been a matter of extensive research. This is because shock attenuation can not only be achieved by lowering the stress σ^+, but also by increasing the rise time of the pulse. The formation of a structured shock wave has traditionally been attributed to inelastic processes, such as viscoelasticity [11], viscoplasticity ([9], [41], [75]) and twinning. Swegle and Grady [75] conducted shock impact studies on eight different materials, six metals and two insulating solids. They observed a power law scaling between the peak strain rate in the shock and change in stresses across the shock front, $\dot{\epsilon} = \beta(\Delta\sigma)^{h_{SG}}$, where $h_{SG} = 2/m$ with strain rate sensitivity $m = 0.5$. Further, they proposed a viscoplastic material model consistent with these observations. This was later analyzed in detail by Molinari and Ravichandran [58] using the model proposed by Clifton [19].

The analysis and the models developed in [58] and [75] work very well under the assumption of homogeneous materials. However, in a heterogeneous material, the propagating waves will undergo scattering due to internal reflections, which leads to energy dissipation. Grady [35] studied the fundamental questions of entropy production and basis of stress differences between the Hugoniot and the Rayleigh line in a structured wave. The phenomenon of scattering in heterogeneous materials was offered as an alternate explanation to the formation of structured waves. The acoustic scattering of a finite amplitude shock wave was studied by arguing that the energy was a combination of lattice strain energy and a vibrational energy. The vibrational energy was used to answer posed questions about entropy production and excess

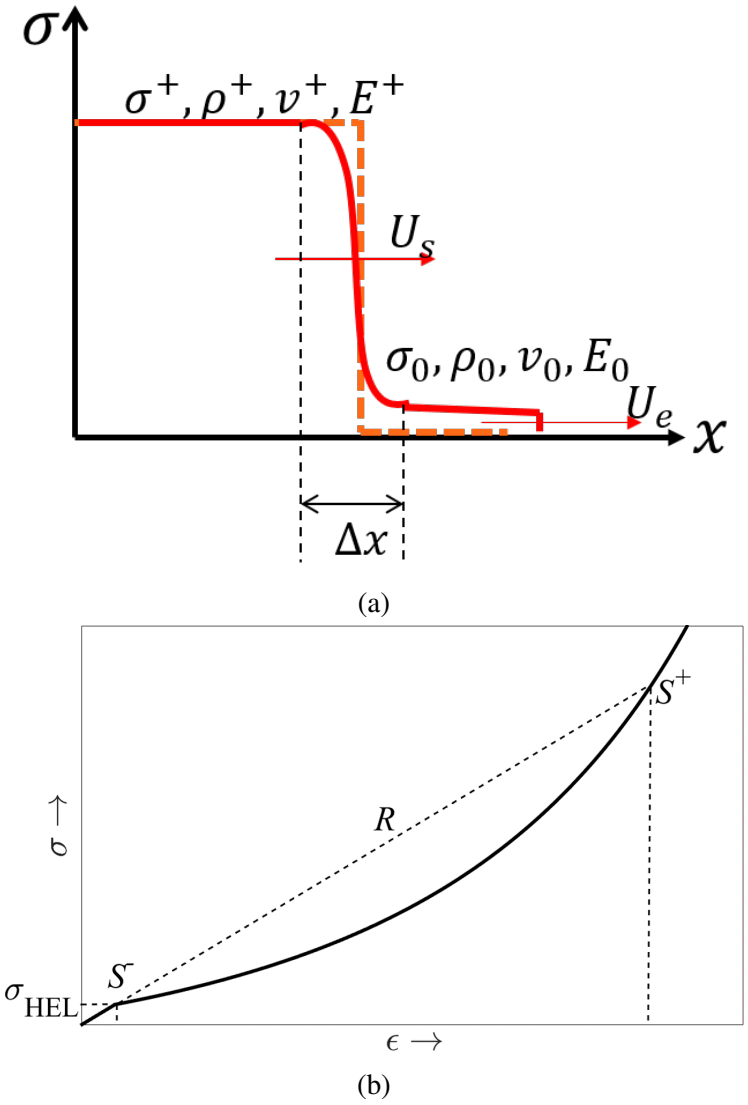

Figure 2.6: (a) Shock waves are idealized as moving discontinuity. However, a smooth, structured profile is observed (depicted in bold red) in experiments. The shock is preceded by an elastic precursor traveling at speed U_e. (b) Modified $\sigma - \epsilon$ Hugoniot curve to depict the Hugoniot Elastic Limit (HEL). The response is linear till σ_{HEL} is achieved.

stress. Using a phonon relaxation model inspired by statistical thermodynamics, anelastic equations were formulated that were consistent with phenomenological equations for structured waves developed in earlier studies [12]. While the model readily described the single-shock data for metals, it did not work very well for two-step shocks.

In order to study strongly heterogeneous materials, plate impact experiments were

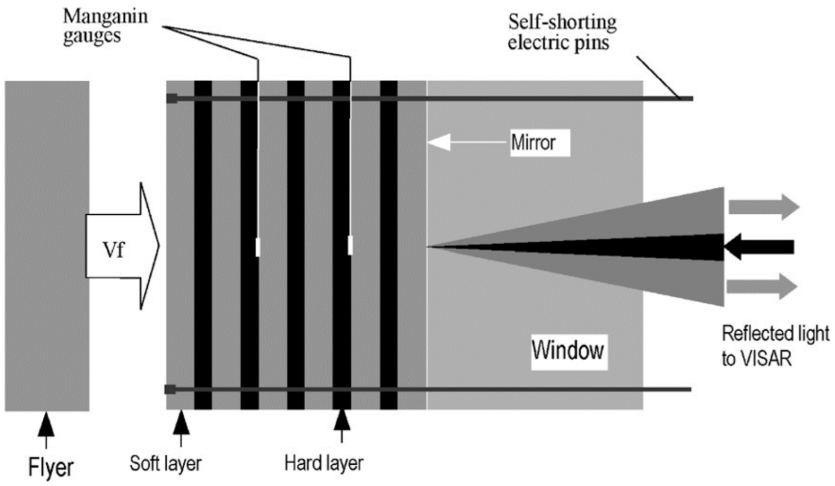

Figure 2.7: Schematic of the experimental setup used by Zhuang [89]. Particle velocity profiles were captured for different combination of impact speeds, layer thickness, material, layer arrangement and number of layers.

conducted on periodically layered composites by Zhuang [89]. Figure 2.7 shows the schematic of the experimental setup. The target composite was made of alternate layers of hard and soft materials. Particle velocity profiles were captured using a VISAR setup. It was observed that the shock structure is significantly influenced by the material heterogeneity. Factors like loading amplitude, impedance mismatch, number of layers, propagation distance and pulse duration were explored. It was observed that the shock front steepens with increase in loading amplitude. Figure 2.8a shows the difference in particle velocity profiles upon change of impedance mismatch between the composite layers. The shock steepens upon decrease in impedance mismatch indicating better wave transmission. Figure 2.8b shows the dependence of particle velocity profile on number of interfaces, keeping the total target thickness constant. The steepening of the shock front with the increase in number of interfaces was attributed to the increasing nonlinearity of the system.

A scaling law $\dot{\epsilon} = \beta(\Delta\sigma)^n$ was also calculated and it was observed that $n \approx 1.8-2.4$ instead of 4, as observed by Swegle and Grady [75]. This was purely the effect of heterogeneity, as the individual component materials had $n \approx 4$. Physically it means that the shock viscosity increases due to the wave scattering in the presence of heterogeneities. The fourth power law was further investigated by Grady [36]. It was shown that invariance of the energy-time product is a more fundamental notion from which the fourth power law can be recovered in the case of steady shock waves. A few studies on composites and porous solids were also reported where the fourth power law does not hold. The underlying mechanism behind the fourth power law

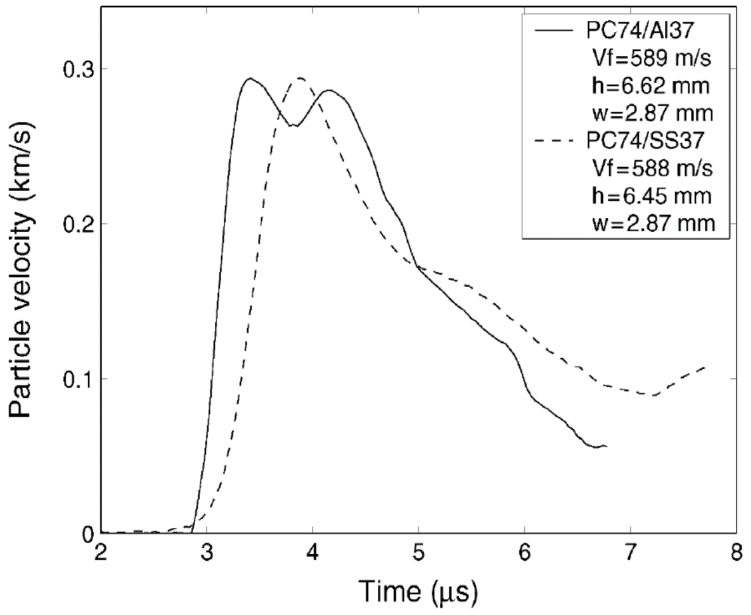

(a)

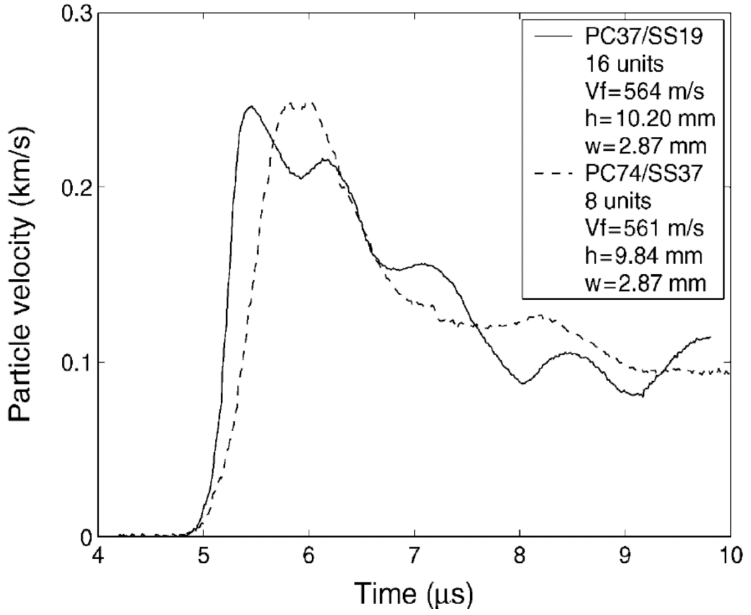

(b)

Figure 2.8: (a) Variation of particle velocity profiles with impedance mismatch in the periodic laminate. The impedance mismatch in PC74/Al37 is lesser than PC74/SS37, which means that shock is transmitted better in PC74/Al37. As such the profile is steeper in this case. (b) Variation of particle velocity profiles with number of interfaces in the laminate. The profile with more interfaces has more ripples corresponding to more scattering in the system. The profile steepens due to inherent nonlinearity in the system [89].

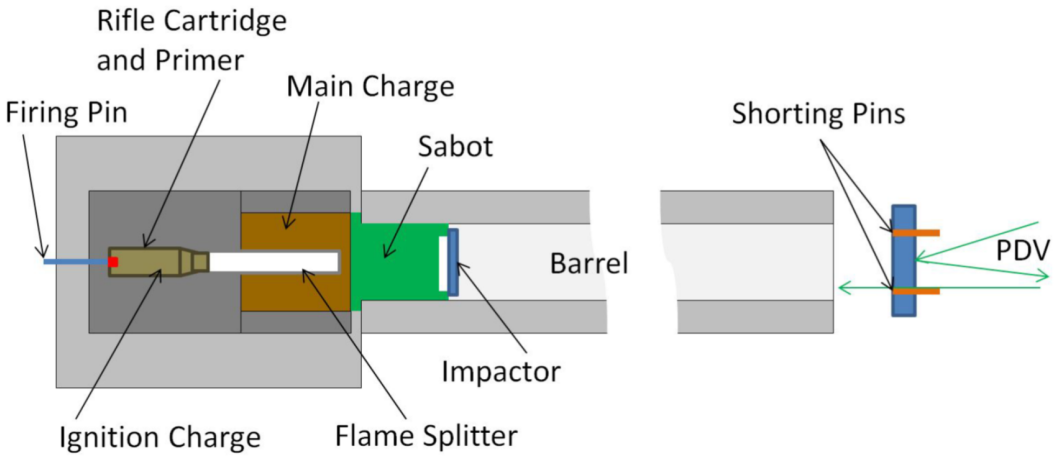

Figure 2.9: Schematic of the experimental setup used by Rauls [65]. A powder gun accelerates an Aluminum impact to impact a two phase composite specimen. Measurements were done using PDV at the right end of the target.

and the associated shock viscosity was not addressed, and it still remains an open problem.

Vogler [79] conducted numerical simulations to study the scaling laws in heterogeneous materials for three types of materials - layered composites, particulate composites and granular materials. In case of layered materials, the simulations agreed with experimental observations of Zhuang [89] and a second power law scaling was recovered. In case of particulate composites, a scaling power of $2 - 3$ was recovered. It was pointed out that scattering associated with the particulate nature of the composite played a significant role in the reduction of scaling power. In the case of granular materials, a linear scaling law was observed. A separate model, taking into account the pore collapse, was proposed to explain the linear scaling.

Recently, plate impact experiments were conducted by Rauls [65] on two phase composites. Figure 2.9 shows the schematic of the experimental setup. The target used was a two phase composite made of PMMA matrix with glass beads as inclusions. Figure 2.10 shows the cross section of the composite sample. The horizontal markings on the cross section came from polishing the sample for imaging. Particle velocity profiles were measured using Photon Doppler Velocimetry (PDV) at three points on the target surface. Experiments were carried out for different sizes (100 μm, 300 μm, 500 μm, 700 μm and 1000 μm) of glass beads and different bead volume fractions (30% and 40%).

It was observed that the presence of heterogeneity significantly influences the shock

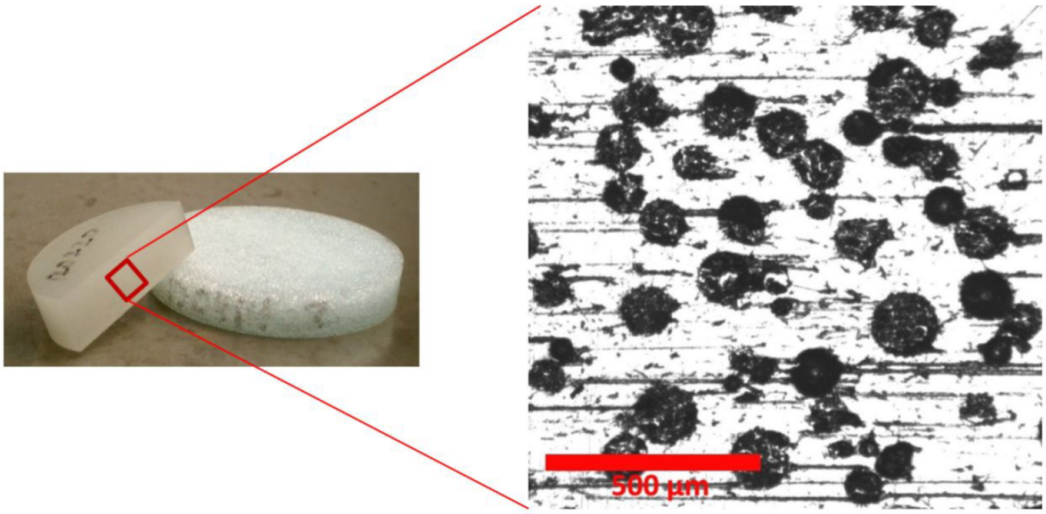

Figure 2.10: A cross section of the two phase composite sample used in [65] made from PMMA matrix and glass beads as inclusions

structure. Figures 2.11a and 2.11b show particle velocity profiles for 100 μm and 100 μm. As the mean bead size increased with fixed volume fraction, the slope of the profile reduced, implying lower shock speeds. Additionally, a structure developed at the leading edge and near the point of maximum particle velocity implying larger shock width. The presence of overshoot in the profiles, which occurs due to secondary reflections, was also a consequence of heterogeneity. Since the volume fraction was kept fixed, increasing the bead size effectively reduced the number of interfaces. This information was reflected into the decrease of overshoot observed in the profiles. Shock rise times scaled linearly with bead size for a fixed volume fraction, with shock width increasing by an order of magnitude between 100 μm and 1000 μm. CTH simulations showed that for larger bead size, due to the decrease in number of beads and increase in bead spacing, the linear scaling of the shock width started to break down.

From a theoretical perspective, scattering of elastic waves in a periodic medium has been studied extensively. In a periodic medium using Bloch-floquet theory, frequency responses have been studied by Sun [74], Lee and Yang [46] and Nayfeh [61] among others. Studies have also been conducted for elastic waves in a random medium by Ryzhik [67] and have showed how scattering results in a diffusive response. However, very little is known about nonlinear wave propagation in a heterogeneous medium. Using Bloch-Floquet theory, plate impact response of periodic laminate was studied by Chen [18]. An approximate solution for the plate impact problem in the periodic domain was constructed along the lines of the elastic

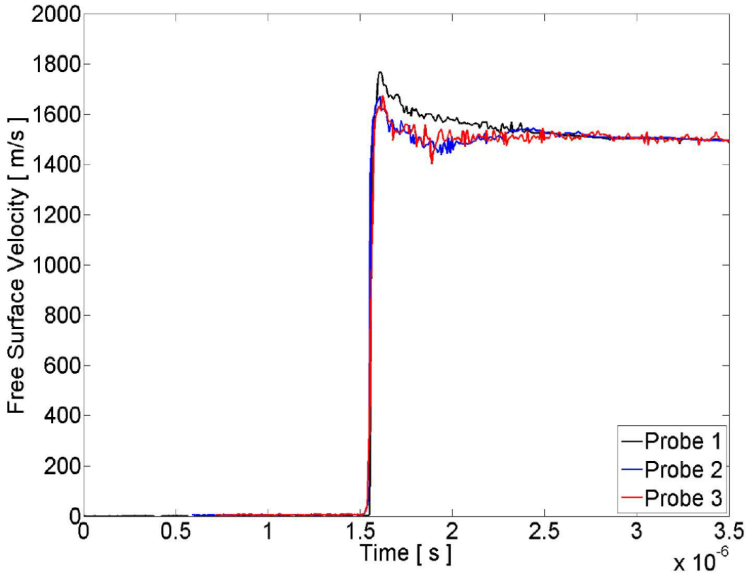

(a)

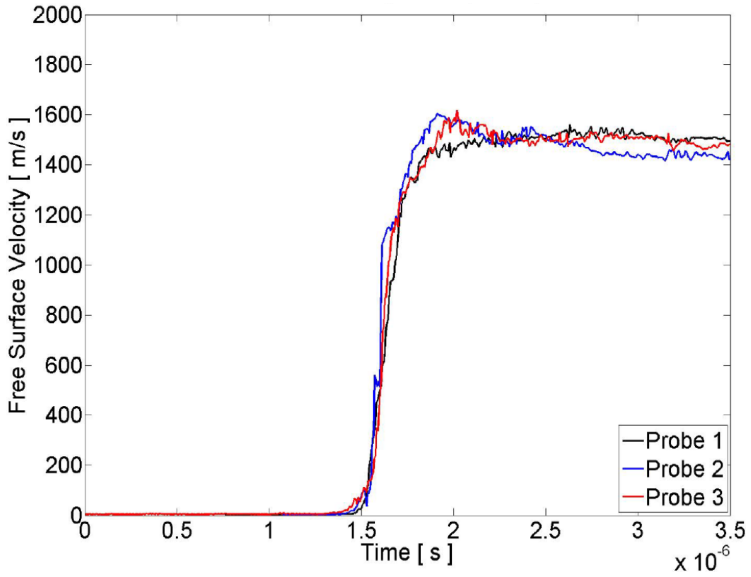

(b)

Figure 2.11: Particle velocity profiles for bead size (a) 100 μm and (b) 1000 μm for 40% volume fraction. Profiles are measured at three points of the sample to account for spatial heterogeneity. The profile for 1000 μm beads has less steep slope with rounded structures towards the leading and trailing edges of the shock. Additionally, the overshock is greater for the 100 μm bead size due to greater number of beads, hence greater number of interfaces, leading to contributions from secondary reflections.

wave solution. An expression for mean stress was derived for moderate shocks and scattering was accounted for in the form of wave trains. Each wave train had a contribution to the stress state for a specific time duration. The overall stress was

then expressed as a combination of mean stress and time dependent contribution from wave trains.

Chapter 3

SHOCK WAVE SCATTERING IN LAYERED MATERIALS

[1] Vinamra Agrawal and Kaushik Bhattacharya. "Shock wave propagation through a model one dimensional heterogeneous medium". In: *International Journal of Solids and Structures* 51.21–22 (2014), pp. 3604–3618. ISSN: 0020-7683. DOI: http://dx.doi.org/10.1016/j.ijsolstr.2014.06.021. URL: http://www.sciencedirect.com/science/article/pii/S0020768314002534.

In this chapter, the phenomenon of scattering is analyzed in a layered, not necessarily periodic, medium. Specifically, a one-dimensional system made of perfectly bonded homogeneous layers is considered. An overall picture is developed by studying individual wave interactions in the system.

3.1 Problem Description

Figure 3.1 shows the schematic of the impact problem on the layered composite. The layers are assumed homogeneous and perfectly bonded to ensure continuity of displacements across the material interfaces. As explained in Section 2.3, the material under shock loading follows a Hugoniot curve represented in Figure 2.6b. While the loading is governed by a Hugoniot curve, the unloading happens along an isentrope leading to the formation of rarefaction waves. Unlike shock waves, the states across rarefaction waves are not discontinuous. Rarefaction waves are represented as a 'wave-fan' across which states are connected continuously [23]. These waves are characteristic of the convex super-linear behavior of the Hugoniot beyond the Hugoniot elastic limit. Impact, wave-wave interactions and wave-material interactions lead to a complex system of shock waves and rarefaction waves into the material. In order to simplify the analysis in this problem, the Hugoniot is approximated by a piecewise linear stress strain curve as represented in Figure 3.1. In other words, the rarefaction waves are no longer present in the system as they can be collapsed onto a single 'elastic' wave.

As explained in Section 2.3, shock problems are typically augmented with a linear $U_s - v$ Hugoniot. In this problem, following Knowles [44], the piecewise affine stress-strain relationship is augmented with a kinetic relation that relates shock speed with the rate of dissipation at the shock front. The framework was originally

introduced by Abeyaratne and Knowles [1], [4] to study phase transitions. However, it has been useful to study shock wave propagation ([44], [62]). Further, the structure of the shock is neglected in this analysis. This means that the shock is assumed to be a moving discontinuity. This is because the kinetic relation can be chosen in such a way that dissipation at the discontinuity and the dissipation due to the structured shock is equal [4]. Additionally, in a more recent study by Tan [76], it was shown that sharp front assumption is valid if the length scale of the heterogeneity is much larger than the inherent shock width.

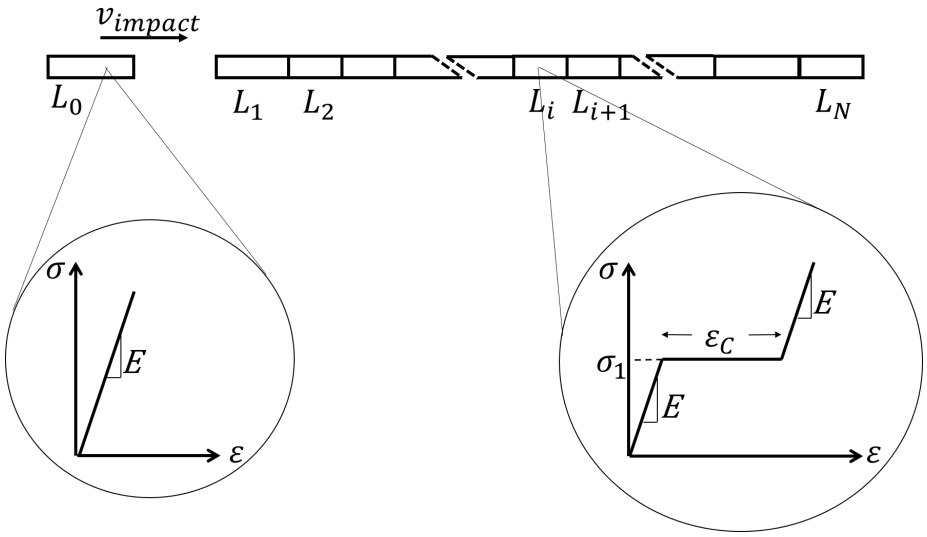

Figure 3.1: Schematic representation of plate impact

The problem setup (Figure 3.1) shows a layered composite consisting of N layers, ρ_i and L_i being the density and thickness of the i^{th} layer, being impacted upon by a linear elastic flyer traveling at speed v_{impact}. The left edge of the flyer and the right edge of the layered composite has a traction free boundary condition. For now, the piecewise affine stress-strain curve is parameterized by three quantities - yield stress σ_1, the modulus E, and the compliant strain ε_C. Additionally, every layer is assumed to have the same ρ, σ_1 and E. The case with relaxed assumption will be addressed later. This assumption simplifies the analysis by reducing the heterogeneity to shock waves and making the composite homogeneous to elastic waves. This will be addressed in detail in Section 3.2. Finally, the system is assumed isothermal.

3.2 Governing equations

The problem is formulated in Lagrangian setting with $X = 0$ being on the left edge of the flyer. The moment of impact is marked as $t = 0$. The stress, strain

and particle velocity at any point X at time t is denoted by $\sigma(X,t)$, $\varepsilon(X,t)$ and $v(X,t)$, respectively. The compressive stresses and strain are taken to be positive as notation. The system is governed by the set of compatibility and conservation laws as presented in Section 2.1. Additionally, due to the isothermal assumption, conservation of energy is not required as it is automatically taken care of by the kinetic relation and the dissipation inequality. The piecewise affine stress-strain curve allows the system of equations to reduce to following jump equations:

$$[\![\sigma]\!] + \rho\dot{s}[\![v]\!] = 0, \tag{3.1}$$

$$[\![v]\!] + \dot{s}[\![\varepsilon]\!] = 0, \tag{3.2}$$

where $\dot{s}$ is the speed of the propagating discontinuity.

An *elastic* wave is described as a moving discontinuity across which the states lie in the same branch of the stress-strain curve. Further, a *shock* wave is characterized by the moving discontinuity across which the states lie on different branches of the stress-strain curve. This is represented in Figure 3.2a, where states 1-2 and Q-3 are connected through an elastic wave and states 2-3 are connected by a shock wave. For an elastic wave, it can be shown that the equations (3.1) and (3.2) hold if and only if,

$$\dot{s} = \pm c = \pm\sqrt{\frac{E}{\rho}}. \tag{3.3}$$

The assumption of uniform ρ, E and σ_1 allows the same elastic wave speed c for all layers, thereby making the system homogeneous to elastic waves. The heterogeneity is only limited to shock waves. The dissipation across the shock front can be represented as the signed area between the line $2-3$ and the stress strain curve between the points 2 and 3. This means that across the shock front, the dissipation is given by the difference in area $P3Q$ and $P21$.

For this analysis, a *maximally dissipative* kinetic relation [83] is used as the additional empirical law to complete the set of equations to obtain a unique solution. Physically, it means that the shock tries to maximize the dissipation [62]. Maximal dissipation kinetics is thermodynamical equivalent of the Lax entropy criteria [47] widely used in shock physics. Thus, for a compression shock taking the material from the low-strain branch to the high-strain branch, the low strain state has to coincide with point 1 for maximal dissipation kinetics to be satisfied. Along the same lines, the tensile shock from high-strain branch to low-strain branch can satisfy the maximal dissipation law only when the high-strain state coincides with point Q in Figure

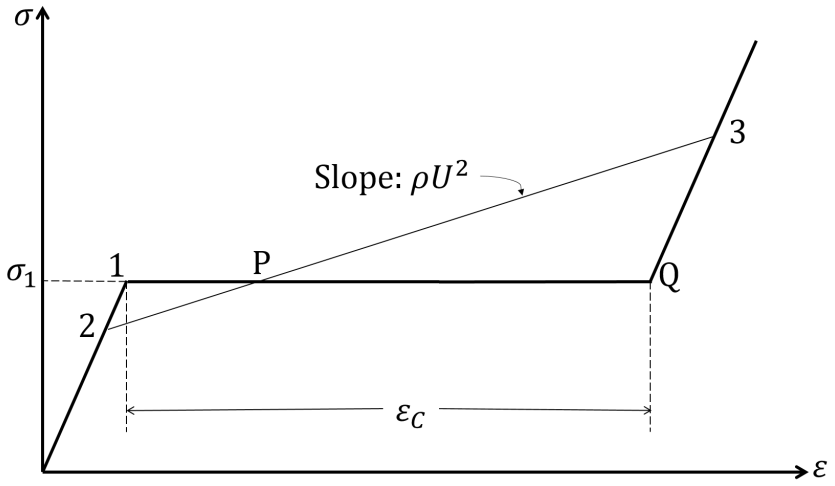

(a)

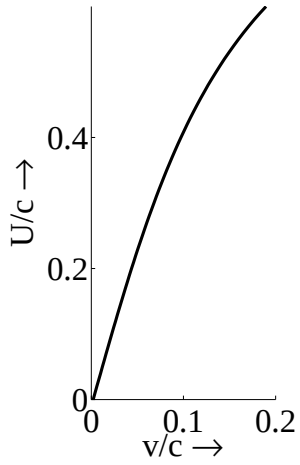

(b)

Figure 3.2: (a) Illustration of elastic and shock waves in the stress-strain curve. The difference between the areas P3Q and P21 denotes the dissipation across the shock front.

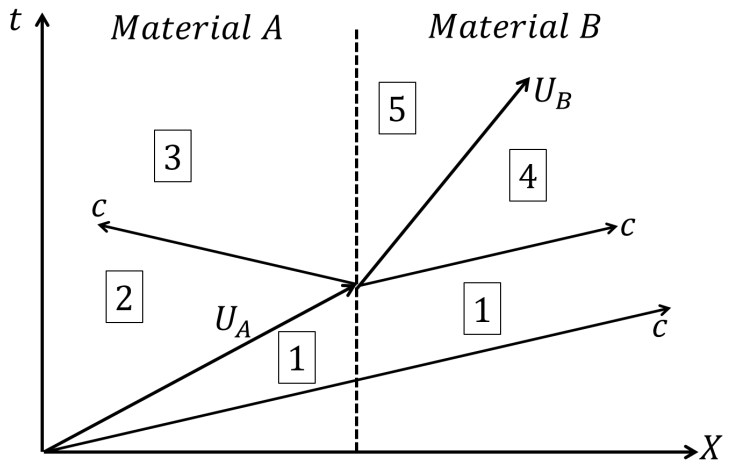

(a)

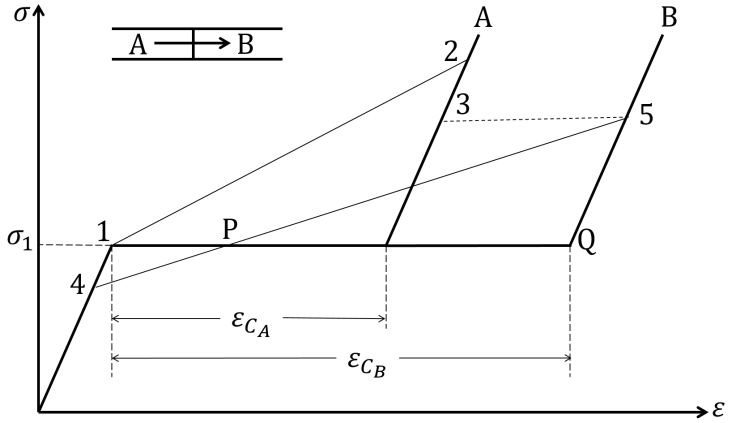

(b)

Figure 3.3: (a) $X - t$ diagram for the shock interaction problem at the A-B material interface. The impinging shock U_A interacts with the material interface to produce the elastic waves and a shock U_B.

3.2a. A formal expression of the kinetic relation can also be derived using the jump equations (3.1) and (3.2) as follows:

$$-[\![v]\!] = \frac{Uc^2\varepsilon_c}{c^2 - U^2}. \tag{3.4}$$

The expression (3.4) for the kinetic relation is represented in Figure 3.2b. Although this is not a linear expression, a linear approximation can be made for a large range of under-driven shocks.

3.3 Shock wave interaction at a material interface

In this section, the fundamental problem of the interaction of a shock wave at a material interface is considered. Two layers A and B, perfectly bonded at the

interface, are considered with initial stress-free configuration. A sudden loading $\sigma_0 > \sigma_1$ is applied to the left end and the resulting wave problem is studied. Figures 3.3a and 3.3b show the $X-t$ diagram of the problem and the equivalent representation in the stress-strain space, respectively. The loading produces a combination of an elastic wave and a shock wave into the material A. Since the system is homogeneous to elastic waves, the elastic wave propagates unimpeded into the material B. In order to satisfy the maximal dissipation kinetics, the elastic wave needs to take the material from unstressed configuration to point 1 in the stress strain curve shown in Figure 3.3b. The shock U_A takes the state of the material A from point 1 to 2, with $\sigma_2 = \sigma_0$ as shown in Figure 3.3b. The jump equations across the elastic and shock waves are given by

$$\sigma_1 - 0 + \rho c(v_1 - 0) = 0, \tag{3.5}$$

$$\sigma_2 - \sigma_1 + \rho U_A(v_2 - v_1) = 0, \tag{3.6}$$

$$v_2 - v_1 + U_A(\varepsilon_2 - \varepsilon_1) = 0. \tag{3.7}$$

Since the states σ_1, σ_2, ε_1 and ε_2 are known, the above equations can be solved for v_1, v_2 and U_A to give

$$v_1 = -\frac{\sigma_1}{\rho c}, \tag{3.8}$$

$$U_A = \sqrt{\frac{\sigma_2 - \sigma_1}{\rho(\varepsilon_2 - \varepsilon_1)}}, \tag{3.9}$$

$$v_2 = v_1 - \sqrt{\rho(\sigma_2 - \sigma_1)(\varepsilon_2 - \varepsilon_1)}. \tag{3.10}$$

Upon interaction of the shock wave at the A-B material interface, following waves can potentially form as shown in Figure 3.3a:

1. An elastic wave originating from the point of interaction propagating back into A taking the state of A from point 2 to 3.

2. An elastic wave propagating into B taking the state of B from point 1 to 4.

3. A shock wave propagating into B taking the state of B from 4 to 5.

From the previous discussion, the maximal dissipation kinetics enforces state 4 to coincide with 1. More precisely, $\sigma_4 = \sigma_1$, giving $v_4 = v_1$. Physically this means that the forward propagating elastic wave B will not exist in the system. Additionally, the layers are perfectly bonded which means that $\sigma_3 = \sigma_5$ and $v_3 = v_5$. As such,

only state 3 needs to be determined. Writing jump equations across the elastic wave in A and across the shock wave in B,

$$\sigma_3 - \sigma_2 - \rho c(v_3 - v_2) = 0, \tag{3.11}$$

$$\sigma_2 - \sigma_1 + \rho U_B(v_2 - v_1 = 0, \tag{3.12}$$

$$v_3 - v_1 + U_B(\varepsilon_3 - \varepsilon_1) = 0. \tag{3.13}$$

Solving these equations give,

$$\sigma_3 = \frac{E\varepsilon_c^B\sigma_1 - \sigma_1^2 + (\sigma_2 + \rho c(v_1 - v_2))^2}{2(\sigma_2 - \sigma_1) + \rho c(\varepsilon_c^B c + 2v_1 - 2v_2)}, \tag{3.14}$$

$$v_3 = \frac{(E\varepsilon_c^B(\sigma_1 - \sigma_2 + \rho c v_2)) - (\sigma_1 - \sigma_2 + \rho c(-v_1 + v_2))(\sigma_1 - \sigma_2 + \rho c(v_1 + v_2))}{\rho c(-2\sigma_1 + 2\sigma_2 + \rho c(\varepsilon_c^B c + 2v_1 - 2v_2))}, \tag{3.15}$$

$$U_B = \frac{\sigma_2 - \sigma_1 + \rho c(v_1 - v_2)}{\sigma_2 - \sigma_1 + \rho c(\varepsilon_c^B c + v_1 - v_2)}. \tag{3.16}$$

Simplification of above expressions results in

$$U_B = \frac{rU_A c}{c + (r-1)U_A}, \tag{3.17}$$

where $r = \varepsilon_c^A/\varepsilon_c^B$ is the compliance ratio between the two materials. It can be seen from (3.17) that if $r < 1$, which means that the shock passes from a less compliant to a more compliant medium, the shock speed decreases. Similarly, if $r > 1$, the shock speed increases. A similar expression for σ_3, purely in terms of r, cannot be derived because σ_3 can not be eliminated. Second, the forward moving elastic wave in B is not present in this system, which is a consequence of the kinetic law. Finally, the receding elastic wave in B eventually brings the entire laminate to the same stress state σ_3.

In the analysis involving a Hugoniot, instead of a piecewise affine relation, the shock interaction at the material interface depends upon the impedance ration $Z = \rho_A C_A/\rho_B C_B$, where C is the characteristic speed introduced in (2.18). The case of $Z > 1$ results in the formation of two shock waves, one receding in A and one propagating in B. This case is equivalent to $r < 1$ presented in this analysis. For $Z < 1$, the interaction leads to the formation of a shock wave in B and a rarefaction wave fan in A. This case is equivalent to $r > 1$ where a shock wave forms in B and an unloading elastic wave forms in A.

3.4 Semi-infinite medium

In order to get one step closer to the problem in Figure 3.1, a laminate with N segments is chosen. The impactor and the last layer of the laminate are assumed to be semi-infinite. This assumption removes any possible wave reflections from the ends of the target or the impactor. Additionally, as pointed out in the earlier section, the laminate is homogeneous to elastic waves and the interaction of a shock at material interface does not produce any forward propagating elastic waves. This implies that the shock never interacts with an elastic wave and the only interaction is that with a material interface. As such, the problem can be described exactly as in the previous section. The shock speed in the N^{th} layer can be expressed as

$$U_N = \frac{r_N U_1 c}{c + (r_N - 1)U_1}, \tag{3.18}$$

where $r_N = \varepsilon_c^1/\varepsilon_c^N$ is the ratio of compliant strain of the first and the last layer.

The expression (3.18) implies that the speed of the shock in the semi-infinite medium depends only on the properties of the first and the last layer. The properties and the arrangement of intermediate layers in this model do not play a role in determining the final state. Again, the receding elastic waves will eventually bring the entire system to the common stress state σ_N.

3.5 Finite heterogeneous medium: Method

In this section, the semi-infinite assumption is removed from the previous section. This adds a lot more complexity in the system due to the elastic waves reflecting off the free surface and interacting with the shock. It is important to note that the solution (v, σ) is piecewise constant due to the nature of the stress-stress curve. This means that following the waves is enough to generate the solution. The numerical scheme presented in the next section follows every elastic wave and shock wave as it nucleates and propagates into the system. As a first step, all possible interactions between waves and interfaces are cataloged. These interactions are posed locally as Riemann problems with piecewise constant initial data.

Individual interactions

An advantage of having a piecewise linear stress-strain curve is that the all possible interactions can be classified into the following classes of Riemann problems.

1. Reflection of an elastic wave from a free edge
2. Interaction of one elastic wave with another

a) Interaction within a linear elastic material

b) Interaction within a piecewise affine material

   i. Interaction resulting in the formation of two elastic waves

   ii. Interaction of waves in low-strain branch forming a pair of compression shocks

   iii. Interaction of waves in high-strain branch forming a pair of tensile shocks

c) Interaction at the interface of linear and piecewise affine material

   i. Interaction resulting in the formation of two elastic waves

   ii. Interaction resulting in the formation of a compression shock in piecewise affine material

   iii. Interaction resulting in the formation of a tensile shock in piecewise affine material

3. Elastic wave in piecewise affine material crossing material boundary to enter another layer

4. Elastic wave from a linear elastic material entering a piecewise affine material

   a) Interaction forming a compression shock in piecewise affine material

   b) Interaction forming a tensile shock in piecewise affine material

   c) Low amplitude wave passing through unimpeded

5. Interaction of a compression shock at an interface

   a) Interface connects a linear elastic and piecewise affine material

   b) Interface connects two piecewise affine materials

6. Interaction of a tensile shock at an interface

   a) Interface connects a linear elastic and piecewise affine material

   b) Interface connects two piecewise affine materials

7. Interaction of a shock wave with an elastic wave

   a) Compression shock and elastic wave traveling in the same direction

   b) Compression shock and elastic wave traveling in the opposite direction

   c) Tensile shock and elastic wave traveling in the same direction

d) Tensile shock and elastic wave traveling in the opposite direction

8. Interaction of two shock waves traveling in opposite direction

   a) Compression shocks

   b) Tensile shocks

Solutions to Riemann problems

Following the procedure listed in Section 3.3, explicit solutions to a few Riemann problems mentioned above are derived in this section.

Interface interactions

a. Elastic wave from a purely elastic medium entering a piecewise affine medium: Figures 3.4a and 3.4b show the schematic of such an interaction. As shown in Figure 3.4b, material A is purely elastic while material B is piecewise linear. Depending upon the states a and b in Figure 3.4a, there are three possible cases.

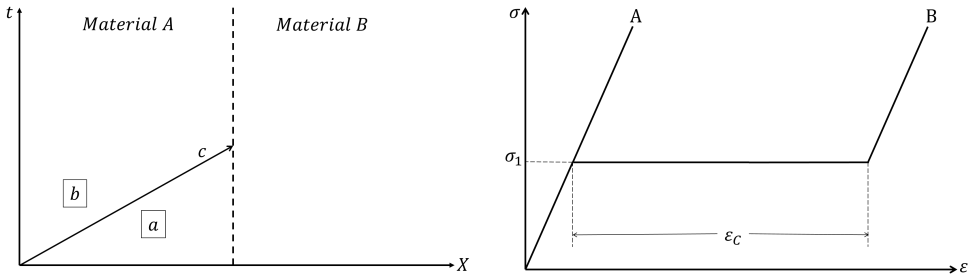

(a) (b)

Figure 3.4: Schematic diagram of the elastic wave interaction at A-B interface

Case 1: No shock formation: This happens when either $\sigma_a < \sigma_1$, $\sigma_b \leq \sigma_1$ or $\sigma_a > \sigma_1$, $\sigma_b \geq \sigma_1$. Since the layers are elastically homogeneous, in this case the elastic wave passes through the interface without any interruption.

Case 2: Formation of compression shock: Figure 3.5a shows the case when the interaction leads to the formation of compression shock. This happens when $\sigma_a \leq \sigma_1$ and $\sigma_b > \sigma_1$. In case $\sigma_a = \sigma_1$, the state just ahead of the point of interaction needs to be considered to decide if case 1 is applicable or case 2. The process in stress-strain space is represented in Figure 3.5b. The maximal dissipation criteria requires state e in Figure 3.5a to coincide with σ_1. Finally, the shock speed U is

given by

$$U = \frac{c(-2\sigma_1 + \sigma_a + \sigma_b + c\rho(v_a - v_b))}{-2\sigma_1 + \sigma_a + \sigma_b + c\rho(\varepsilon_c c + v_a - v_b)}.$$

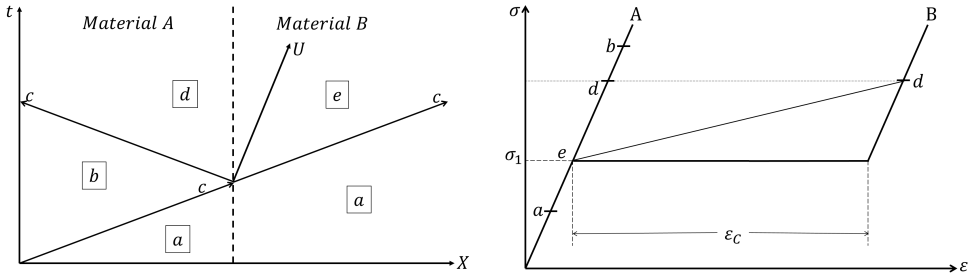

(a) (b)

Figure 3.5: Elastic wave interaction leading to a compression shock

Case 3: Formation of unloading shock: Figure 3.6a shows the formation of an unloading shock during this interaction. This happens when $\sigma_a \geq \sigma_1$ and $\sigma_b < \sigma_1$. Just as in case 2, if $\sigma_a = \sigma_1$, the state ahead of the point of interaction needs to be considered to decide if case 1 is applicable or case 3. The Riemann problem in stress-strain space is presented in Figure 3.6b. Finally, the shock speed is given by

$$U = c - \frac{E\varepsilon_c c}{2\sigma_1 - \sigma_a - \sigma_b + \rho c(\varepsilon_c c - v_a + v_b)}.$$

It should be noted that state d in Figure 3.6a can be of unloading nature which can lead to the separation of A-B interface. This enables the study of spallation and re-compression shocks.

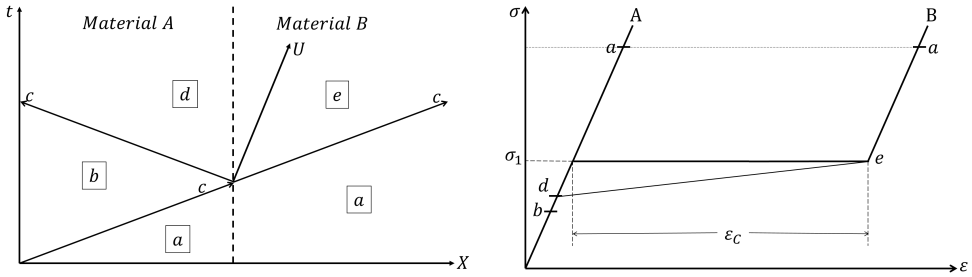

(a) (b)

Figure 3.6: Elastic wave interaction leading to an unloading shock

b. Compression/Unloading shock entering a purely elastic medium: The interaction of a shock wave at an interface of two nonlinear materials was studied in

Section 3.3. The case of a shock wave interacting with the interface of a nonlinear and linear material is considered here. Figures 3.7a and 3.7b show the Riemann problem of a compression shock interacting with the interface of nonlinear and linear material in $X - t$ and stress-strain space, respectively. The interaction leads to the formation of two elastic waves. The state d in Figure 3.7a and 3.7b is given by

$$\sigma_d = \frac{1}{2}\left(\sigma_1 + \sigma_b + \rho c(v_a - v_b)\right),$$
$$v_d = \frac{1}{2\rho c}\left(\sigma_1 - \sigma_b + \rho c(v_a + v_b)\right).$$

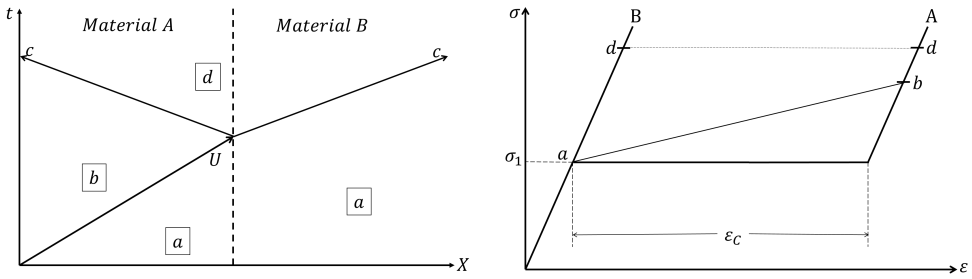

(a) (b)

Figure 3.7: Compression shock wave entering a purely elastic material

The case of unloading shock is represented in Figures 3.8a and 3.8b. The state d in Figures 3.8a and 3.8b can be calculated from the same expressions above.

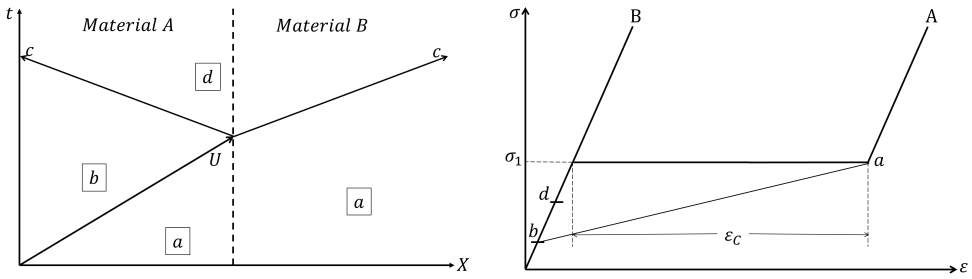

(a) (b)

Figure 3.8: Compression shock wave entering a purely elastic material

c. Unloading shock entering another nonlinear material The interaction of an unloading shock at the interface of two nonlinear layers leads to the formation of another unloading shock. The interaction is presented in Figure 3.9a in $X - t$ space

and in Figure 3.9b in the stress-strain space. The interaction leads to the formation of two elastic waves and an unloading shock. The process is exactly the same as in Section 3.3. The maximal dissipation kinetics ensure that the forward moving elastic wave does not exist. Finally,

$$U_B = c\left(\frac{\sigma_1 - \sigma_b + \rho c(-v_a + v_b)}{\sigma_1 - \sigma_b + \rho c(\varepsilon_c^B c - v_a + v_b)}\right).$$

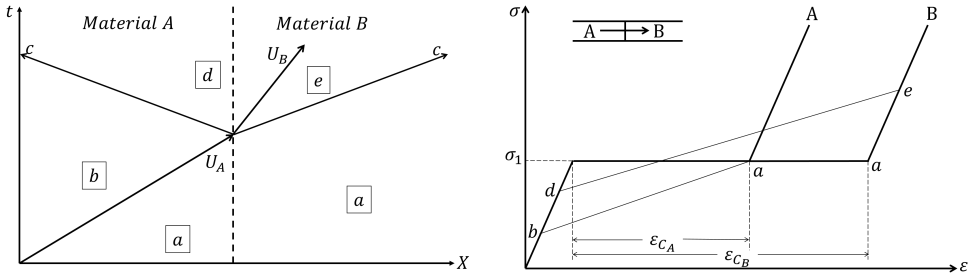

(a) (b)

Figure 3.9: Unloading shock wave entering another piecewise affine material

Wave - wave interaction

a. Interaction of elastic wave and shock wave traveling in the same direction: Next, the interaction of an elastic and a shock wave traveling in same direction is studied. The interaction is represented by Figure 3.10a in $X - t$ space and by Figure 3.10b in stress-strain space. The speed of the resulting shock is given by,

$$U_2 = c\left(\frac{-\sigma_1 + \sigma_3 + \rho c(v_1 - v_3)}{-\sigma_1 + \sigma_3 + \rho c(\varepsilon_c c + v_1 - v_3)}\right).$$

b. Interaction of elastic wave and shock wave traveling in opposite directions: Next, the interaction is considered for the case when the elastic wave and the shock wave are traveling in opposite directions. Figure 3.11 shows the interaction between an elastic wave and a shock wave (compression shock in this case) leading to two possible solutions - unloading shock and compression shock. Admissibility criteria for the solution are governed by the fact that the speed of the shock should be less than the elastic wave speed. In the case that both solutions are admissible, the dominating solution is determined by maximal dissipation criteria. The solution to the Riemann problem involves connecting states 2 and 4 in the stress-strain space. The solution

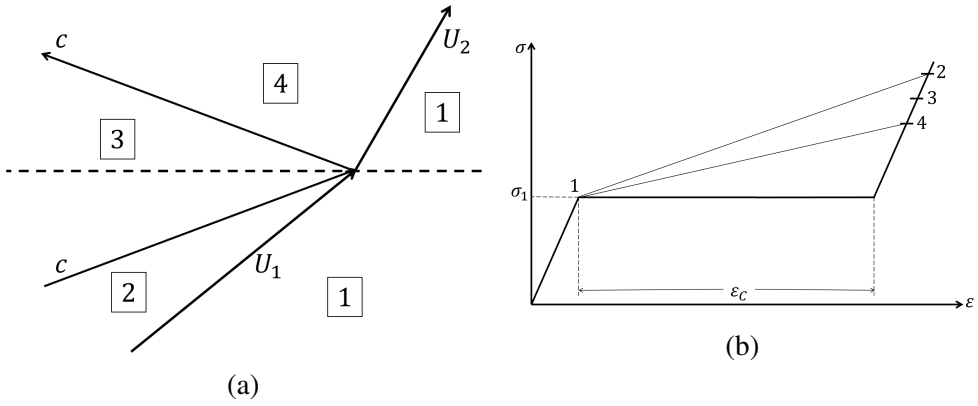

Figure 3.10: Interaction of elastic wave with compression shock

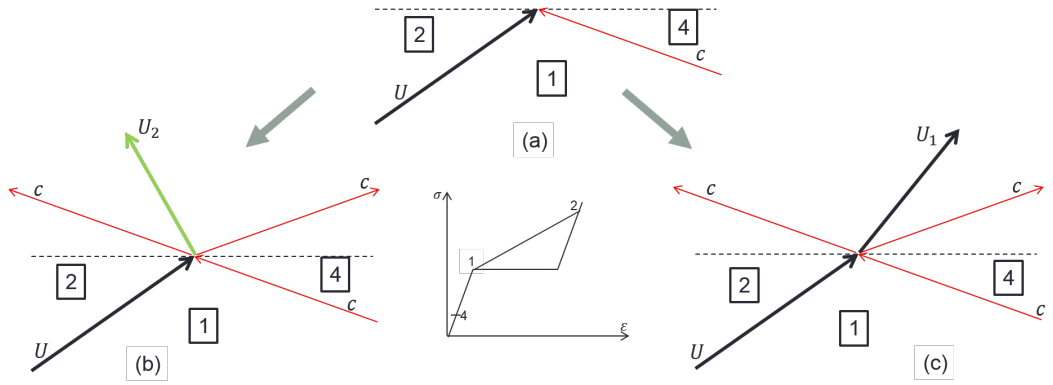

Figure 3.11: Interaction of elastic wave and compression shock traveling in opposite directions resulting in two possible solutions - (b) unloading shock wave and (c) compression shock wave.

involving unloading shock involves reversal of the shock direction. The speeds U_1 and U_2 are given by

$$U_1 = c - \frac{Ec\varepsilon_c}{\sigma_2 + \sigma_4 - 2\sigma_1 + \rho c(\varepsilon_c c - v_2 + v_4)},$$
$$U_2 = c - \frac{Ec\varepsilon_c}{2\sigma_1 - \sigma_2 - \sigma_4 + \rho c(\varepsilon_c c + v_2 - v_4)}.$$

Interactions of this kind play an important role in the analysis ahead. The reversal of the shock direction and change of the nature of the shock marks the 'reflection' of the shock wave.

c. Interaction of two elastic waves in a nonlinear layer: Next, the interaction between two elastic waves in studied is a nonlinear layer. The importance of this interaction will be seen later on in Section 3.6 when the possibility of spallation will be discussed. Two elastic waves of unloading nature in the high strain branch of the

stress strain curve can lead to the formation of a pair of unloading shocks as shown in Figure 3.12a and 3.12b. The shock speeds U_1 and U_2 are given by,

$$U_1 = U_2 = c\,\frac{E\varepsilon_c - [E^2\varepsilon_c^2 + (\sigma_3 + \sigma_2 - 2\sigma_1 + \rho c(v_3 - v_2))^2]^{1/2}}{\sigma_3 + \sigma_2 - 2\sigma_1 + \rho c(v_3 - v_2)}.$$

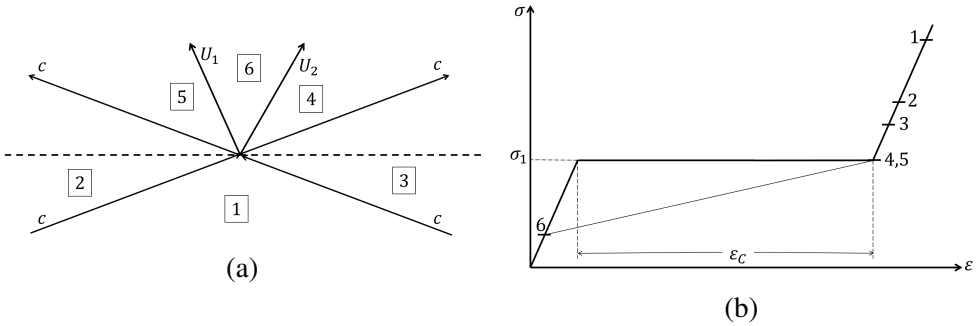

Figure 3.12: Interaction of two elastic waves forming a pair of unloading shocks

Similarly the interaction of two elastic waves of loading nature can lead to the formation of a pair of compression shocks. This Riemann problem is represented in Figure 3.13a in the $X - t$ plane and in Figure 3.13b in the stress-strain space. The speed of the compression shocks in this case is given by

$$U_1 = U_2 = c\,\frac{-E\varepsilon_c + [E^2\varepsilon_c^2 + (\sigma_3 + \sigma_2 - 2\sigma_1 + \rho c(v_3 - v_2))^2]^{1/2}}{\sigma_3 + \sigma_2 - 2\sigma_1 + \rho c(v_3 - v_2)}.$$

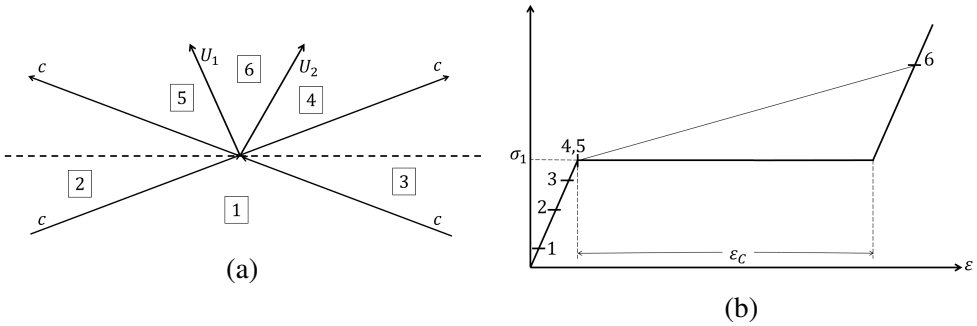

Figure 3.13: Interaction of two elastic waves forming a pair of compression shocks

d. Interaction of two shock waves traveling in opposite directions: Another possible interaction is the interaction of two shock waves in a nonlinear material. While this is a relatively unlikely interaction, it is still important because it causes the shock

waves to disappear. State 4 in Figures 3.14a and 3.14b can be determined via jump conditions. Similarly, the interaction between two unloading shock waves leads to formation of two elastic waves.

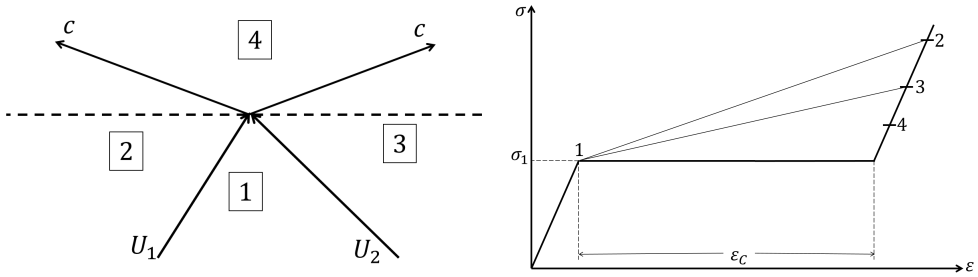

Figure 3.14: Interaction of two compression shock waves forming a pair of elastic waves

e. Interaction of two elastic waves at the interface of linear and piecewise affine layer: Although this interaction is very rare, it becomes important when a periodically layered linear-nonlinear medium is considered. Under certain kinds of conditions, the interaction can lead to formation of shocks in the nonlinear layer. Figure 3.15a shows the Riemann problem where the interaction leads to the formation of compression shock in the nonlinear layer. An equivalent representation in the stress-strain space is shown in Figure 3.15b. The speed of the compression shock can be expressed as,

$$U_1 = c - \frac{Ec\varepsilon_c}{\sigma_2 + \sigma_3 - 2\sigma_1 + \rho c(E\varepsilon_c - v_2 + v_3)}.$$

Similarly, Figures 3.16a and 3.16b represent the case of tensile shock formation. An expression can be obtained for tensile shock speed as follows

$$U_1 = c + \frac{Ec\varepsilon_c}{\sigma_2 + \sigma_3 - 2\sigma_1 - \rho c(E\varepsilon_c + v_2 - v_3)}.$$

Numerical method

The numerical scheme employed follows every wave in the system. An object oriented approach is developed where each wave is treated as an *object* containing the origin and the endpoint in the $X - t$ plane, the direction, the speed, the material in which it is propagating, the *status* of the wave, and the state (σ, ε, v) before and after the wave. Each wave is assigned a status, either *active* or *passive*. An active

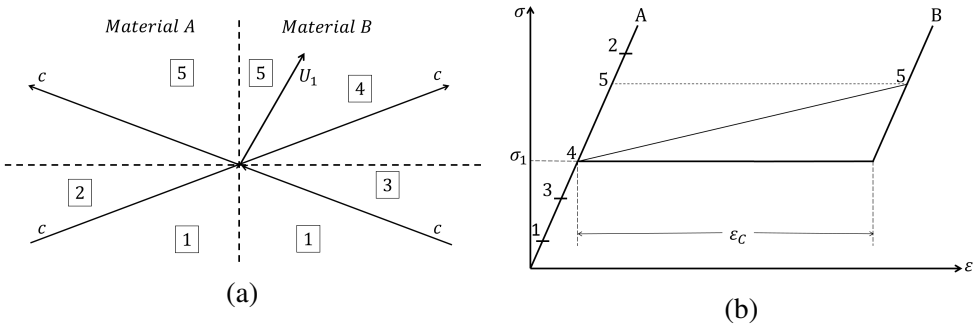

Figure 3.15: Interaction of two elastic waves forming a compression shock in the piecewise affine layer

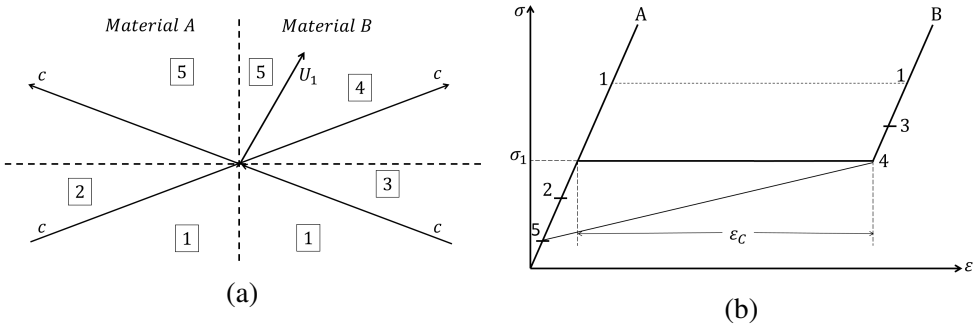

Figure 3.16: Interaction of two elastic waves forming a compression shock in the piecewise affine layer

wave can interact with other active waves and the material boundary and lead to more active waves. The solution for the corresponding Riemann problem is looked up in the list above. Upon interaction, the status of an active wave is changed to passive.

It is important to note that due to the absence of any space-time discretization, the outlined scheme produces an exact solution to the impact problem. The only errors in the system come from rounding off while calculating the next time of interaction and the solutions to the Riemann problem.

3.6 Finite heterogeneous medium: Results

Calculations are carried out for $\rho = 2700$ kg/m^3, $c = 6000$ m/s, $\sigma_1 = 200$ MPa, $E = \rho c^2$, $V_{impact} = 1000$ m/s and the total length of the target being 1m. The length of the flyer L_0, the number of layers N, and the compliant strain ε_c profiles are varied from simulation to simulation. The range of ε_c is always maintained from 0.2 to 0.6. The chosen range of ε_c is for demonstrative purposes, and to remain in the linear regime of the $U_s - v$ relation shown in Figure 3.2b. It should be noted

that the analysis holds true for other values of ε_c too. For simplicity, each layer is chosen to have equal length $1/N$. This assumption can be relaxed very easily, as the procedure is not affected by length of individual layers.

Typical Results

Figure 3.17a shows a typical $X - t$ plot for a sample impact problem. In this calculation, the composite is made of $N = 20$ layers with ε_c decreasing linearly from 0.6 to 0.2 along the length of the target. The region $X \in [0, 1]$ denotes the impactor, while the layered target occupies $X \in [1, 2]$. The vertical black lines denote layer material interfaces. The ends $X = 0$ and $X = 2$ have traction free boundary conditions, while the flyer-target interface $X = 1$ is free to separate. The red lines in the $X - t$ diagram denote elastic waves in the system while the bold black lines are the shock waves. Upon impact, three waves are generated - a compressive elastic wave receding back into the flyer, a compressive elastic wave and a compression shock wave propagating into the first layer of the shock wave. The moment of impact is marked $t = 0$, and the simulation starts from there.

As per the stated assumption, the target is assumed to be homogeneous to elastic waves. Hence the elastic wave propagates unimpeded into the target. The compression shock interacts with the material interfaces and gives off backward propagation elastic waves in the target, called *scattered elastic waves*. The two branches of the stress strain curve have the same slopes, which by design, restricts the speed of the shock wave $\dot{s} \leq c$. Since the compliant strain ε_c is decreasing, the scattered elastic waves are compressive in nature, thereby further loading the material. The elastic wave generated in the target upon impact travels faster than the shock, reflects off the free edge of the target as a tensile wave, and interacts with the shock. This interaction in turn leads to the formation of two elastic waves (one forward moving and one backward) and a shock wave. The forward moving wave again travels unimpeded, reflects off at the target's end $X = 2$, and comes back to interact with the shock. This means that the interaction of type 7(b) happens over and over again until the shock changes its direction. Similarly the leading elastic wave generated in the flyer upon impact reflects off the free end $X = 0$ as a tensile wave. This wave is called the *first release wave* and interacts with the backward propagating elastic wave generated during the scattering process.

One of the most commonly used tools to investigate shock waves in a medium is to measure particle velocity profiles at the free surface of the target, $X = 2$ in the

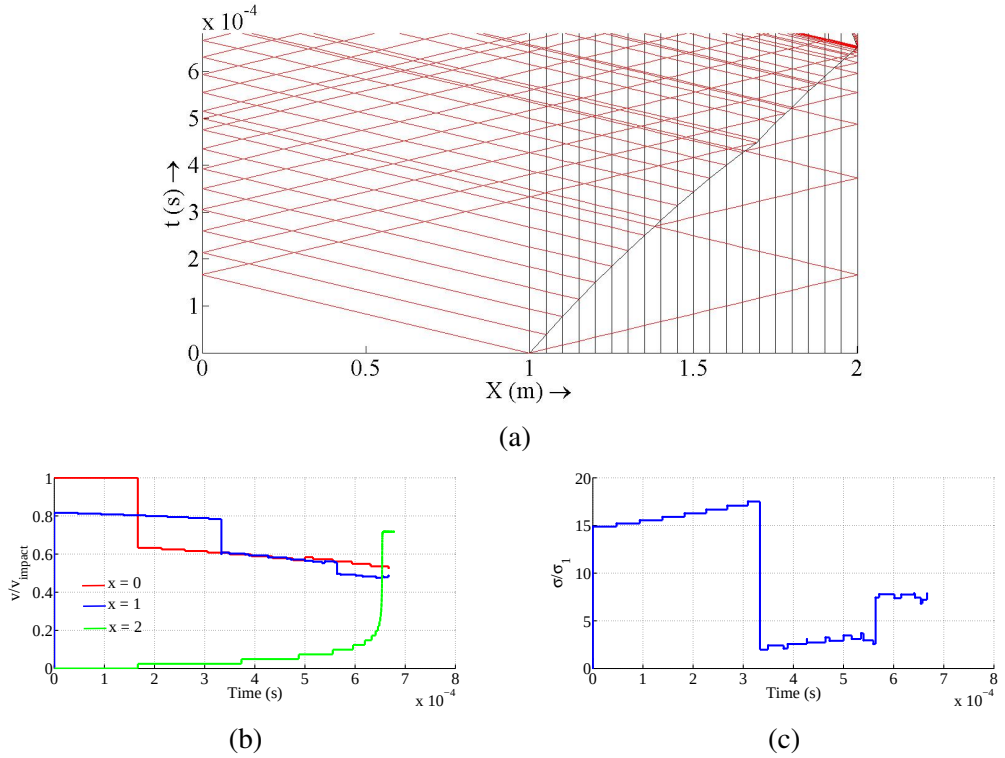

Figure 3.17: Impact problem for $L_0 = 1m$ and ε_c decreasing linearly. (a) $X - t$ diagram of the impact problem. The red lines correspond to the elastic waves while the black line is the propagating shock wave. (b) Particle velocity profiles at $X = 0$ (left edge of the flyer), $X = 1$ (flyer-target interface) and $X = 2$ (right edge of the target). (c) Stress profile at the flyer-target interface. The sudden drop in stress denotes the arrival of the release wave from the free edge of the flyer.

present case. Typically, velocity interferometry (VISAR) or Doppler velocimetry (PDV) is used to generate particle velocity profiles. As explained in Section 2.4, velocity profiles are useful in interpreting shock rise times, peak stresses, scattering and shock speeds. Figure 3.17b shows the normalized particle velocity profiles at $X = 0$, $X = 1$ and $X = 2$. The profile at $X = 0$ starts at v_{impact} and drops as soon as the elastic wave from the impact reaches the free end of the flyer. The corresponding release wave interacts with every scattered elastic wave coming from the scattering process, reducing their intensity. The profile at $X = 1$ shows a drop in particle velocity as soon as the release wave hits the flyer-target interface.

The profile at $X = 2$ shows increase in particle velocity with every reflection of an elastic wave. By design of the problem, the shock does not slope or round towards the leading and trailing parts of the profile. This is because the rarefaction wave fan that occurs in a Hugoniot is collapsed on to a single sharp elastic wave front in this

case. As such the particle velocity profiles are consistently sharp throughout this analysis.

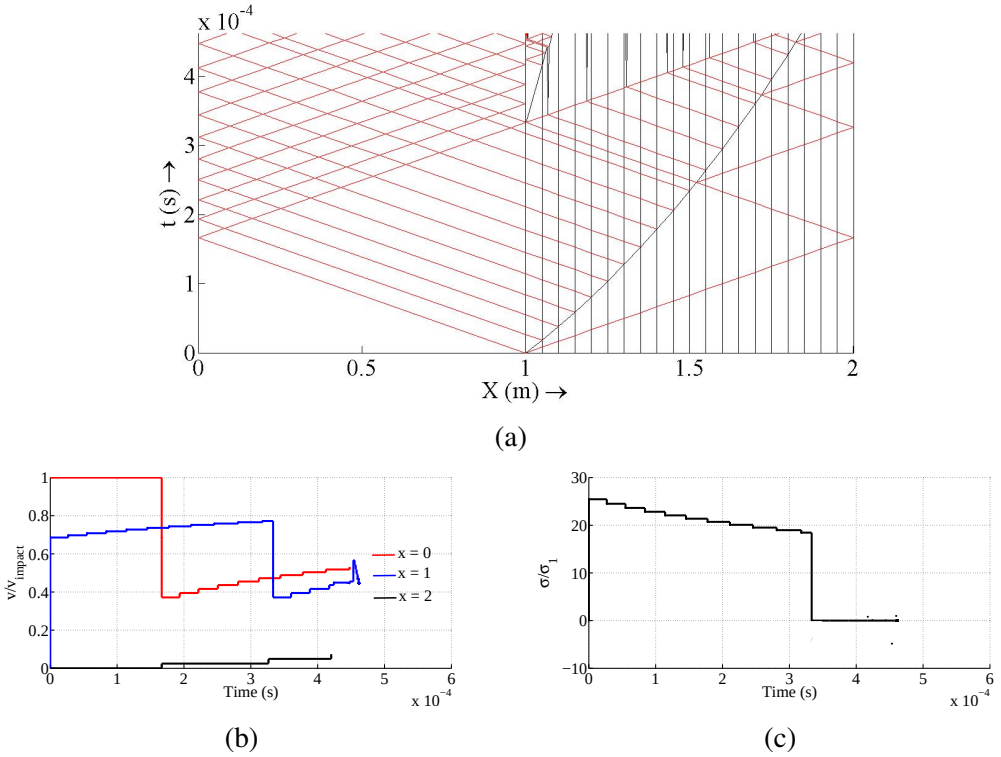

Figure 3.18: Impact problem for $L_0 = 1m$ and ε_c increasing linearly. (a) $X - t$ diagram of the impact problem. (b) Particle velocity profiles at $X = 0$ (left edge of the flyer), $X = 1$ (flyer-target interface) and $X = 2$ (right edge of the target). (c) Stress profile at the flyer-target interface. The sudden drop in stress denotes the arrival of the release wave from the free edge of the flyer.

Similar results are presented in Figures 3.18a, 3.18b and 3.18c for the case when ε_c increases linearly from 0.2 to 0.6 along the length of the target. For the same initial impact speed, the first layer in the composite of Figure 3.18a is less compliant than the one in Figure 3.17a. As such, the initial stress is higher in this case as represented in Figure 3.18a. Additionally, the scattered elastic waves in this system are of unloading nature. These waves upon interaction with the release wave from the flyer's free end, further strengthen the unloading nature of the release wave. Upon interaction of the release wave with the flyer-target interface, the interface separates creating a free boundary condition. This is evident by the stress drop at $X = 1$ at $t \approx 0.33$ ms. As the release wave travels further into the target, it interacts with the scattered elastic waves and produces a pair of tensile shocks at every interaction. Under certain conditions, the stress state can be tensile in the

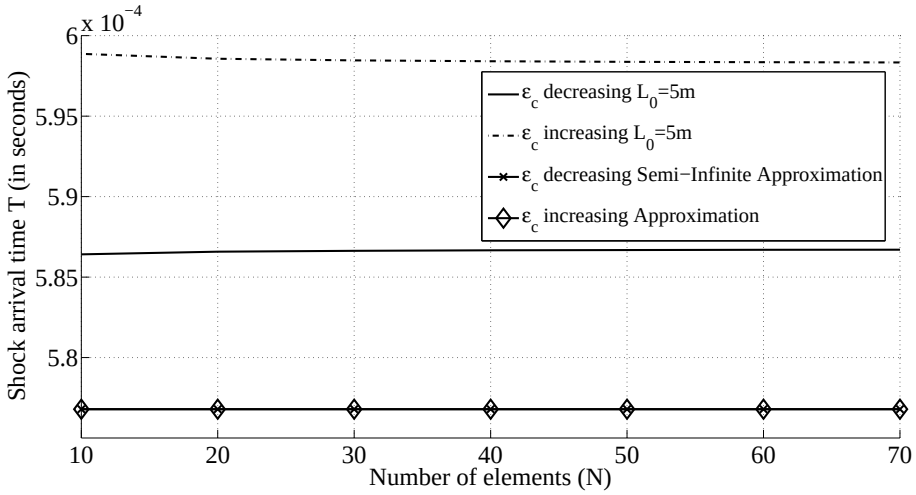

Figure 3.19: Variation of arrival times T with number of layers N for different layer profiles

region enclosed by this pair of shock waves leading to possible spallation. This will be covered later.

Effect of reflected waves

Shock arrival times

The arrival time T for a shock is defined as the time taken by the shock to reach the free edge of the target. By design, the shock wave is always preceded by an elastic wave which constantly reflects off the free edge of the target, interacts with the shock and produces more elastic waves. Hence, the shock never actually reaches the free edge of the target. So in this case, T is taken to be the time compression shock wave takes to change its direction and becomes a tensile shock. Figure 3.19 shows the variation of T with number of layers N. Here the length of the impactor is taken $L_0 = 5$ m, to prevent the release waves from entering into the target and interacting with the shock wave. The effect of release waves will be studied later.

For comparison, the arrival times are also plotted for a semi-infinite medium. Here the arrival time is defined as the time taken for the shock to travel 1m length in the target. It should be noted that the arrival time here is independent of the number of layers in the medium. Additionally, the arrival time is independent of the profile of ε_c. This is because the target is made of layers with identical thickness and the chosen ε_c profiles are linear. For a general case, the arrival time will depend on the ε_c profile in the target. A general observation that can be made from Figure 3.19 is that the reflected waves slow down the shock, thereby increasing T. This is because the

reflected waves are of unloading nature. Second, the point of interaction becomes important as the symmetry of the system is broken. This is because the shock speed reduces as the target becomes progressively compliant. As such, the point where the reflected wave interacts governs the Riemann solution and subsequent structure.

Alternate nonlinear and linear materials

The effect of reflected waves is highlighted when the contrast between the layers is increased. In this section, an alternate arrangement of linear and nonlinear material is considered. Given an even number N, a target of $N-1$ layers is constructed such that the first and last layers are made of nonlinear material. This results in a total of $N/2$ nonlinear layers and $N/2-1$ linear layers. The total length of the laminate is kept at 1 m, and every layer is of equal length. Further, the nonlinear layers have identical compliant strain, while the linear layers have the same E and ρ as the nonlinear layers. Figure 3.20a and 3.20b show the variation of normalized particle velocity profile with N for $\varepsilon_c = 0.2$ and $\varepsilon_c = 0.6$, respectively.

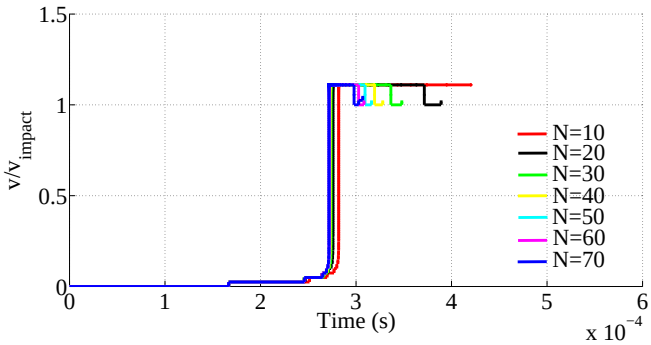

(a)

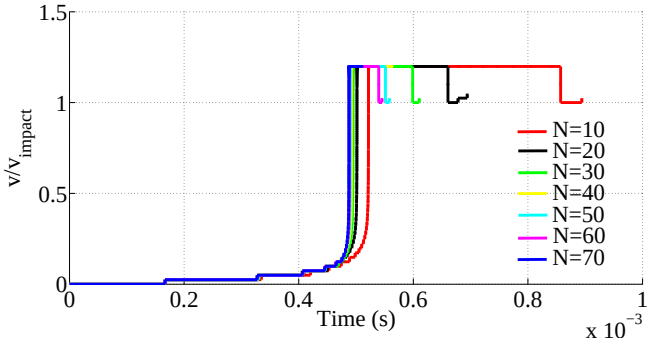

(b)

Figure 3.20: Variation of particle velocity profile at the free edge of the target with N for an alternate linear and nonlinear material. The first layer is chosen to be nonlinear with (a) $\varepsilon_2 = 0.2$ and (b) $\varepsilon_c = 0.6$.

In general, the arrival time for $\varepsilon_c = 0.6$ is larger because the material is more compliant, and hence has a lower shock speed. This is evident in the profiles in Figure 3.20a and 3.20b. In this kind of layer arrangement, the reflected elastic wave can interact with either the shock wave or an elastic wave depending on whether the interaction happens in a nonlinear layer or a linear layer. This would lead to different particle velocity profiles. The periodicity of the laminate is marked by the oscillations in the particle velocity profiles after the peak value is achieved. This is from the scattering of the shock wave on its way back after reflection. It can be seen from Figure 3.20a and 3.20b that as N increases the arrival times T decrease. This means that the effective speed of the shock increases with increasing N. This is interesting because the total length of the elastic layers remains the same with N. This is purely a consequence of increasing heterogeneity and number of interfaces in the material - which affects the interaction of reflected waves with shock waves.

Influence of ε_c profiles

In this section, the effects of ε_c profiles will be studied. In order to avoid interaction with release waves, the impactor length is kept long: $L_0 = 5m$.

Linear ε_c profiles

Figure 3.21a and 3.21b show the variation of particle velocity profiles with N for a material with ε_c varying linearly along the material. The particle velocities overlap for different N, indicating marginal effect of number of layers on the profile. This is corroborated by Figure 3.19 showing variation of arrival times T with N.

Power law profiles

The compliant strain ε_c for a layer i is chosen according to the following power law

$$\varepsilon_c^i = a + b\left(\frac{i-1}{N-1}\right)^n, \qquad i = 1, \ldots, N \tag{3.19}$$

where $a = 0.2$, $b = 0.4$ for ε_c increasing case and $a = 0.6$, $b = -0.4$ for ε_c decreasing case. Figure 3.22a and 3.22b show variation of particle velocity profiles with n for ε_c decreasing and increasing respectively. The number of layers is taken to be 20 for these calculations. It is observed from Figure 3.22a that as n increases, the arrival time increases. This can be explained from the analysis in Section 3.3. The speed of the shock increases as ε_c decreases. As the exponent n increases, the increase in shock speed happens more slowly. This can also be used to explain

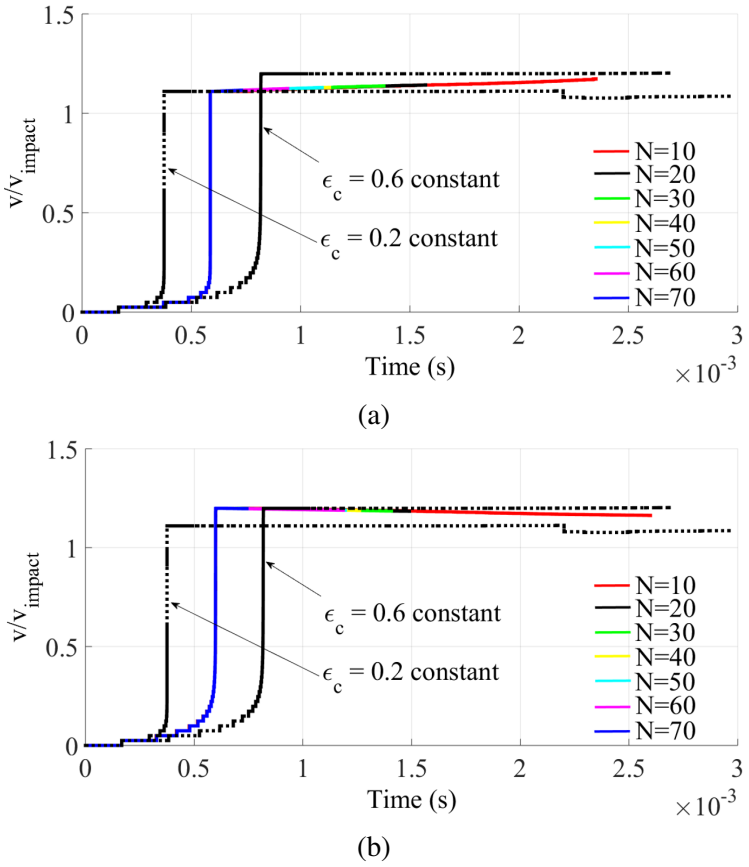

Figure 3.21: Variation of particle velocity profiles with N for (a) linearly decreasing and (b) linearly increasing ε_c profile. Profiles for constant $\varepsilon_c = 0.2$, 0.6 are plotted for comparison.

increase in effective shock speed with n in Figure 3.22b. Here the decrease in shock speed happens more slowly along the length of the material as the exponent n increases.

Step ε_c profiles

Next, a step ε_c profile along the material is considered. Material of length 1 m is considered with $N = 20$ layers. For $X \in [0, \lambda)$, ε_c takes a constant value (0.2 in ε_c increasing case and 0.6 in ε_c decreasing case), while another constant value for $X \in [\lambda, 1]$ (0.6 in ε_c increasing case and 0.2 in ε_c decreasing case). Figure 3.23a and 3.23b show the variation of normalized particle velocity profiles with λ for ε_c decreasing and increasing respectively. Profiles for constant $\varepsilon_c = 0.2$ and $\varepsilon_c = 0.6$ are plotted for comparison. For the decreasing case, the arrival times increase with increasing λ. This is consistent with the analysis in Section 3.3 where the shock speed decreases with increasing ε_c. In both cases, ε_c = constant profiles bound the

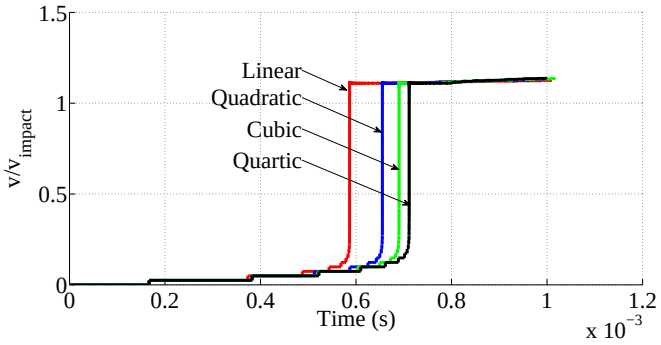

(a)

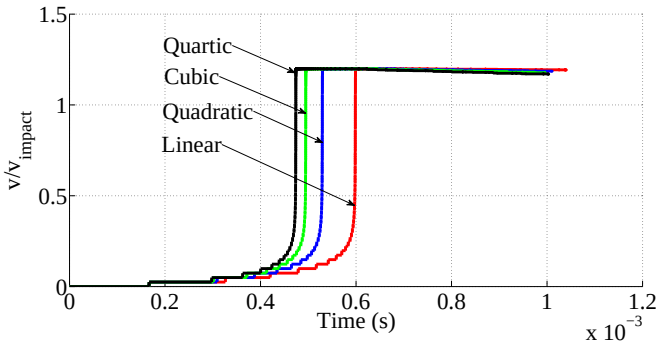

(b)

Figure 3.22: Variation of particle velocity profiles with the exponent n for (a) ε_c decreasing and (b) ε_c increasing profiles.

λ dependent profiles.

Periodically nonlinear material

The role of the ε_c profile is further explored by considering a periodic layering of nonlinear materials. Figure 3.24a and 3.24b show the variation of normalized particle velocity profiles with N for alternate $\varepsilon = 0.6$, 0.2 and $\varepsilon_c = 0.2$, 0.6 layers respectively. It is observed that the arrival times are not affected by N or the arrangement of ε_c layers. The difference is observed in the subsequent profile structure. Unlike the case studied in Section 3.6, the arrival times here are almost identical with N. This is because the reflected elastic waves in the material described in Section 3.6 interact with either an elastic wave (in a linear material) or a shock wave (in a nonlinear material). In this case, the reflected waves interact with just shock waves, which has a marginal effect on arrival times. This can also be seen in Figure 3.19. The subsequent oscillations are a consequence of shock wave scattering on its way back into the target after reflection near the free edge of the target.

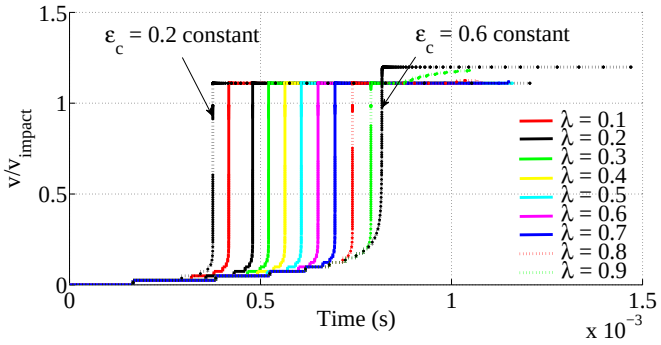

(a)

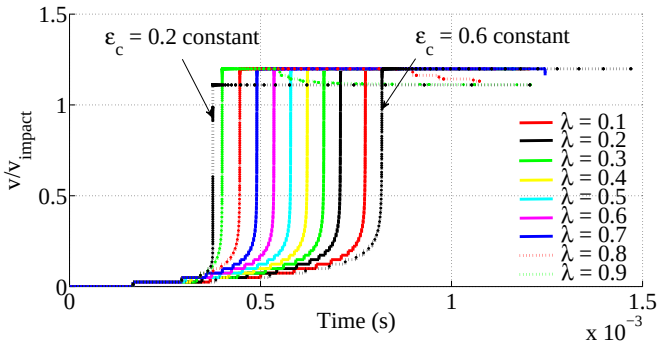

(b)

Figure 3.23: Variation of particle velocity profiles with λ for (a) ε_c decreasing and (b) ε_c increasing profiles.

Effect of release waves

As observed in Figure 3.17a and 3.18a, the elastic wave generated in the flyer upon impact reflects off the free edge as a tensile wave. This release wave then interacts with scattered waves and the shock wave as it travels through the flyer and into the target. As explained in Section 3.6, the unloading nature of the release wave can be attenuated or amplified by the nature of scattered elastic waves. If the scattered waves are also of unloading nature, the unloading nature of the release wave is amplified and it leads to flyer-target interface separation and subsequent pairs of tensile shocks (Figure 3.17a). Note that in a real Hugoniot, the unloading waves are replaced by rarefaction wave fans. As such, the interaction of the release wave becomes quite complicated. In this section, the effect of release waves is considered by taking the length of the flyer $L_0 = 0.5m$. The short length of the flyer allows the release wave to catch up with the shock.

Figure 3.25a and 3.25b show the $X - t$ diagram of the impact process with a thin ($L_0 = 0.5m$) impactor upon a layered target, $N = 2$ and $N = 20$ respectively, with

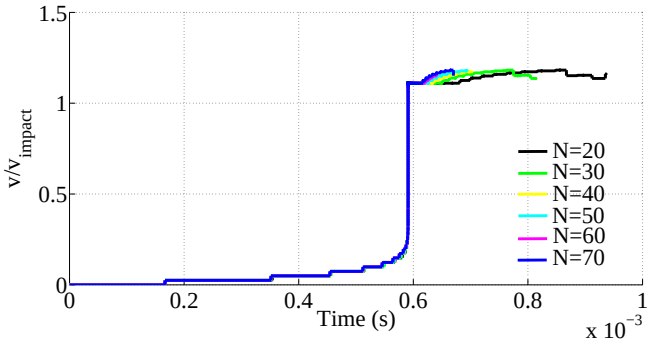

(a)

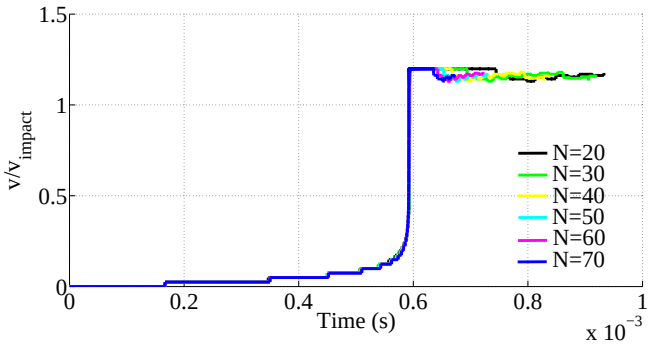

(b)

Figure 3.24: Variation of particle velocity profiles with N for alternate layering of (a) $\varepsilon_c = 0.6$ and 0.2 (b) $\varepsilon_c = 0.2$ and 0.6.

ε_c increasing linearly along the length. In both cases, the total length of the target is $1m$ and the first layer has an $\varepsilon_c = 0.6$ while the last layer has $\varepsilon_c = 0.2$. The difference lies in the gradient of ε_c along the target. In both cases, the release wave causes the flyer-target interface separation upon its return. As explained in Section 3.3, the scattered elastic waves will be of unloading nature. Due to the large contrast between layers for $N = 2$, the scattered elastic wave will have a very strong unloading nature as compared to any scattered wave in the $N = 20$ case. It can be seen from Figures 3.25a and 3.25b that the pair of tensile shocks formed in $N = 2$ have higher speeds, and therefore greater strength, as compared to those in $N = 20$. In this case, the state of stress within the zone in the $X - t$ plane enclosed by the pair of tensile shocks is negative. This leads to the possibility of spallation in the material, if the tensile stress exceeds the spallation strength.

Spallation is an important failure mechanism caused by tensile waves reflecting off the free edge of the material. Spallation has been extensively studied (ref. Bushman [15] and references therein). It has been shown by Erzar et al. [29], Vogler and

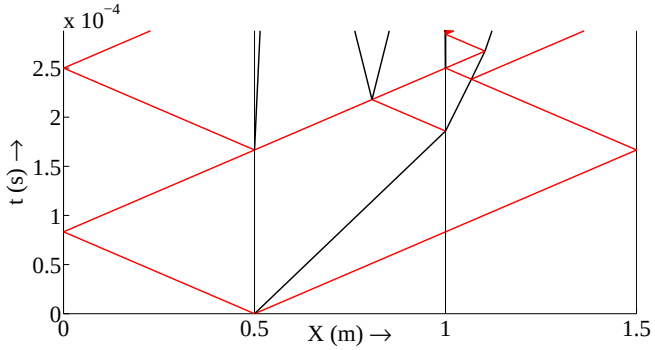

(a)

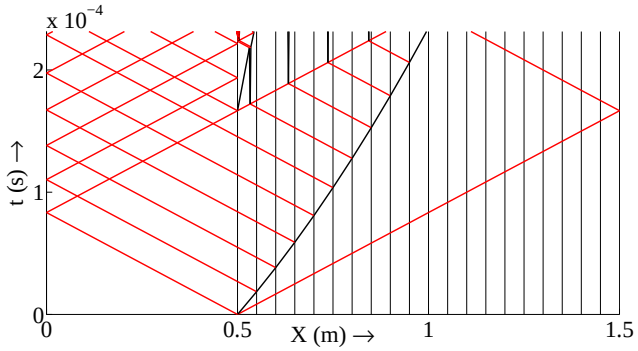

(b)

Figure 3.25: $X-t$ diagram for the impact process on a layered target with (a) $N = 2$ and (b) $N = 20$, where the ε_c increases linearly for both cases. A pair of tensile shocks is observed in both cases, with stronger shocks for $N = 2$.

Clayton [80] and Wang et al. [81] that the quantities associated with spallation such as the location of spall plane and the critical stress can be significantly influenced by internal stress variations. In the case shown in Figure 3.25a, the spallation can be caused by high contrast between layer properties and the subsequent scattered waves.

Dissipation

Shock waves are dissipative by nature. The dissipation, as explained in Section 3.2 from Figure 3.2a, is the difference between area $\Delta 3PQ$ and $\Delta P21$. Since the states across an elastic wave lie on the same branch of the stress strain curve, these waves do not cause any dissipation. The maximal dissipation kinetics followed in this analysis ensures that the stress state ahead of the shock is σ_1. Figure 3.26 shows the variation of total dissipation in the layered material with N for two different layer arrangements. In order to avoid the effect of release waves, the flyer length is taken to be $L_0 = 5m$. The total dissipation shows nominal variation with N. This

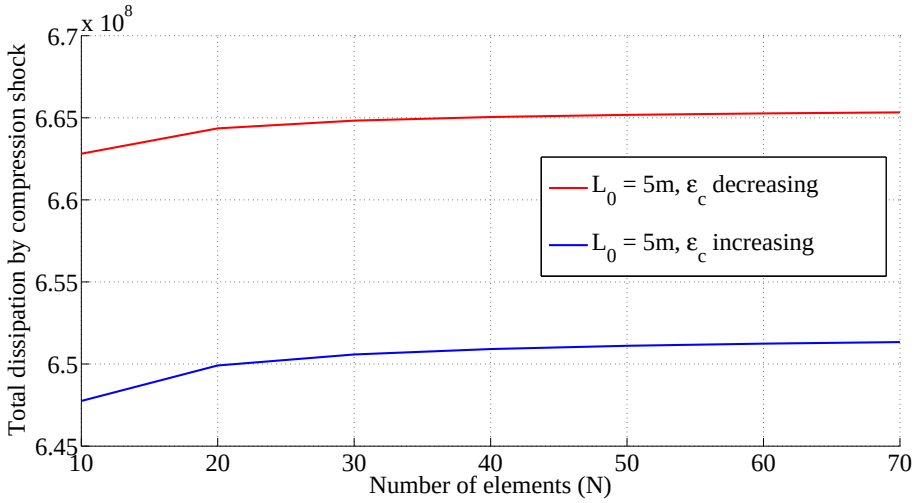

Figure 3.26: Variation of total dissipation in the material with N for different ε_c arrangement. The flyer length is chosen to be large to avoid the effect of release waves. The dissipation is higher for the layer arrangement with ε_c decreasing linearly along the length.

is consistent with the observations in Figure 3.19, where the arrival times do not show much dependence on N. The effective shock speed is higher for ε_c decreasing case as shown in Figure 3.19. Due to maximal dissipation kinetics, the higher shock speed implies larger dissipation. Hence, the observations in Figure 3.26 are consistent with the analysis so far.

3.7 Extensions and relaxing assumptions

In order to make the analysis simple in the previous sections, the material parameters such as σ_1, ρ and E were assumed to be same for all layers. Further, both branches of the stress-strain curves were assumed to have the same slope E. This allowed only one elastic wave speed, and hence only one kind of elastic wave, in the system. This section will focus on the consequences and the associated physical interpretations of relaxing these assumptions. Relaxing the assumptions increases the complexity of the system by introducing more classes of Riemann problems. The analytic solutions of every class can be obtained by a similar procedure as outlined in Section 3.3. The remaining challenge is to identify the Riemann problems, tweak the algorithm to search for those Riemann problems, and introduce new waves according to those solutions.

An immediate extension lies in changing the slopes of the two branches of the stress strain curves - E_1 and E_2. This introduces two kinds of elastic waves into

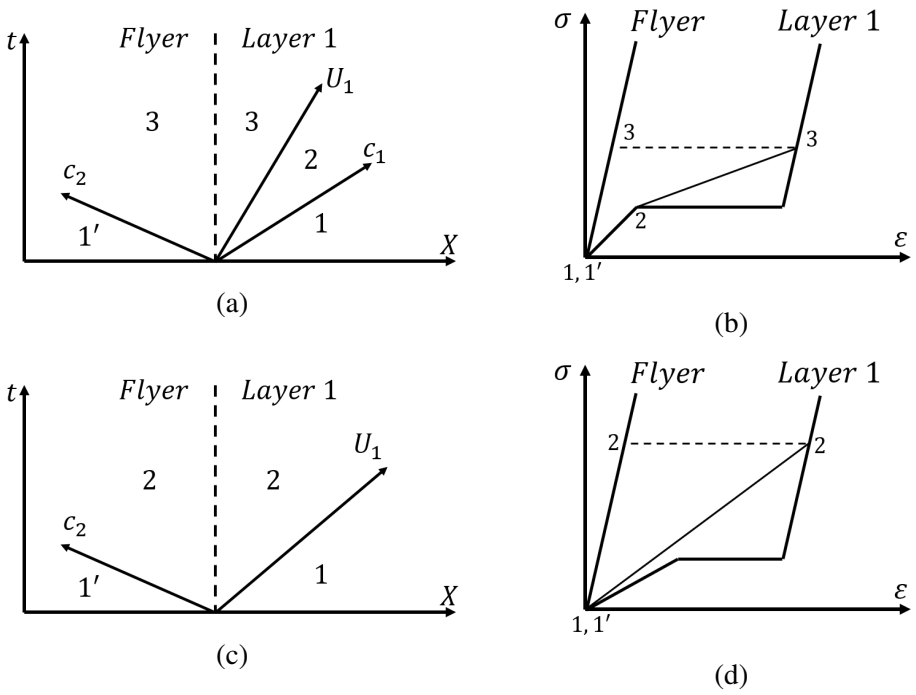

Figure 3.27: Potential solutions for initial impact on a layered composite with the modified piecewise affine stress-strain curve. For small impact speeds, the maximal dissipation kinetics ensures (a), (b) a two wave structure. For high impact speeds (c), (d) a single shock wave is sufficient for a unique solution.

the system with wave speeds $c_1 = \sqrt{E_1/\rho}$ and $c_2 = \sqrt{E_2/\rho}$ respectively. The stress states across the wave with speed c_1 (c_2) lie on the first (second) branch of the stress strain curve. This extension allows better approximation of the Hugoniot, provided $c_2 > c_1$. The introduction of the second kind of wave speed removes the fundamental constraint that the shock speed $\dot{s} < c$ associated with the earlier model. Now, the shock speed can be greater than c_1 though it still needs to be less than c_2. Figures 3.27a and 3.27c show the $X - t$ diagram of two potential solutions for the initial impact Riemann problem. This is a consequence of the compatibility relations and the maximal dissipation kinetics. For low impact speeds, the maximal dissipation kinetics ensures a two wave structure - a shock wave preceded by an elastic wave of speed c_1. Figure 3.27b shows this process in the corresponding stress-strain space. This is similar to the cases dealt with earlier. For high impact speeds, due to the difference in slopes of the stress-strain branches, a single shock wave is sufficient to obtain a unique solution. Figures 3.27c and 3.27d show this solution in $X - t$ plane and $\sigma - \varepsilon$ plane.

It can also be noticed that in this case, the shock is no longer preceded by an

elastic wave. This may or may not hold as the shock travels through the material and interacts with layer interfaces. Again, there will be two potential solutions depending upon the stress states and the material contrast. For example, in the case where ε_c decreases along the length, the shock strength will increase and the shock will produce c_2 waves of loading nature as it traverses into the material. The shock will not be preceded by an elastic wave and it can interact with the free surface to form a tensile shock. The Riemann problems there can again be solved by similar methods.

Another important extension is assigning different ρ and c values for different layers. This corresponds to the impedance difference between the layers in a typical arrangement. Relaxing this assumption essentially removes the elastic homogeneity assumption in the analysis. This leads to the addition of a Riemann problem of an elastic wave scattering at a material interface. This introduces more elastic waves into the system and more interactions of shock wave with scattered and reflected elastic waves. Additionally, the σ_1 parameter that corresponds to the σ_{HEL} can vary with the layer. This adds a few Riemann problems such as an elastic wave in one nonlinear layer potentially leading to a shock in another nonlinear layer.

3.8 Conclusions and discussions

In this chapter, the phenomenon of shock wave propagation through a heterogeneous medium is explored by studying a simplified problem of impact on a layered medium. The propagation of shock waves through a homogeneous medium has been extensively studied. Even though the interaction of a shock wave through a single interface has been studied [23], open problems pertaining to the overall effect remain in the case of a heterogeneous medium. In this chapter, the overall effect of heterogeneity and scattering is explored through multiple interfaces. The framework introduced by Knowles [44] is followed in the analysis presented. This is complemented by showing the connection between the Knowles approach and the conventional approach of specifying a linear relation between shock speed and particle velocity.

The layered target is assumed to follow a piecewise affine stress strain curve. This collapses the rarefaction wave fan observed in the Hugoniot into a single moving discontinuity. This ensures that the states (σ, v, ε) are piecewise constant in the $X-t$ plane, and thereby ensures that only Riemann problems occur in the system. The method classifies all possible Riemann problems in the system and analytic solutions

are obtained for every class of problem. As a consequence, the task reduces to following waves in the medium. In order to focus on the scattering of shock waves, the layered target is assumed homogeneous to elastic waves. The algorithm uses object oriented programming to track existing waves, look for possible interactions, solve them and introduce new waves into the system. While there are other powerful numerical methods to study shock wave propagation in one or higher dimensions, the method presented in this chapter provides insight into each and every interaction. Additionally, the method provides information into a broad range of phenomena. The method is independent of spatial and temporal resolutions and reconstructs the complete picture through exact solutions of individual interactions. As such, it can be useful to benchmark different numerical studies.

The assumption of elastic homogeneity in the composite restricts the heterogeneous nature to shock waves. This removes the scattering of elastic waves in the system. This process can be reintroduced by changing the moduli of the layers, and correspondingly adding more Riemann problems. The scattering of elastic waves will add structure in the particle velocity profiles at the free end of the target, due to internal reflections in the last layer. The assumption of same modulus for the two branches of stress strain curve ensures only one type of elastic wave in the system. While this simplifies the analysis, the piecewise linear curve can deviate from the actual Hugoniot beyond a certain strain. The analysis can be extended to allow different modulus for different branches by introducing more Riemann problems. The shocked region is compressed and has higher modulus. This ensures that the analysis remains valid for much larger strain values. This also allows the shock speed to be greater than the elastic wave speed corresponding to the lower modulus branch. This is also referred to as an overshocked condition. Similarly, other quantities such as density and yield stress can be chosen differently for different layers by introducing even more Riemann problems.

The idea of damage mitigation through shock attenuation is explored by studying a layer arrangement corresponding to decreasing stiffness (or increasing compliant strain ε_c). A simplified case of a semi-infinite medium is studied in Section 3.4 where reflections of elastic waves are ignored to focus on the shock wave scattering. Interestingly, it is observed that the shock speed in the N^{th} layer depends on the material properties of the first and the N^{th} layer. The effective shock speed (studied as the arrival time T of the shock), being the harmonic mean of shock speeds in individual layers, depends on the layer arrangement. The assumption of linear

profile and equal layer thickness for the semi-infinite case makes the arrival time T independent of the layer arrangement and ε_c profiles (Figure 3.19). This is not true for general cases.

The case of finite medium allows for reflections of elastic waves at the free edges of the target and the flyer. In order to focus on the effect of reflected waves from the free surface of the target, the reflections from the flyer free edge are ignored by taking a long flyer. The reflected waves are of unloading nature, and slow down the shock upon interaction. Although individual interactions of reflected waves off the free edge of the target cause nominal changes in the shock speed, repeated interactions can significantly influence the overall shock propagation (Figure 3.21a and 3.21b). Different layer arrangements are also explored and their consequence on the particle velocity profiles are studied. Keeping the overall target length, impact speed and impactor length the same, it is observed that the profiles can vary depending upon the heterogeneity of the material.

The release waves (reflected waves from the free edge of the flyer) have significant influence over the material behavior (Figures 3.25a and 3.25b) . These waves are of unloading nature and travel through the flyer, enter the target and interact with the shock. The target layer arrangement plays a crucial role in this analysis. As the shock propagates into the target, it interacts with the material interfaces and produces scattered elastic waves which travel backwards into the target. Depending upon the layer arrangement, the scattered waves can be of unloading nature (Section 3.3) and can increase the unloading nature of release waves upon interaction. This can lead to the possibility of spallation if the contrast between the layers is large and sudden, as explained in Section 3.6. As such, the design for shock attenuation, which involves progressively decreasing layer stiffness, may lead to spall fracture if the property gradient is large (Figure 3.25a). The overall dissipation is also monitored in the material. The overall dissipation is higher in a material if the effective shock speed is larger. This is a direct consequence of the maximal dissipation kinetics used in the analysis. Further, the dissipation increases with increase in the number of interfaces and hence, increased scattering.

An important observation to note is the lack of any structure in the shock in the analysis. The particle profiles presented in this chapter consistently show a series of elastic precursors (corresponding to the reflected waves off the target free edge) followed by a sharp spike corresponding to the reflection off the shock wave from near the free edge. This is consistent with the recent observations made by Rauls

[65]. It should be noted that if the piecewise affine stress strain curve is replaced by a Hugoniot, the rarefaction wave fan would result in the formation of a structured particle velocity profile. The complex interaction between a forward moving shock and a backward moving rarefaction wave would lead to a formation of a structured particle velocity profile at the free edge of the target. In case of periodically layered materials, the analysis presented in this chapter shows oscillations in the particle velocity profiles, which is consistent with the experimental observations made by Zhuang [89] and the numerical studies by Chen [18].

Chapter 4

PULSED POWER GENERATION IN FERROELECTRIC MEDIUM

[1] Vinamra Agrawal and Kaushik Bhattacharya. "Impact induced depolarization and electro-thermomechanical coupling of ferroelectric materials". In: (2016). (To be submitted).

In this chapter, the nonlinear electro-thermomechanical coupling of a ferroelectric material is explored. The application in consideration is a pulsed power generator which uses a ferroelectric material under shock loading to generate a large current (or voltage) pulse for a short duration of time. The electro-thermomechanical coupling of the material plays a central role in causing a mechanically induced electrical phase transition in the material leading to a sudden discharge of bound polarization in the material.

4.1 Ferroelectric materials and pulsed power generation

Ferroelectric materials are the electric analogs of magnets: they are spontaneously electrically polarized. Thus ferroelectric materials develop a potential difference across them when they are kept in an open-loop configuration. The amount of polarization can change with applied electric field. Figure 4.1 shows a typical ferroelectric polarization vs. electric field loop. Note that the polarization is non-zero at zero electric field due to the spontaneous polarization. Note further that these materials are bistable, i.e., there are at least two states of spontaneous polarization.

All ferroelectric materials undergo a phase transformation at the Curie temperature: they are ferroelectric below this temperature, but become paraelecric or nonpolar above this temperature. Some ferroceramic materials also display a ferroelectric-antiferroelectric phase transformation. In the latter state, the material is polarized at the microscopic scale, but the polarization alternates at this scale resulting in a net-zero polarization at the macroscopic scale.

Ferroelectric materials are also a subclass of piezoelectric materials because they exhibit a electromechanical coupling. This means that upon application of mechanical loading, the material exhibits electrical output. Unlike conventional piezoelectric materials, the focus for ferroelectric materials lies under large deformations where

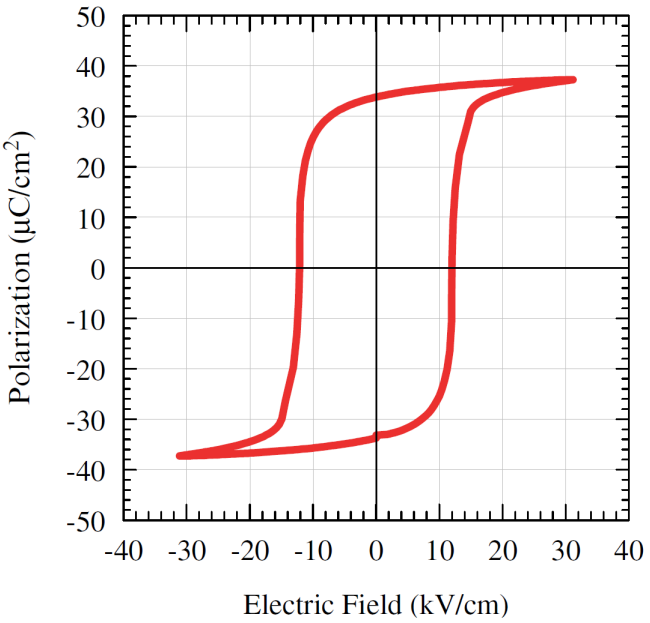

Figure 4.1: Characteristic curve of a ferroelectric material. At zero electric field, the material exhibits a non-zero polarization ($\approx 33\ \mu C/cm^2$ in this case).

the electromechanical coupling is highly nonlinear. Additionally, these materials also exhibit electrothermal coupling and hence are a subclass of pyroelectric materials. Due to the nonlinear electro-thermomechanical coupling, these materials can undergo electrical phase transition upon application of mechanical loading. Figure 4.2b shows the variation of the characteristic curves ($D - E$ loops) with applied hydrostatic stress [78]. Here D is electric displacement in the material, typically measured through charge. It can be seen that beyond a certain threshold stress, the $D - E$ loop closes. This corresponds to an FE-AFE phase transition in the material.

Ferroelectricity is found in a variety of materials. However, the commonly used ferroelectric materials like lead-zirconate-titanate (PZT) and barium-titanate ($BaTiO_3$) have a perovskite crystal structure. Ferroelectric materials have found a wide range of applications including as sensors, actuators, capacitors, and optical modulators. They are often used in their ceramic or polycrystalline form. While PZT most commonly finds applications as actuators and transducers, $BaTiO_3$ is commonly used for capacitors and electro-optic modulators (see [22], [42] and [85]). Although these materials exhibit strong nonlinearities under large loading, typical applications restrict themselves to the linear range of the ferroelectric response. This is due to the poor fatigue life of ferroelectric materials under phase transitions and the associated large electromechanical loading. Focusing on the linear range also avoids hysteresis

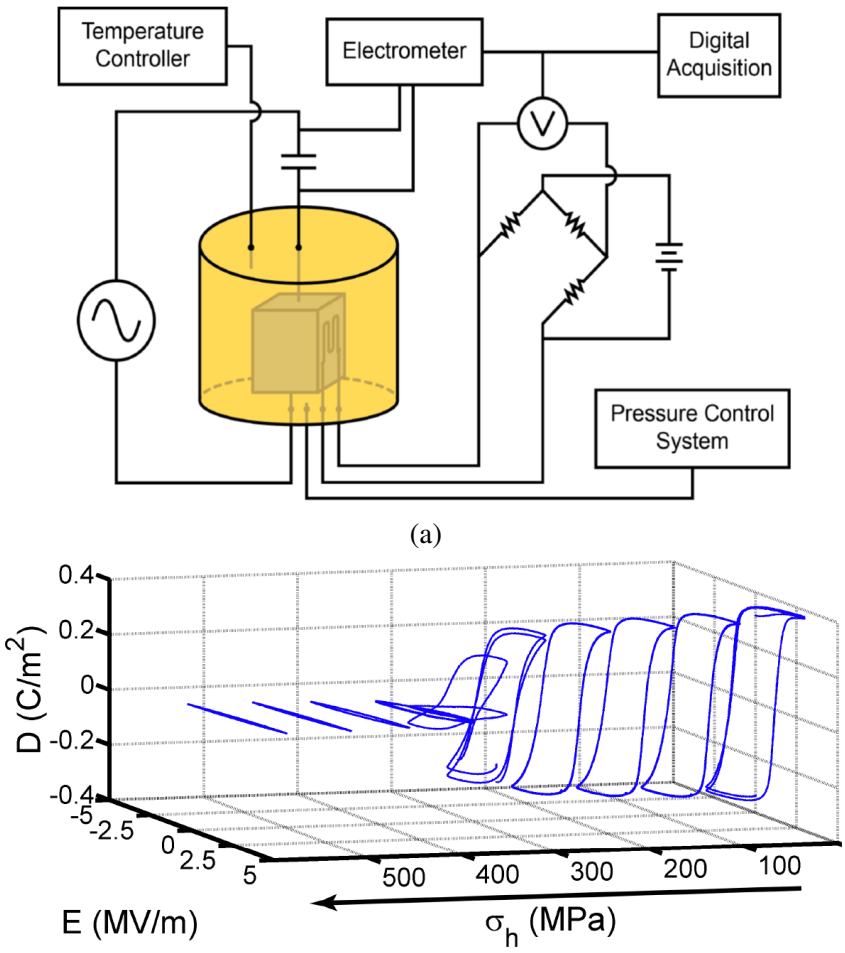

Figure 4.2: (a) Experimental setup for loading a PZT sample hydrostatically, and measuring $D - E$ loops. (b) Variation in the characteristic curve of a ferroelectric material upon application of hydrostatic pressure (Figures from [78]).

losses and the cyclic degradation of the material. In the experiment shown in Figures 4.2a and 4.2b, the material is subjected to large, albeit slow, mechanical loading. The closing of the loop is reflected in the electrical output, in the form of charge output, in the external circuit.

Ferroelectric generators (FEGs) employ ferroelectric ceramics to generate large pulses of electrical power for a short period of time [7]. The process of pulsed power generation in an FEG involves loading a ferroelectric material with a shock loading and inducing a phase transition in the material within a very short period. The shock loading is typically achieved by a high velocity impact or a blast. Figures 4.3a and 4.3b show the schematic of ferroelectric generators using plate impact and blast as loading mechanisms. The plate impact method is typically used in experiments

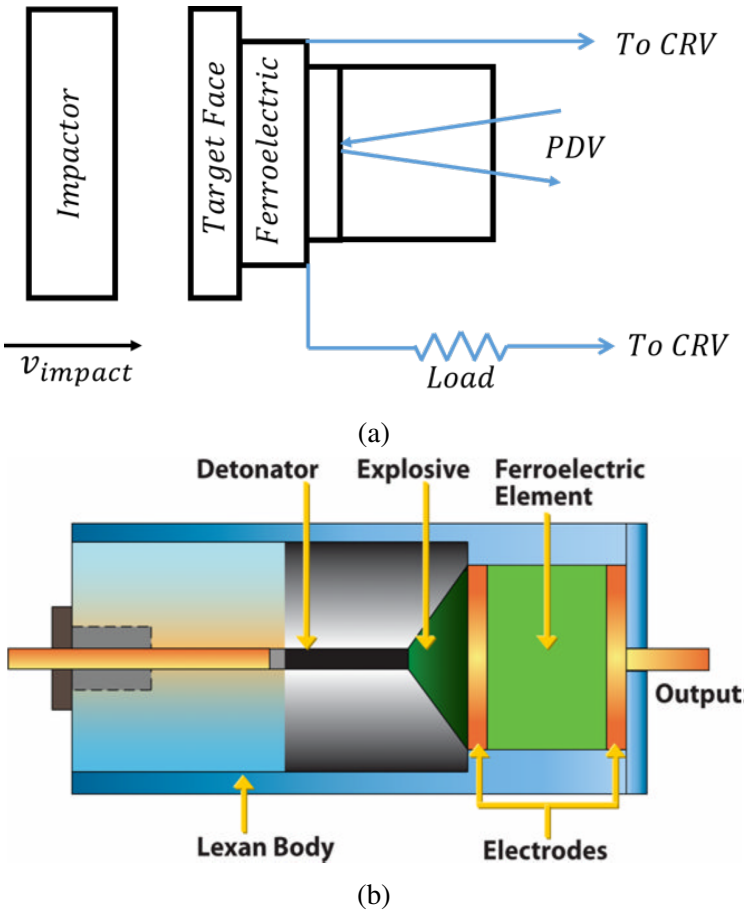

Figure 4.3: Schematic of ferroelectric generators providing shock loading to the material through (a) plate impact and (b) blast loading

due to ease of setup, control of loading amplitude and loading pulse. Depending upon the external circuit (or electrical boundary conditions), a large current (short circuit) or a large voltage (open circuit) output can be obtained. Under shock loading, a ferroceramic experiences high stress amplitudes and dynamic loading conditions. The associated electrical response is a consequence of either FE-AFE phase transitions or domain reorientation. The most commonly used ferroceramic used for FEG applications is PZT 95/5 (the ratio of Zirconium and Titanium being 95:5) doped with 2% Niobium, commonly referred to as doped PZT 95/5. The ferroelectric and antiferroelectric energy wells for a doped PZT 95/5 lie close to each other at room temperature, thereby allowing easy phase transitions at relatively low impact speeds. In the process of shock induced phase transitions, the material loses its remnant polarization. As such these experiments are commonly referred to as depolarization experiments.

Investigations on the electromechanical coupling of ferroelectric materials, such as PZT and $BaTiO_3$, were first carried out by Berlincourt [14]. The nonlinear effects due to domain reorientation in such materials were studied for high pressures. Quantities like open circuit voltage, short circuit charge and mechanical strains were measured under slow and rapid loading up to 400 MPa applied parallel or perpendicular to the poled direction. It was observed that the open circuit and short circuit response were significantly different. The charges developed on the electrode surface in the open circuit configuration prevented further domain reorientation. Plate impact experiments conducted by Halpin ([37], [38]) on short circuit axially poled PZT samples, showed an increase in current output with an increase in impact speeds. Three samples - normally sintered PZT 95/5, hot pressed PZT 95/5 and PSZT 68/7 were tested with polarization dipoles aligned opposite to the direction of the impinging shock. It was also observed that the pulse duration decreased with increasing impact speeds. Additionally, beyond a certain threshold impact speed, the current output declined. The effects of polarity in axially oriented PZT 65/35 samples were explored by Cutchen [21]. It was observed that the current output became more sensitive to stress fluctuations when the sample was poled in the direction opposite to the direction of shock propagation.

The dielectric breakdown of PZT 65/25 was explored by Lysne [52]. It was observed that a stress of 1 GPa was sufficient to cause dielectric breakdown in the material. Later, a model for dielectric breakdown was developed to explain experimental results [53]. In a separate experiment conducted on axially poled doped PZT 95/5 [54], it was observed that the properties of the unshocked material influenced the electric field ahead of the shock, which in turn affected the shock wave speed. The question about contribution from domain reorientation and phase transition into electrical output was addressed by Fritz [31]. It was observed that domain reorientation dominates for lower stress amplitudes, while at higher stress magnitudes the contribution is mainly through phase transition. Additionally, experiments conducted by Dick and Vorthman [27] on normally poled and unpoled PZT 95/5 samples showed the lack of dependence of point of phase transition and kinetics on the poling state of the material. These experiments were conducted for the short circuit case and with finite resistance in the extenal circuit.

Figure 4.4a shows the schematic of the experimental setup used by Furnish et al. [34]. The target was an axially poled PZT 95/5 with short circuit electrical boundary conditions. The impact speeds ranged from 65 m/s to 344 m/s corresponding to

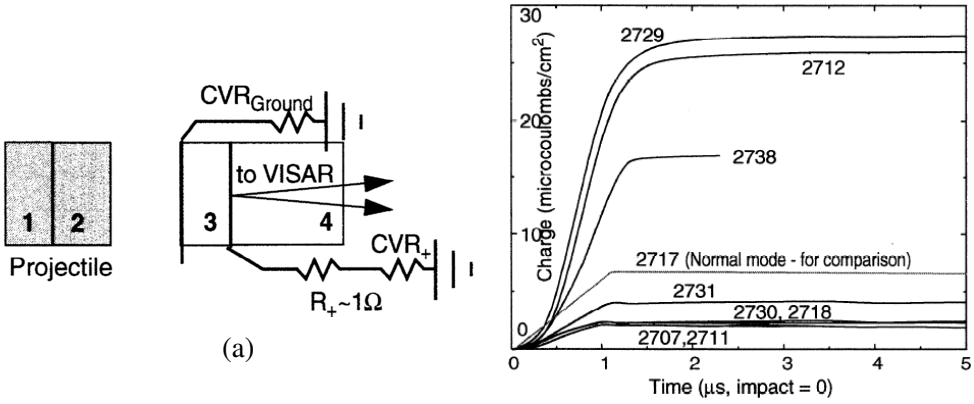

Figure 4.4: (a) Schematic of the experimental setup used by Furnish et al. [34]. (b) Charge profiles obtained through the external circuit. The numbers on top of the individual profiles denote different experimental runs. Parameters for each experimental run are available in [34].

stress amplitudes of 0.9 GPa to 4.6 GPa. A complete depolarization was observed at 65m/s impact speed. This corresponds to experiment number 2729 in Figure 4.4b. At higher speeds, the current output declined - as evident from the decline in the slopes of charge profiles. The reason for this decline was attributed to dielectric breakdown. In many detailed studies by Setchell ([69], [70] and [71]), Hugoniot profiles for unpoled doped PZT 95/5 were constructed. It was observed that the Hugoniot curve was sensitive to phase transitions and showed variation at the point of the phase transition. Further, onset of pore collapse of ferroceramic at higher impact speeds, was also evident in the Hugoniot curve. Hugoniot profiles were different for axially poled, normally poled and unpoled samples due to possible domain reorientation.

In the process of shock induced depolarization, the ferroelectric material undergoes large deformations in a highly dynamic environment. This requires accounting for the intertial effects in the material. Further, the process is adiabatic due to the fact that there is no time for heat exchange under shock loading. As such, the material enters into the highly nonlinear regime of electro-thermomechanical coupling. Despite the highly dynamic (and adiabatic) environment, it can be assumed that the electromagnetic processes happen at a faster time scale than the intertial processes. Physically, it means that the wave speeds in the medium are much smaller than the speed of light in the material. This is referred to as a quasi-static electromagnetic approximation. An important consequence of large deformations and large electric

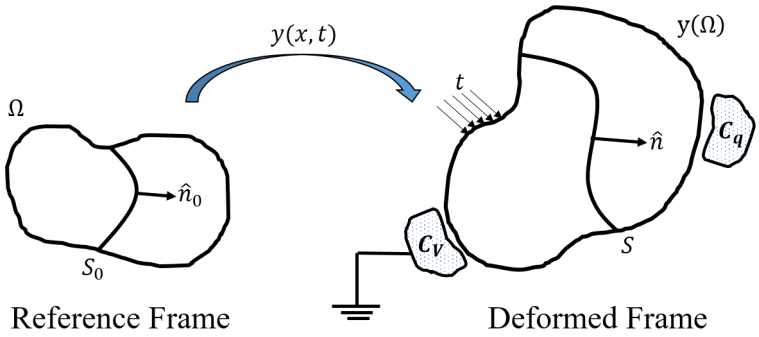

Figure 4.5: Continuum representation of the problem. The material is subjected to a generalized electromechanical loading in the deformed frame. A phase boundary propagates causing FE-AFE phase transition.

fields in the system is that the Maxwell stress starts to play a role in the analysis. Over the years, many studies have been undertaken to understand domain patterns and switching behavior using the phase field approach on a continuum level ([5], [6], [16], [39], [45], [48], [49], [60], [82], [86] and [87]) and using the atomistic approach ([20], [57]).

Despite being widely used, the continuum approach comes with its own limitation. The continuum phase field models are typically based on the work by Devonshire ([25], [24],[26]) and Toupin [77] where a ferroelectric material is modeled as an insulator. In reality, these materials are semiconductors with wide band gaps ([59], [68]). A continuum formulation for ferroelectric materials, as semiconductors, was presented by Xiao [84]. The formulation introduced dopant density and volumetric charge density to account for semiconducting behavior. In the next section, a large deformation dynamic behavior analysis for ferroelectric materials is presented to study the shock induced phase boundary propagation process.

4.2 Continuum formulation

Preliminaries

We consider a ferroelectric medium occupying a region $\Omega \subset \mathbb{R}^3$ in the Lagrangian frame as shown in Figure 4.5. The system is subjected to a deformation $\mathbf{y} : \Omega \to \mathbb{R}^3$ under the action of traction $\mathbf{t}$ bringing it in contact with electrodes $C_v \subset \mathbb{R}^3$ and $C_q \subset \mathbb{R}^3$. The electrode C_v has a fixed potential $\hat{\phi}$ while the electrode C_q has a fixed charge Q. The deformation gradient is $\mathbf{F} = \nabla_x \mathbf{y} : \Omega \to \mathbb{M}^{3\times3}$ where $\mathbb{M}^{a\times b}$ is the space of all $a \times b$ matrices and ∇_x denotes derivative with respect to the reference variable $\mathbf{x}$. Further, $\mathbf{F}$ is assumed invertible and it is assumed that $J = \det \mathbf{F} > 0$

a.e in Ω. The polarization of the ferroelectric material per unit volume is given by $\mathbf{p} : \mathbf{y}(\Omega) \to \mathbb{R}^3$ in deformed configuration. Since the deformation is assumed invertible, we can define polarization in reference configuration by $\mathbf{p}_0 : \Omega \to \mathbb{R}^3$. The two quantities are related as

$$\mathbf{p}_0(\mathbf{x}) = J\,\mathbf{p}(\mathbf{y}(\mathbf{x})). \tag{4.1}$$

Further, it is assumed that the conductor C_q is fixed in space while C_v deforms with negligible elastic energy. In practice this assumption works because the electrodes are usually very thin compared to the ferroelectric medium. A phase boundary denoted by S_0 in reference configuration (S in deformed configuration) propagates in the ferroelectric with a normal velocity s_n^0 (s_n in deformed configuration). The deformation is continuous across the phase boundary, but the deformation gradient and the polarization may suffer jumps across it. Further, the phase boundary may be charged with a charge density σ, and also experiences a force $\mathbf{f}$ per unit deformed area.

Electric field and Maxwell's equations

We define the electric potential at any point by $\phi : \mathbf{y}(\Omega) \to \mathbb{R}^3$. Using Maxwell's equations, we can relate the polarization vector and the electric field.

$$\begin{aligned} &\nabla_y \cdot (-\varepsilon_0 \nabla_y \phi + \mathbf{p}\,\chi(\mathbf{y}(\Omega, t)) = 0 \qquad \text{in } \mathbb{R}^3 \backslash (C_v \cap C_q), \\ &\nabla_y \phi = 0 \qquad \text{on } C_v \cup C_q \end{aligned} \tag{4.2}$$

subject to

$$\begin{aligned} &\int_{\partial C_q} \frac{\partial \phi}{\partial \hat{\mathbf{n}}}\, dS_y = -\frac{Q}{\varepsilon_0}, \\ &\phi = \hat{\phi} \qquad \text{on } C_v, \\ &\phi \to 0 \text{ as } |\mathbf{y}| \to \infty, \end{aligned} \tag{4.3}$$

where $\chi(B)$ is the standard characteristic function of a set B, $\hat{\mathbf{n}}$ denotes the normal to the surface C_q and ε_0 is the vacuum permittivity. Note that the Maxwell equations used above correspond to an electrostatic system, ignoring any dynamics. This is a consequence of the quasistatic electromagnetic assumption that removes any electromagnetic waves from the analysis. Following [73], we reformulate the above

system in a weaker form. $\phi \in H^1(\mathbb{R}^3)$ satisfies

$$-\int_{\mathbb{R}^3} (-\varepsilon_0 \nabla_y \phi + \mathbf{p}\, \chi(\mathbf{y}(\Omega)) \cdot \nabla_y \psi \, dy = \int_{\partial C_v \cup \partial C_q} \sigma\psi \, dS_y + \int_S \sigma\psi \, dS_y, \tag{4.4}$$

$$\int_{\partial C_q} \sigma \, dS_y = Q, \tag{4.5}$$

$$\phi = \hat{\phi} \text{ on } C_v, \tag{4.6}$$

for every $\psi \in H^1(\mathbb{R}^3)$, where $\sigma : \partial C_v \cup \partial C_q \cup S \to \mathbb{R}$ is the surface charge density on the interface defined as

$$\sigma = [\![-\varepsilon_0 \nabla_y \phi + \mathbf{p}\, \chi(\mathbf{y}(\Omega))]\!] \cdot \hat{\mathbf{n}}. \tag{4.7}$$

Comparing with the analysis in [84], notice that there is an additional term in (4.4). This is the contribution from the surface charges forming on the phase boundary S.

We can similarly derive a weak form of the Maxwell equations for an arbitrary sub-domain $\mathbf{y}(B)$, with $B \subset \Omega$, for every function $\psi \in H^1$ as follows:

$$\begin{aligned} 0 &= \int_{y(B)} \psi \ \nabla_{\mathbf{y}} \cdot (-\varepsilon_0 \nabla_{\mathbf{y}} \phi + \mathbf{p}) \, dy \\ &= \int_{y(B)} \left[\nabla_{\mathbf{y}} \cdot \left(\psi(-\varepsilon_0 \nabla_{\mathbf{y}} \phi + \mathbf{p}) \right) - \nabla_{\mathbf{y}} \psi \cdot (\varepsilon_0 \nabla_{\mathbf{y}} \phi + \mathbf{p}) \right] \, dy \\ &= \int_{\partial y(B)} \psi(-\varepsilon_0 \nabla_{\mathbf{y}} \phi + \mathbf{p}) \cdot \hat{\mathbf{n}} \, dS_y - \int_{S \cap y(B)} [\![\psi(-\varepsilon_0 \nabla_{\mathbf{y}} \phi + \mathbf{p})]\!] \cdot \hat{\mathbf{n}} \, dS_y \\ &\qquad - \int_{y(B)} \nabla_{\mathbf{y}} \psi \cdot (-\varepsilon_0 \nabla_{\mathbf{y}} \phi + \mathbf{p}) \ dy. \end{aligned} \tag{4.8}$$

Electrostatic jump conditions

The potential ϕ is continuous in $\mathbb{R}^3$, but the derivatives can be discontinuous. If an interface separates $B \subset \mathbf{y}(\Omega)$ into B^- and B^+, then across any such interface the jump in electric displacement, $\mathbf{D} = -\varepsilon_0 \nabla_y \phi + \mathbf{p}$, is given by

$$[\![\mathbf{D}]\!] \cdot \hat{\mathbf{n}} = [\![-\varepsilon_0 \nabla_y \phi + \mathbf{p}]\!] \cdot \hat{\mathbf{n}} = \sigma \tag{4.9}$$

where σ is the surface charge density on the interface and $\hat{\mathbf{n}}$ is the normal of the interface pointing from B^- to B^+. Here we use the notation $[\![a]\!] = a^+ - a^-$ for defining a jump in a across the interface. Continuity of ϕ across the interface gives $[\![\nabla_y \phi]\!] \cdot \hat{\mathbf{t}} = 0 \ \forall \ \hat{\mathbf{t}} \cdot \hat{\mathbf{n}} = 0$. From (4.9), we can get

$$[\![\nabla_y \phi]\!] = -\frac{1}{\varepsilon_0} \left(\sigma - [\![\mathbf{p} \cdot \hat{\mathbf{n}}]\!] \right) \hat{\mathbf{n}}. \tag{4.10}$$

Across any interface, the continuity equation for ϕ reduces to

$$[\![\phi_{,t}]\!] + s_n[\![\nabla_y \phi \cdot \hat{\mathbf{n}}]\!] = 0, \tag{4.11}$$

where s_n is the interface speed in the deformed configuration. In the case where the interface is not moving in the reference configuration, the continuity of ϕ simplifies to

$$[\![\phi_{,t}]\!] + [\![\nabla_y \phi]\!] \cdot \mathbf{v} = 0. \tag{4.12}$$

For future use, the *Maxwell stress tensor* $\mathbf{T}_M$ is defined in terms of electric field $\mathbf{E} = -\nabla_y \phi$ and electric displacement $\mathbf{D}$ as

$$\mathbf{T}_M = \mathbf{E} \otimes \mathbf{D} - \frac{\varepsilon_0}{2}\mathbf{E} \cdot \mathbf{E}\mathbf{I}. \tag{4.13}$$

Across an interface, $\mathbf{T}_M$ can develop discontinuities due to jumps in $\mathbf{E}$ and $\mathbf{D}$. We have,

$$\begin{aligned}
[\![\mathbf{T}_M \hat{\mathbf{n}}]\!] &= [\![(\mathbf{E} \otimes \mathbf{D} - \frac{\varepsilon_0}{2}\mathbf{E} \cdot \mathbf{E}\mathbf{I})\hat{\mathbf{n}}]\!] \\
&= \langle \mathbf{E} \rangle [\![\mathbf{D} \cdot \hat{\mathbf{n}}]\!] + [\![\mathbf{E}]\!](\langle \mathbf{D} \rangle \cdot \hat{\mathbf{n}}) - \varepsilon_0(\langle \mathbf{E} \rangle \cdot [\![\mathbf{E}]\!])\hat{\mathbf{n}} \\
&= \langle \mathbf{E} \rangle \sigma + [\![\mathbf{E}]\!](\langle \mathbf{p} \rangle \cdot \hat{\mathbf{n}} + \varepsilon_0 \langle \mathbf{E} \rangle \cdot \hat{\mathbf{n}}) - \varepsilon_0(\langle \mathbf{E} \rangle \cdot [\![\mathbf{E}]\!])\hat{\mathbf{n}} \\
&= \left(\mathbf{E}^- + \frac{[\![\mathbf{E}]\!]}{2}\right)\sigma + \varepsilon_0 [\![\mathbf{E}]\!](\langle \mathbf{E} \rangle \cdot \hat{\mathbf{n}}) + [\![\mathbf{E}]\!](\langle \mathbf{p} \cdot \hat{\mathbf{n}} \rangle) \\
&\qquad\qquad - \varepsilon_0(\langle \mathbf{E} \rangle \cdot ([\![\mathbf{E}]\!] \cdot \hat{\mathbf{n}})\hat{\mathbf{n}})\hat{\mathbf{n}} \\
&= \mathbf{E}^- \sigma + \frac{1}{\varepsilon_0}\left(\frac{\sigma}{2} + \langle \mathbf{p} \cdot \hat{\mathbf{n}} \rangle\right)(\sigma - [\![\mathbf{p} \cdot \hat{\mathbf{n}}]\!])\hat{\mathbf{n}}.
\end{aligned} \tag{4.14}$$

Here, we have used the identity $[\![ab]\!] = [\![a]\!]\langle b \rangle + \langle a \rangle [\![b]\!]$ in the second step, (4.9) in the third step and (4.10) in the fourth step.

Conservation of linear momentum

In the deformed configuration, on an arbitrary subdomain with no discontinuity, conservation of linear momentum can be writtern as

$$\frac{d}{dt}\int_{y(B)} \rho \dot{\mathbf{y}}\, dy = \int_{\partial y(B)} \mathbf{t}\, dS_y, \tag{4.15}$$

where $\mathbf{t} = \mathbb{S}\hat{\mathbf{n}}$ for some stress tensor to ensure conservation of angular momentum. The conservation of momentum in reference configuration can be written as

$$\frac{d}{dt}\int_{B} \rho_0 \dot{\mathbf{y}}\, dx = \int_{\partial B} \mathbf{t}_0\, dS_x, \tag{4.16}$$

where $\mathbf{t}_0 = \mathbb{S}_0\hat{\mathbf{n}}_0$ and the pullback $\mathbb{S}_0$ is the pullback of $\mathbb{S}$ defined as $\mathbb{S}_0 = J\mathbb{S}\mathbf{F}^{-T}$. Localizing (4.16) by applying the divergence theorem gives

$$\rho_0\ddot{\mathbf{y}} = \nabla_x \cdot \mathbb{S}_0 \tag{4.17}$$

in the reference frame and $\rho_0\ddot{\mathbf{y}} = \nabla_y \cdot \mathbb{S}$ in the deformed frame. In case of a subdomain containing a part of the phase boundary, the integral form of conservation of linear momentum in the deformed configuration can be written as

$$\frac{d}{dt}\int_{y(B)} \rho\dot{\mathbf{y}}\, dy = \int_{\partial y(B)} \mathbf{t}\, dS_y + \int_{S\cap y(B)} \mathbf{f}\, dS_y, \tag{4.18}$$

where $\mathbf{f}$ is the additional force introduced in the system to take care of any unaccounted forces due to surface charges. In the reference frame, the conservation of linear momentum can be written as

$$\frac{d}{dt}\int_{B} \rho_0\dot{\mathbf{y}}\, dy = \int_{\partial B} \mathbf{t}_0\, dS_y + \int_{S_0\cap B} \mathbf{f}_0\, dS_x, \tag{4.19}$$

where $\mathbf{f}_0$ is the pullback of $\mathbf{f}$ to the reference frame defined as follows:

$$\begin{aligned}
\hat{\mathbf{n}}\, dS_y &= J\mathbf{F}^{-T}\hat{\mathbf{n}}_0\, dS_x \\
dS_y &= \left(\hat{\mathbf{n}} \cdot J\mathbf{F}^{-T}\hat{\mathbf{n}}_0\right) dS_x \\
\int_{S\cap y(B)} \mathbf{f}\, dS_y &= \int_{S_0\cap B} \mathbf{f}\left(\hat{\mathbf{n}} \cdot J\mathbf{F}^{-T}\hat{\mathbf{n}}_0\right) dS_x = \int_{S_0\cap B} \mathbf{f}_0\, dS_x \\
\Rightarrow \qquad \mathbf{f}_0 &= \left(\hat{\mathbf{n}} \cdot J\mathbf{F}^{-T}\hat{\mathbf{n}}_0\right)\mathbf{f}.
\end{aligned} \tag{4.20}$$

Localization of (4.19) leads to the following equations,

$$\rho_0\ddot{\mathbf{y}} = \nabla_x \cdot \mathbb{S}_0 \tag{4.21}$$

$$,[\![\rho_0\dot{\mathbf{y}}]\!]s_n^0 + [\![\mathbb{S}_0\hat{\mathbf{n}}_0]\!] = \mathbf{f}_0, \tag{4.22}$$

where s_n^0 is the normal speed of the phase boundary in the reference frame.

Conservation of energy

For any subdomain $\mathbf{y}(B) \subset \mathbf{y}(\Omega)$, the conservation of energy in its rate form can be written as

$$\frac{d\mathcal{E}}{dt} = \mathcal{F} + \frac{dQ}{dt}, \tag{4.23}$$

where $\mathcal{E}$ is the total energy of the subdomain, $\mathcal{F}$ is the rate of work done and $\frac{dQ}{dt}$ is the rate of heat input to the subdomain. The total energy $\mathcal{E}$ of $\mathbf{y}(B)$ comprises of four parts: energy stored within the ferroelectric medium, interfacial energy at

the phase boundary surface due to surface charges, the energy from the electrostatic field generated by various internal and external sources and the kinetic energy of the system (see [73] for static case):

$$\mathcal{E} = \int_B E_0 dx + \int_{S\cap y(B)} W_\sigma dS_y + \frac{\varepsilon_0}{2}\int_{y(B)} |\nabla_y \phi|^2 dy + \int_B \frac{\rho_0}{2}|\dot{\mathbf{y}}|^2 dx. \tag{4.24}$$

Here, E_0 is the stored energy density in the ferroelectric medium per unit reference volume. W_σ is the interfacial energy density per unit deformed area of the phase boundary surface. In this analysis, we will be dealing with sharp interfaces due to shocks. The second term in (4.24) is the energy associated with the electric field in $\mathbf{y}(B)$. The electric potential ϕ can be obtained by solving the Maxwell equations (4.2) subject to boundary conditions (4.3).

The rate of work done $\mathcal{F}$ on $\mathbf{y}(B)$ is given by a combination of rate of work done by external traction and the rate of work done by external fields on the boundary of the subdomain. This can be written as

$$\mathcal{F} = \int_{\partial y(B)} \mathbf{t}\cdot\mathbf{v}\, dS_y - \int_{\partial y(B)} \phi \frac{d}{dt}\left(\mathbf{D}\cdot\hat{\mathbf{n}}\right)\, dS_y - \int_{\partial y(B)} \phi\left(\mathbf{D}\cdot\hat{\mathbf{n}}\right)\left(\mathbf{v}\cdot\hat{\mathbf{n}}\right) dS_y, \tag{4.25}$$

where $\mathbf{D} = \mathbf{p} - \varepsilon_0 \nabla_y \phi$ is used for compactness of notation. The second and third terms in (4.25) correspond to electrostatic work done and additional electrical work due to convection, respectively. Finally the rate of heat input is given by a combination of volumetric heat generation and heat flux going out through the boundary:

$$\begin{aligned}\frac{dQ}{dt} &= \int_B \dot{r}\, dx - \int_{\partial y(B)} \mathbf{q}\cdot\hat{\mathbf{n}}\, dS_y \\ &= \int_B \dot{r}\, dx - \int_B \nabla_x \cdot J\mathbf{F}^{-1}\mathbf{q}\, dx + \int_{S_0\cap B} [\![J\mathbf{F}^{-1}\mathbf{q}\cdot\hat{\mathbf{n}}_0]\!]\, dS_x.\end{aligned} \tag{4.26}$$

Rate of change of total energy

We are interested in calculating the rate of change of total energy,

$$\begin{aligned}\frac{d\mathcal{E}}{dt} =& \frac{d}{dt}\int_B E_0 dx + \frac{d}{dt}\int_{S\cap y(B)} W_\sigma(\sigma) dS_y + \frac{d}{dt}\int_{y(B)} \frac{\varepsilon_0}{2}|\nabla_y\phi|^2 dy \\ &+ \frac{d}{dt}\int_B \frac{\rho_0}{2}|\dot{\mathbf{y}}|^2 dx.\end{aligned} \tag{4.27}$$

Rate of change of stored energy

Looking at the first term in (4.27),

$$\begin{aligned}\frac{d}{dt}\int_B E_0 dx &= \frac{d}{dt}\left[\int_{B^+} E_0 dx + \int_{B^-} E_0 dx\right] \\ &= \int_B \dot{E}_0 dx - \int_{S_0\cap B} [\![E_0]\!] s_n^0 dS_x. \end{aligned} \tag{4.28}$$

The calculation of the rate of electrostatic energy in (4.27) is rather involved. The steps are similar to [40] and [84] but with modifications and generalizations. The calculation is split over four parts listed below.

Rate of change of electrostatic energy: Part 1

We start by the weak form of Maxwell equation (4.8) and set $\psi = \phi$. Since ψ is assumed continuous throughout, we can take out the jump term from (4.8). We use $\mathbf{D} = -\varepsilon_0 \nabla_{\mathbf{y}}\phi + \mathbf{p}$ for notation, whenever needed. Re-arranging the terms, we get

$$\int_{y(B)} \varepsilon_0 \nabla_y \phi \cdot \nabla_y \phi dy = \int_y \nabla_y \phi \cdot \mathbf{p} dy + \int_{S\cap y(B)} \phi\sigma dS_y - \int_{\partial y(B)} \phi(\mathbf{D}\cdot\hat{\mathbf{n}})\, dS_y. \tag{4.29}$$

Differentiating with time, we get

$$\begin{aligned}\frac{d}{dt}\int_{y(B)} \varepsilon_0 \nabla_y\phi \cdot \nabla_y\phi\, dy \;&= \frac{d}{dt}\int_{y(B)} \nabla_y\phi\cdot\mathbf{p} dy + \frac{d}{dt}\int_{S\cap y(B)} \phi\sigma dS_y \\ &\quad - \frac{d}{dt}\int_{\partial y(B)} \phi(\mathbf{D}\cdot\hat{\mathbf{n}})\, dS_y.\end{aligned}$$

On the phase boundary $S \cap y(B)$, the time derivative is more involved (see [17]):

$$\frac{d}{dt}\int_S \phi\sigma\, dy = \int_S \left(\overset{\circ}{\overline{(\phi\sigma)}} - \phi\sigma s_n \kappa\right) dS_y + \int_{\partial S} \phi\sigma(\mathbf{v}\cdot\mathbf{w})\, dl,$$

where κ is the total curvature of S and $\mathbf{w}$ is the unit vector on the boundary of S, tangential to the surface but normal to the curve $\partial S \cap y(B)$. For simplicity, we ignore the term corresponding to ∂S. In other words, we are neglecting the line charge on the boundary $\partial(S \cap y(B))$. Also, $\mathring{a}$ denotes the normal time derivative of a on the surface S. This simplifies to

$$\frac{d}{dt}\int_S \phi\sigma\, dS_y = \int_S \mathring{\phi}\sigma\, dS_y + \int_S \phi\mathring{\sigma}\, dS_y - \int_S \phi\sigma s_n\kappa\, dS_y. \tag{4.30}$$

Finally, the time derivative of (4.29) can be written as

$$
\begin{aligned}
&\frac{d}{dt}\left[\int_{y(B)} \varepsilon_0 |\nabla\phi|^2 dy\right] \\
&= \frac{d}{dt}\int_{y(B)} \nabla_y\phi\cdot\mathbf{p}\; dy + \int_{S\cap y(B)} (\mathring{\phi}\sigma + \phi\mathring{\sigma} - \phi\sigma s_n\kappa)\, dS_y - \frac{d}{dt}\int_{\partial y(B)} \phi\mathbf{D}\cdot\hat{\mathbf{n}}\, dS_y \\
&= \frac{d}{dt}\int_{B} \nabla_y\phi\cdot\mathbf{p}_0\; dx + \int_{S\cap y(B)} (\mathring{\phi}\sigma + \phi\mathring{\sigma} - \phi\sigma s_n\kappa)\, dS_y - \frac{d}{dt}\int_{\partial y(B)} \phi\mathbf{D}\cdot\hat{\mathbf{n}}\, dS_y \\
&= \int_B \left(\frac{d}{dt}(\nabla_y\phi)\cdot\mathbf{p}_0 + \nabla_y\phi\cdot\dot{\mathbf{p}}_0\right) dx - \int_{S_0\cap B} [\![(\nabla_y\phi)\cdot\mathbf{p}_0]\!] s_n^0\, dS_x \\
&\qquad + \int_{S\cap y(B)} (\mathring{\phi}\sigma + \phi\mathring{\sigma} - \phi\sigma s_n\kappa)\, dS_y - \frac{d}{dt}\int_{\partial y(B)} \phi\mathbf{D}\cdot\hat{\mathbf{n}}\, dS_y \\
&= \int_B (\nabla_y\phi + \mathbf{v}(\nabla_y\nabla_y\phi))\cdot\mathbf{p}_0\; dx + \int_B \nabla_y\phi\cdot\dot{\mathbf{p}}_0\; dx - \int_{S_0\cap B} [\![(\nabla_y\phi)\cdot\mathbf{p}_0]\!] s_n^0\, dS_x \\
&\qquad\qquad + \int_{S\cap y(B)} (\mathring{\phi}\sigma + \phi\mathring{\sigma} - \phi\sigma s_n\kappa)\, dS_y - \frac{d}{dt}\int_{\partial y(B)} \phi\mathbf{D}\cdot\hat{\mathbf{n}}\, dS_y.
\end{aligned}
\tag{4.31}
$$

Rate of change of electrostatic energy: Part 2

Next, we put $\psi = \phi_{,t}$ in the weak form of Maxwell equation (4.8). This time, since $\phi_{,t}$ can be discontinuous across the phase boundary, we can not take it out of the jump term:

$$
\int_{y(B)} \varepsilon_0 \nabla_{\mathbf{y}}\phi\cdot\nabla_{\mathbf{y}}\phi_{,t}\, dy = \int_B \nabla_{\mathbf{y}}\phi_{,t}\cdot\mathbf{p}_0\, dx - \int_{\partial y(B)} \phi_{,t}\mathbf{D}\cdot\hat{\mathbf{n}}\, dS_y + \int_{S\cap y(B)} [\![\phi_{,t}\,\mathbf{D}\cdot\hat{\mathbf{n}}]\!]\, dS_y. \tag{4.32}
$$

Rate of change of electrostatic energy: Part 3

We use the Reynolds' transport theorem to get

$$
\begin{aligned}
&\frac{d}{dt}\left[\int_{y(B)} \frac{\varepsilon_0}{2}|\nabla_{\mathbf{y}}\phi|^2 dy\right] \\
&= \int_{y(B)} \frac{\partial}{\partial t}\left(\frac{\varepsilon_0}{2}|\nabla_{\mathbf{y}}\phi|^2\right) dy + \int_{\partial y(B)} \frac{\varepsilon_0}{2}|\nabla_{\mathbf{y}}\phi|^2\mathbf{v}\cdot\hat{\mathbf{n}}\, dS_y \\
&\qquad\qquad - \int_{S\cap y(B)} \left[\!\!\left[\frac{\varepsilon_0}{2}|\nabla_{\mathbf{y}}\phi|^2\right]\!\!\right] s_n\, dS_y \\
&= \int_{y(B)} \varepsilon_0 \nabla_{\mathbf{y}}\phi\cdot\nabla_{\mathbf{y}}\phi_{,t}\, dy + \int_{\partial y(B)} \frac{\varepsilon_0}{2}|\nabla_{\mathbf{y}}\phi|^2\mathbf{v}\cdot\hat{\mathbf{n}}\, dS_y - \int_{S\cap y(B)} \left[\!\!\left[\frac{\varepsilon_0}{2}|\nabla_{\mathbf{y}}\phi|^2\right]\!\!\right] s_n\, dS_y.
\end{aligned}
\tag{4.33}
$$

Plugging (4.32) in (4.33) gives us

$$\frac{d}{dt}\left[\frac{1}{2}\int_{y(B)}\varepsilon_0|\nabla_y\phi|^2dy\right] = \int_B \nabla_{\mathbf{y}}\phi_{,t}\cdot\mathbf{p}_0\,dx - \int_{\partial y(B)}\phi_{,t}(-\varepsilon_0\nabla_{\mathbf{y}}\phi+\mathbf{p})\cdot\hat{\mathbf{n}}\,dS_y + \int_{S\cap y(B)}[\![\phi_{,t}\,\mathbf{D}\cdot\hat{\mathbf{n}}]\!]\,dS_y + \int_{\partial y(B)}\frac{\varepsilon_0}{2}|\nabla_{\mathbf{y}}\phi|^2\mathbf{v}\cdot\hat{\mathbf{n}}\,dS_y - \int_{S\cap y(B)}\left[\!\!\left[\frac{\varepsilon_0}{2}|\nabla_{\mathbf{y}}\phi|^2\right]\!\!\right]s_n\,dS_y. \tag{4.34}$$

We simplify the terms in (4.34) associated with $S\cap y(B)$ by using the continuity equation (4.11) across $S\cap y(B)$. Across the surface $S\cap y(B)$, $[\![\nabla_y\phi]\!] = -\frac{1}{\varepsilon_0}(\sigma - [\![\mathbf{p}\cdot\hat{\mathbf{n}}]\!])\hat{\mathbf{n}}$ and $[\![\phi_{,t}]\!] = \frac{1}{\varepsilon_0}(\sigma - [\![\mathbf{p}\cdot\hat{\mathbf{n}}]\!])s_n$:

$$\begin{aligned}
&\int_{S\cap y(B)}[\![\phi_{,t}(-\varepsilon\nabla_y\phi+\mathbf{p})]\!]\cdot\hat{\mathbf{n}}\,dS_y - \int_{S\cap y(B)}\left[\!\!\left[\frac{\varepsilon_0}{2}|\nabla_y\phi|^2\right]\!\!\right]s_n\,dS_y\\
&\quad= \int_{S\cap y(B)}\langle\phi_{,t}\rangle[\![\mathbf{D}]\!]\cdot\hat{\mathbf{n}}\,dS_y + \int_{S\cap y(B)}[\![\phi_{,t}]\!]\langle\mathbf{D}\rangle\cdot\hat{\mathbf{n}}\,dS_y - \int_{S\cap y(B)}\varepsilon_0(\langle\nabla_y\phi\rangle\cdot[\![\nabla_y\phi]\!])s_n\,dS_y\\
&\quad= \int_{S\cap y(B)}\langle\phi_{,t}\rangle\sigma\,dS_y + \int_{S\cap y(B)}[\![\phi_{,t}]\!]\langle-\varepsilon_0\nabla_y\phi+\mathbf{p}\rangle\cdot\hat{\mathbf{n}}\,dS_y - \int_{S\cap y(B)}\varepsilon_0(\langle\nabla_y\phi\rangle\cdot[\![\nabla_y\phi]\!])s_n\,dS_y.
\end{aligned}$$

Across $S\cap y(B)$, $\langle\phi_{,t}\rangle = \mathring{\phi} - \langle\nabla_y\phi\cdot\hat{\mathbf{n}}\rangle s_n$. Putting this and the jump terms into the

above equation, we obtain

$$
\begin{aligned}
&= \int_{S\cap y(B)} (\mathring{\phi} - \langle \nabla_y \phi \cdot \hat{\mathbf{n}} \rangle s_n)\sigma \, dS_y + \int_{S\cap y(B)} \frac{1}{\varepsilon_0} \left(\sigma - [\![\mathbf{p} \cdot \hat{\mathbf{n}}]\!]\right) s_n \langle \mathbf{D} \rangle \cdot \hat{\mathbf{n}} \, dS_y \\
&\qquad + \int_{S\cap y(B)} \varepsilon_0 \left(\langle \nabla_y \phi \rangle \cdot \frac{1}{\varepsilon_0} \left(\sigma - [\![\mathbf{p} \cdot \hat{\mathbf{n}}]\!]\right) \hat{\mathbf{n}} \right) s_n \, dS_y \\
&= \int_{S\cap y(B)} (\mathring{\phi} - \langle \nabla_y \phi \cdot \hat{\mathbf{n}} \rangle s_n)\sigma \, dS_y + \int_{S\cap y(B)} \frac{1}{\varepsilon_0} \left(\sigma - [\![\mathbf{p} \cdot \hat{\mathbf{n}}]\!]\right) s_n \langle \mathbf{D} \rangle \cdot \hat{\mathbf{n}} \, dS_y \\
&\qquad + \int_{S\cap y(B)} \langle \nabla_y \phi \cdot \hat{\mathbf{n}} \rangle \left(\sigma - [\![\mathbf{p} \cdot \hat{\mathbf{n}}]\!]\right) s_n \, dS_y \\
&= \int_{S\cap y(B)} (\mathring{\phi} - \langle \nabla_y \phi \cdot \hat{\mathbf{n}} \rangle s_n)\sigma \, dS_y + \int_{S\cap y(B)} \frac{1}{\varepsilon_0} \left(\sigma - [\![\mathbf{p} \cdot \hat{\mathbf{n}}]\!]\right) s_n \langle \mathbf{p} \cdot \hat{\mathbf{n}} \rangle \, dS_y \\
&= \int_{S\cap y(B)} (\mathring{\phi} - \left(\nabla_y \phi^- + \frac{1}{2} [\![\nabla_y \phi]\!] \right) \cdot \hat{\mathbf{n}} \, s_n)\sigma \, dS_y \\
&\qquad + \int_{S\cap y(B)} \frac{1}{\varepsilon_0} \left(\sigma - [\![\mathbf{p} \cdot \hat{\mathbf{n}}]\!]\right) s_n \langle \mathbf{p} \cdot \hat{\mathbf{n}} \rangle \, dS_y \\
&= \int_{S\cap y(B)} \left[s_n \sigma \left(-\nabla_y \phi^- \cdot \hat{\mathbf{n}} \right) + \frac{s_n}{\varepsilon_0} \left(\sigma - [\![\mathbf{p} \cdot \hat{\mathbf{n}}]\!]\right) \left(\frac{\sigma}{2} + \langle \mathbf{p} \cdot \hat{\mathbf{n}} \rangle \right) \right] dS_y \\
&\qquad + \int_{S\cap y(B)} \mathring{\phi} \sigma \, dS_y.
\end{aligned}
$$

Using (4.14), this analysis gives us

$$
\begin{aligned}
&\int_{S\cap y(B)} \left[[\![\phi_{,t} (\mathbf{D} \cdot \hat{\mathbf{n}})]\!] - \left[\!\!\left[\frac{\varepsilon_0}{2} |\nabla_y \phi|^2 \right]\!\!\right] s_n \right] \, dS_y \\
&\qquad = \int_{S\cap y(B)} \mathring{\phi} \sigma \, dS_y + \int_{S\cap y(B)} [\![\hat{\mathbf{n}} \cdot \mathbf{T}_M \hat{\mathbf{n}}]\!] s_n \, dS_y, \qquad (4.35)
\end{aligned}
$$

where $[\![\hat{\mathbf{n}} \cdot \mathbf{T}_M \hat{\mathbf{n}}]\!] = \sigma(-\nabla_y \phi^- \cdot \hat{\mathbf{n}}) + \frac{1}{\varepsilon_0}(\frac{\sigma}{2} + \langle \mathbf{p} \cdot \hat{\mathbf{n}} \rangle)(\sigma - [\![\mathbf{p} \cdot \hat{\mathbf{n}}]\!])$. Next, we deal with the $\partial y(B)$ terms in (4.34). We write $\phi_{,t} = \dot{\phi} - \nabla_y \phi \cdot \mathbf{v}$, and use the definition of Maxwell stress (4.13) such that,

$$
\int_{\partial y(B)} \phi_{,t} (\mathbf{D} \cdot \hat{\mathbf{n}}) - \frac{\varepsilon_0}{2} |\nabla_{\mathbf{y}} \phi|^2 \mathbf{v} \cdot \hat{\mathbf{n}} \, dS_y = \int_{\partial y(B)} \frac{d\phi}{dt} \mathbf{D} \cdot \hat{\mathbf{n}} \, dS_y + \int_{\partial y(B)} \mathbf{T}_M \hat{\mathbf{n}} \cdot \mathbf{v} \, dS_y. \qquad (4.36)
$$

Plugging (4.35) and (4.36) in (4.34), we get

$$
\begin{aligned}
\frac{d}{dt} \left[\frac{1}{2} \int_{y(B)} \varepsilon_0 |\nabla_y \phi|^2 dy \right] &= \int_B \nabla_{\mathbf{y}} \phi_{,t} \cdot \mathbf{p}_0 \, dx - \int_{\partial y(B)} \frac{d\phi}{dt} \mathbf{D} \cdot \hat{\mathbf{n}} \, dS_y \\
&\quad + \int_{S\cap y(B)} \mathring{\phi} \sigma \, dS_y - \int_{\partial y(B)} \mathbf{T}_M \hat{\mathbf{n}} \cdot \mathbf{v} \, dS_y \\
&\quad + \int_{S\cap y(B)} [\![\hat{\mathbf{n}} \cdot \mathbf{T}_M \hat{\mathbf{n}}]\!] s_n \, dS_y. \qquad (4.37)
\end{aligned}
$$

Rate of change of electrostatic energy: Part 4

Finally we subtract (4.37) from (4.31) to get the final expression:

$$\begin{aligned}\frac{d}{dt}\int_{y(B)}\frac{\varepsilon_0}{2}|\nabla_y\phi|^2\,dy = &\int_{y(B)}(\nabla_y\nabla_y\phi)\mathbf{v}\cdot\mathbf{p}\,dy + \int_B \nabla_y\phi\cdot\dot{\mathbf{p}}_0\,dx\\ &-\int_{S_0\cap B}[\![\nabla_y\phi\cdot\mathbf{p}]\!]s_n^0\,dS_x + \int_{\partial y(B)}\mathbf{T}_M\hat{\mathbf{n}}\cdot\mathbf{v}\,dS_y\\ &+\int_{\partial y(B)}\frac{d\phi}{dt}\mathbf{D}\cdot\hat{\mathbf{n}}\,dS_y - \frac{d}{dt}\int_{\partial y(B)}\phi\,\mathbf{D}\cdot\hat{\mathbf{n}}\,dS_y\\ &-\int_{S\cap y(B)}[\![\hat{\mathbf{n}}\cdot\mathbf{T}_M\hat{\mathbf{n}}]\!]s_n\,dS_y + \int_{S\cap y(B)}(\phi\mathring{\sigma} - \kappa\sigma\phi s_n)\,dS_y.\end{aligned} \tag{4.38}$$

Rate of change of kinetic energy

Using the typical Reynolds' transport theorem, we obtain

$$\begin{aligned}\frac{d}{dt}\int_B\frac{\rho_0}{2}|\dot{\mathbf{y}}|^2dx &= \int_B\rho_0\ddot{\mathbf{y}}\cdot\dot{\mathbf{y}}\,dx - \int_{S_0\cap B}\left[\!\!\left[\frac{\rho_0}{2}\dot{\mathbf{y}}\cdot\dot{\mathbf{y}}\right]\!\!\right]s_n^0\,dS_x\\ &= \int_{y(B)}\rho\ddot{\mathbf{y}}\cdot\dot{\mathbf{y}}\,dy - \int_{S_0\cap B}\left[\!\!\left[\frac{\rho_0}{2}\dot{\mathbf{y}}\cdot\dot{\mathbf{y}}\right]\!\!\right]s_n^0\,dS_x.\end{aligned} \tag{4.39}$$

Rate of change of interfacial energy

The rate of change of the interfacial energy can be written as (following [17])

$$\frac{d}{dt}\int_{S\cap y(B)}W_\sigma dS_y = \int_{S\cap y(B)}(\mathring{W}_\sigma - W_\sigma s_n\kappa)dS_y. \tag{4.40}$$

Here we have ignored the line charges on $\partial(S\cap y(B))$ so that we do not have to deal with the contribution from the ∂S curve.

First law of thermodynamics

Finally putting all the expressions together, (4.23) becomes

$$\begin{aligned}&\int_B\left[\dot{E}_0 + \nabla_y\phi\cdot\dot{\mathbf{p}}_0 - \dot{r} + \nabla_x\cdot J\mathbf{F}^{-1}\mathbf{q}\right]\,dx + \int_{y(B)}\left[\left(\nabla_y\nabla_y\phi\right)\mathbf{v}\cdot\mathbf{p} + \rho\ddot{\mathbf{y}}\cdot\mathbf{v}\right]\,dy\\ &+\int_{\partial y(B)}\left[\mathbf{T}_M\hat{\mathbf{n}}\cdot\mathbf{v} - \mathbf{t}\cdot\mathbf{v}\right]\,dS_y\\ &+\int_{S_0\cap B}\left[-[\![E_0 + \nabla_y\phi\cdot\mathbf{p}_0]\!]s_n^0 - \left[\!\!\left[\frac{\rho_0}{2}\dot{\mathbf{y}}\cdot\dot{\mathbf{y}}\right]\!\!\right]s_n^0 - [\![J\mathbf{F}^{-1}\mathbf{q}\cdot\hat{\mathbf{n}}_0]\!]\right]\,dS_x\\ &+\int_{S\cap y(B)}\left[-[\![\hat{\mathbf{n}}\cdot\mathbf{T}_M\hat{\mathbf{n}}]\!]s_n - (W_\sigma + \sigma\phi)\kappa s_n - \mathbf{f}\cdot\mathring{\mathbf{y}} + \left(\mathring{W}_\sigma + \phi\mathring{\sigma}\right)\right]\,dS_y\\ &+\int_{\partial y(B)}\left[\frac{d\phi}{dt}\mathbf{D}\cdot\hat{\mathbf{n}} + \phi\frac{d}{dt}(\mathbf{D}\cdot\hat{\mathbf{n}}) + \phi(\mathbf{D}\cdot\hat{\mathbf{n}})(\mathbf{v}\cdot\hat{\mathbf{n}})\right]\,dS_y - \frac{d}{dt}\int_{\partial y(B)}\phi\,\mathbf{D}\cdot\hat{\mathbf{n}}\,dS_y\\ &= 0.\end{aligned} \tag{4.41}$$

Next, we do a few rearragements and simplifications to some terms in (4.41). Note that, $(\nabla_y \nabla_y \phi)\mathbf{v} \cdot \mathbf{p} = (\nabla_y \nabla_y \phi)\mathbf{p} \cdot \mathbf{v}$ because $\phi_{,ij} = \phi_{,ji}$. Looking at $(\nabla_y \nabla_y \phi)\mathbf{p}$,

$$\begin{aligned}
-(\nabla_y \nabla_y \phi)\mathbf{p} &= -\phi_{,ij} p_j \\
&= -\phi_{,ij}(D_j + \varepsilon_0 \phi_{,j}) \\
&= -(\phi_{,i} D_j)_{,j} - \left(\frac{\varepsilon_0}{2}\phi_{,k}\phi_{,k}\delta_{ij}\right)_{,j} \\
&= (E_i D_j)_{,j} - \left(\frac{\varepsilon_0}{2} E_k E_k \delta_{ij}\right)_{,j} \\
&= \nabla_y \cdot \left(\mathbf{E} \otimes \mathbf{D} - \frac{\varepsilon_0}{2}\mathbf{E} \cdot \mathbf{E}\mathbf{I}\right) \\
&= \nabla_y \cdot \mathbf{T}_M, \qquad (4.42)
\end{aligned}$$

where the electrostatic Maxwell equation $\nabla_y \cdot \mathbf{D} = 0$ is used in the third step. This means that $(\nabla_y \nabla_y \phi)\mathbf{v} \cdot \mathbf{p} = -\left(\nabla_y \cdot \mathbf{T}_M\right) \cdot \mathbf{v}$. The next step is to simplify $-\int_{y(B)} \left(\nabla_y \cdot \mathbf{T}_M\right) \cdot \mathbf{v}\, dy$ as

$$\begin{aligned}
-\int_{y(B)} \left(\nabla_y \cdot \mathbf{T}_M\right) \cdot \mathbf{v}\, dy &= \int_{y(B)} \left[-\nabla_y \cdot \left(\mathbf{v}^T \mathbf{T}_M\right) + \mathbf{T}_M \cdot \nabla_y \mathbf{v}\right]\, dy \\
&= \int_{y(B)} -\left(T^M_{ij} v_i\right)_{,j} + T^M_{ij} v_{i,j}\, dy \\
&= -\int_{\partial y(B)} T^M_{ij} v_i n_j\, dS_y + \int_{S \cap y(B)} [\![T^M_{ij} v_i]\!] n_j\, dS_y \\
&\qquad + \int_{y(B)} T^M_{ij} v_{i,j}\, dy, \qquad (4.43)
\end{aligned}$$

where T^M_{ij} denotes the components of the Maxwell stress tensor $\mathbf{T}_M$. Rearranging and pulling back the last two terms to the reference configuration gives

$$\begin{aligned}
-\int_{y(B)} \left(\nabla_y \cdot \mathbf{T}_M\right) \cdot \mathbf{v}\, dy + \int_{\partial y(B)} \mathbf{T}_M \hat{\mathbf{n}} \cdot \mathbf{v}\, dS_y & \\
= \int_{S_0 \cap B} [\![J \mathbf{T}_M \mathbf{F}^{-T} \hat{\mathbf{n}}_0 \cdot \mathbf{v}]\!]\, dS_x + \int_B J \mathbf{T}_M \mathbf{F}^{-T} \cdot \dot{\mathbf{F}}\, dx & \\
= \int_{S_0 \cap B} [\![\mathbf{T}^0_M \hat{\mathbf{n}}_0 \cdot \mathbf{v}]\!]\, dS_x + \int_B \mathbf{T}^0_M \cdot \dot{\mathbf{F}}\, dx, \qquad (4.44) &
\end{aligned}$$

where $\mathbf{T}^0_M = J\mathbf{T}_M\mathbf{F}^{-T}$ is the pullback of the Maxwell stress tensor into the reference frame. Next, we focus on the traction term as follows:

$$\begin{aligned}\int_{\partial y(B)} \mathbf{t}\cdot\mathbf{v}\, dS_y &= \int_{\partial y(B)} \mathbb{S}\hat{\mathbf{n}}\cdot\mathbf{v}\, dS_y = \int_{\partial B} J\mathbb{S}\mathbf{F}^{-T}\hat{\mathbf{n}}_0\cdot\mathbf{v}\, dS_x = \int_{\partial B} \mathbb{S}_0\hat{\mathbf{n}}_0\cdot\mathbf{v}\, dS_x \\ &= \int_B \nabla_x\cdot(\mathbb{S}_0\mathbf{v})\ dx + \int_{S_0\cap B} [\![\mathbb{S}_0\hat{\mathbf{n}}_0\cdot\mathbf{v}]\!]\, dS_x \\ &= \int_B \left[(\nabla_x\cdot\mathbb{S}_0)\cdot\mathbf{v} + \mathbb{S}_0\cdot\dot{\mathbf{F}}\right]\ dx + \int_{S_0\cap B} [\![\mathbb{S}_0\hat{\mathbf{n}}_0\cdot\mathbf{v}]\!]\, dS_x. \end{aligned} \tag{4.45}$$

We use the following equality (see [40]) to manipulate the terms associated with s_n in (4.41),

$$\begin{aligned}\int_S g s_n\ dS_y &= \int_S g\ \mathbf{v}^{\pm}\cdot\hat{\mathbf{n}}\ dS_y + \int_{S_0} g\ J^{\pm}s_n^0\, dS_x\,, \\ \int_S [\![g]\!]s_n\ dS_y &= \int_S [\![g\mathbf{v}\cdot\hat{\mathbf{n}}]\!]\ dS_y + \int_{S_0} [\![g\ J]\!]s_n^0\ dS_x\,. \end{aligned}$$

Starting with the term associated with Maxwell stress and s_n in (4.41),

$$\begin{aligned}\int_{S\cap y(B)} [\![\hat{\mathbf{n}}\cdot\mathbf{T}_M\hat{\mathbf{n}}]\!]s_n\, dS_y &= \int_{S\cap y(B)} [\![\mathbf{v}\cdot\mathbf{T}_M\hat{\mathbf{n}}]\!]\, dS_y + \int_{S_0\cap B} [\![(\hat{\mathbf{n}}\cdot\mathbf{T}_M\hat{\mathbf{n}})J]\!]s_n^0\, dS_x \\ &= \int_{S\cap y(B)} [\![\mathbf{v}\cdot\mathbf{T}^0_M\hat{\mathbf{n}}_0]\!]\, dS_y + \int_{S_0\cap B} [\![(\hat{\mathbf{n}}\cdot\mathbf{T}_M\hat{\mathbf{n}})J]\!]s_n^0\, dS_x. \end{aligned} \tag{4.46}$$

Looking at κ term associated with s_n in (4.41)

$$\begin{aligned}&\int_{S\cap y(B)} (W_\sigma + \phi\sigma)\kappa s_n\, dS_y \\ &= \int_{S\cap y(B)} \mathbf{v}^{\pm}\cdot(W_\sigma+\phi\sigma)\kappa\hat{\mathbf{n}}\, dS_y + \int_{S_0\cap B} (W_\sigma+\phi\sigma)\kappa s_n^0 J^{\pm}\, dS_x \\ &= \int_{S\cap y(B)} \langle\mathbf{v}\rangle\cdot(W_\sigma+\phi\sigma)\kappa\hat{\mathbf{n}}\, dS_y + \int_{S_0\cap B} (W_\sigma+\phi\sigma)\kappa s_n^0\langle J\rangle\, dS_x. \end{aligned} \tag{4.47}$$

Finally, looking at the term corresponding to the jump in kinetic energy,

$$\begin{aligned}\int_{S_0\cap B} \left[\!\!\left[\frac{\rho_0}{2}\dot{\mathbf{y}}\cdot\dot{\mathbf{y}}\right]\!\!\right] s_n^0\, dS_x &= \int_{S_0\cap B} s_n^0 [\![\rho_0\dot{\mathbf{y}}]\!]\cdot\langle\mathbf{v}\rangle\, dS_x \\ &= \int_{S_0\cap B} (-[\![\mathbb{S}_0\hat{\mathbf{n}}_0]\!] + \mathbf{f}_0)\cdot\langle\mathbf{v}\rangle\, dS_x. \end{aligned} \tag{4.48}$$

The last two terms in (4.41) cancel out. Finally, putting (4.44), (4.45), (4.46), (4.47) and (4.48) in (4.41),

$$\begin{aligned}
&\int_B \left[\dot{E}_0 + \nabla_y\phi\cdot\dot{\mathbf{p}}_0 - \dot{r} + \nabla_x\cdot\mathbf{q}_0 - (\mathbb{S}_0 - \mathbf{T}_M^0)\cdot\dot{\mathbf{F}} + (\rho_0\ddot{\mathbf{y}} - \nabla_x\cdot\mathbb{S}_0)\cdot\mathbf{v}\right] dx \\
&+ \int_{S_0\cap B}\left(-[\![E_0 + \nabla_y\phi\cdot\dot{\mathbf{p}}_0 + (\hat{\mathbf{n}}\cdot\mathbf{T}_M\hat{\mathbf{n}})J - \langle\mathbb{S}_0\hat{\mathbf{n}}_0\rangle\cdot(\mathbf{F}\hat{\mathbf{n}}_0)]\!]\right) s_n^0\, dS_x \\
&- \int_{S_0\cap B}\left[(W_\sigma + \phi\sigma)\kappa s_n^0 - [\![\mathbf{q}_0\cdot\hat{\mathbf{n}}_0]\!]\right] dS_x \\
&+ \int_{S\cap y(B)}\left(\mathring{W}_\sigma + \phi\mathring{\sigma}\right) dS_y \\
&- \int_{S\cap y(B)}(\mathbf{f} - (W_\sigma + \phi\sigma)\kappa\hat{\mathbf{n}})\cdot\langle\mathbf{v}\rangle\, dS_y \\
&= 0, \qquad (4.49)
\end{aligned}$$

where $\mathbf{q}_0 = J\mathbf{F}^{-1}\mathbf{q}$ is introduced and $\mathbf{f}_0$ is pushed forward to the deformed configuration using (4.20). Using the conservation of momentum equation (4.21), the coefficient of $\mathbf{v}$ in the first term of (4.49) vanishes. Applying arbitrariness of domains arguments, the equation can be localized to

$$\dot{E}_0 + \nabla_y\phi\cdot\dot{\mathbf{p}}_0 - \dot{r} + \nabla_x\cdot\mathbf{q}_0 - (\mathbb{S}_0 - \mathbf{T}_M^0)\cdot\dot{\mathbf{F}} = 0\,, \qquad (4.50)$$

$$\begin{aligned}
\left(-[\![E_0 + \nabla_y\phi\cdot\dot{\mathbf{p}}_0 + (\hat{\mathbf{n}}\cdot\mathbf{T}_M\hat{\mathbf{n}})J - \langle\mathbb{S}_0\hat{\mathbf{n}}_0\rangle\cdot(\mathbf{F}\hat{\mathbf{n}}_0)]\!] - (W_\sigma + \phi\sigma)\kappa\right) s_n^0 \\
- [\![\mathbf{q}_0\cdot\hat{\mathbf{n}}_0]\!] = 0\,, \qquad (4.51)
\end{aligned}$$

$$\left(\mathring{W}_\sigma + \phi\mathring{\sigma}\right) = 0\,, \text{ and} \qquad (4.52)$$

$$(\mathbf{f} - (W_\sigma + \phi\sigma)\kappa\hat{\mathbf{n}})\cdot\langle\mathbf{v}\rangle = 0. \qquad (4.53)$$

Coleman-Noll arguments can be applied to (4.53) to give,

$$\mathbf{f} - (W_\sigma + \phi\sigma)\kappa\hat{\mathbf{n}} = 0. \qquad (4.54)$$

The force $\mathbf{f}$ is an extra self-force that appears because the phase boundary need not be straight. For a flat phase boundary with surface charge, the force acting on the phase boundary is given by $\langle\mathbf{E}\rangle\sigma$, which is accounted for in the $[\![\mathbf{T}_M]\!]$ as given by the third step of (4.14). The absence of curvature also means $\mathbf{f} = 0$.

Second law of thermodynamics

The second law of thermodynamics on the arbitrary volume can be used to get

$$\frac{d}{dt}\int_B \eta_0\, dx \geq \int_B \frac{\dot{r}}{\theta}\, dx - \int_{\partial B} \frac{\mathbf{q}_0 \cdot \hat{\mathbf{n}}_0}{\theta}\, dS_x,$$

$$\int_B \dot{\eta}_0\, dx - \int_{S_0 \cap B} [\![\eta_0]\!]\, s_n^0\, dS_x \geq \int_B \frac{\dot{r}}{\theta}\, dx - \int_B \nabla_x \cdot \left(\frac{\mathbf{q}_0}{\theta}\right) dx + \int_{S_0 \cap B} \left[\!\!\left[\frac{\mathbf{q}_0 \cdot \hat{\mathbf{n}}_0}{\theta}\right]\!\!\right] dS_x,$$

$$\int_B \left(\dot{\eta}_0 - \frac{\dot{r}}{\theta} + \nabla_x \cdot \left(\frac{\mathbf{q}_0}{\theta}\right)\right) dx + \int_{S_0 \cap B} \left(-[\![\eta_0]\!] s_n^0 - \left[\!\!\left[\frac{\mathbf{q}_0 \cdot \hat{\mathbf{n}}_0}{\theta}\right]\!\!\right]\right) dS_x \geq 0.$$

Using arbitrariness of domain argument, the equations can be localized to get

$$\dot{\eta}_0 - \frac{\dot{r}}{\theta} + \nabla_x \cdot \left(\frac{\mathbf{q}_0}{\theta}\right) \geq 0, \tag{4.55}$$

$$-[\![\eta_0]\!] s_n^0 - \left[\!\!\left[\frac{\mathbf{q}_0 \cdot \hat{\mathbf{n}}_0}{\theta}\right]\!\!\right] \geq 0. \tag{4.56}$$

Since the material experiences adiabatic environment under shock conditions, heat generation and conduction can be ignored, i.e., $\dot{r} = \mathbf{q} = 0$. Next, the Helmholtz energy of the material is introduced using the following,

$$H_0 = E_0 + \theta\eta_0. \tag{4.57}$$

Plugging (4.57) in (4.50) using (4.55) gives,

$$\dot{H}_0 + \nabla_y \phi \cdot \dot{\mathbf{p}}_0 + \eta\dot{\theta} - (\mathbb{S}_0 - \mathbf{T}_M^0) \cdot \dot{\mathbf{F}} \geq 0. \tag{4.58}$$

Constitutive Equations

Following (4.52) and (4.58), the interfacial energy W_σ and Helmholtz energy H_0 can be expressed as $W_\sigma = W_\sigma(\sigma)$ and $H_0 = H_0(\mathbf{F}, \mathbf{p}_0, \theta)$. Using Coleman-Noll arguments, the following equations can be recovered:

$$\frac{\partial H_0}{\partial \mathbf{p}_0} + \mathbf{F}^{-T}\nabla_x \phi = 0 \text{ in } B, \tag{4.59}$$

$$\frac{\partial H_0}{\partial \theta} + \eta_0 = 0 \text{ in } B, \tag{4.60}$$

$$\frac{\partial H_0}{\partial \mathbf{F}} - (\mathbb{S}_0 - \mathbf{T}_M^0) = 0 \text{ in } B, \text{ and} \tag{4.61}$$

$$\frac{dW_\sigma}{d\sigma} + \phi = 0 \text{ on } S. \tag{4.62}$$

Using the above equation, a stress tensor

$$\mathbf{T}_0 = \mathbb{S}_0 - \mathbf{T}_M^0 = \frac{\partial H_0}{\partial \mathbf{F}} \tag{4.63}$$

can be introduced in the reference configuration. The equations (4.59), (4.60) and (4.61) establish a relation between conjugate quantities $\mathbf{p}$ and $\mathbf{E}$, η and θ; and $\mathbf{F}$ and $\mathbf{T}_0$ through Helmholtz energy. Next, plugging (4.57) in (4.51) using (4.56) gives

$$d\, s_n^0 \geq 0, \tag{4.64}$$

where d is the driving force acting on the phase boundary given by

$$d = [\![H_0 + \langle \eta \rangle \theta + \nabla_y \phi \cdot \mathbf{p}_0 - \mathbf{F}\hat{\mathbf{n}}_0 \cdot \langle \mathbb{S}_0 \hat{\mathbf{n}}_0 \rangle + (\hat{\mathbf{n}} \cdot \mathbf{T}_M \hat{\mathbf{n}})\ J]\!] + (W_\sigma + \phi\sigma)\kappa\langle J \rangle. \tag{4.65}$$

The expression for driving force (4.65) contains terms corresponding to the electro-thermomechanical coupling of the material. In a purely mechanical case, the driving force contains far fewer terms. The third term in the driving force is a product of conjugate variables: polarization and electric field $\mathbf{E} = -\nabla_y \phi$. This term reduces the total driving force, hence resisting the motion of the phase boundary. The fourth term is the electromechanical equivalent of the purely mechanical case where the total stress is now replaced by $\mathbb{S}_0 = \mathbf{T}_0 + \mathbf{T}_M^0$. The fifth term corresponds to the volumetric deformation caused by the Maxwell stress. The final term is the contribution from the surface charges present on the curved phase boundary. For a straight phase boundary with no curvature κ, this term goes away. The expression (4.65) is consistent with one derived by James [40] in magnetism under isothermal environment.

With the expression for the driving force d derived, the analysis can now be continued by choosing a kinetic relation between d and s_n^0. Kinetic relations [1] govern the motion of the phase boundary in an energetically favorable direction. As explained in Chapter 2, shock wave problems are supplemented by Hugoniot relations and Lax entropy criteria to obtain a unique solution. However, in the case of ferroelectric materials, involving electro-thermomechanical coupling, it is difficult to describe a Hugoniot. Kinetic relation can be interpreted as the thermodynamic equivalent of specifying a linear law and the Lax entropy criteria to obtain a unique solution. Further, kinetic relations capture the entire electro-thermomechanical coupling of the material and hence are physically more relevant to the analysis.

4.3 Simplified one-dimensional analysis

As a first step towards the full fledged material model, a simple uncoupled one-dimensional analysis is performed in this section. The electrical, thermal and

mechanical components are completely separated and a simple analysis is performed to understand the behavior of current generation. A one dimensional material of length L is chosen with a phase boundary traveling at some speed V in the Lagrangian frame. In this analysis, the motion of the phase boundary is not the focus. Rather, a constant speed is V is enforced to understand direct relation between the phase boundary motion and current output. At a given instant, the location of the phase boundary is marked as $x = s$. The electrical energy of the material is modeled as

$$H_p^{1D} = \begin{cases} \frac{\alpha_p}{2} p_0^2 & \text{in anti-ferroelectric phase} \\ \frac{\alpha_p}{2}(p_0 - p_1)^2 & \text{in ferroelectric phase.} \end{cases} \tag{4.66}$$

where p_1 is the spontaneous polarization associated with the ferroelectric phase and α_p is related to the relative permittivity of the material. Following 4.59, the electric field can be expressed as

$$E_p^{1D} = \begin{cases} \alpha_p p_0 & \text{in anti-ferroelectric phase} \\ \alpha_p(p_0 - p_1) & \text{in ferroelectric phase.} \end{cases} \tag{4.67}$$

To the left of the phase boundary, the material is in anti-ferroelectric phase, and to the right of the phase boundary the material is in ferroelectric phase. The quantities like polarization, electric field and electric displacement in the anti-ferroelectric phase are represented as p_L, E_L^{1D} and D_L^{1D} respectively. Similarly, for the ferroelectric phase, these quantities are represented with p_R, E_R^{1D} and D_R^{1D} respectively. Following (4.67) and (4.9),

$$\begin{aligned} &p_L = E_L^{1D}/\alpha_p, \\ &D_L^{1D} = p_L + \varepsilon_0 E_L^{1D} = E_L^{1D}/\alpha_p + \varepsilon_0 E_L^{1D} = \left(\varepsilon_0 + \frac{1}{\alpha_p}\right) E_L^{1D} = \varepsilon E_L^{1D}, \end{aligned}$$

for the anti-ferroelectric phase where $\varepsilon = (\varepsilon_0 + 1/\alpha_p)$ is the relative permittivity of the material. Similarly for the ferroelectric material,

$$\begin{aligned} &p_R = p_1 + E_R^{1D}/\alpha_p, \\ &D_R^{1D} = p_R + \varepsilon_0 E_R^{1D} = p_1 + E_R^{1D}/\alpha_p + \varepsilon_0 E_R^{1D} = p_1 + \left(\varepsilon_0 + \frac{1}{\alpha_p}\right) E_R^{1D} = p_1 + \varepsilon E_R^{1D}. \end{aligned}$$

Since the electric displacement should be continuous across the phase boundary,

$$D_L^{1D} = D_R^{1D} \Rightarrow \varepsilon E_L^{1D} = p_1 + \varepsilon E_R^{1D} \Rightarrow E_L^{1D} = \frac{p_1}{\varepsilon} E_R^{1D}. \tag{4.68}$$

The current I^{1D} flowing through the external circuit R can be expressed as

$$I^{1D} = -\frac{dD_R^{1D}}{dt} = -\varepsilon\frac{dE_R^{1D}}{dt} = -\varepsilon V\frac{dE_R^{1D}}{ds}. \tag{4.69}$$

The potential across the external resistance can be expressed in terms of electric field as follows,

$$V^{1D} = sE_L^{1D} + (L-s)E_R^{1D}. \tag{4.70}$$

Using Ohm's Law $V^{1D} = I^{1D}R$ and using (4.68) and (4.69),

$$\begin{aligned} s\frac{p_1}{E} + sE_R^{1D} + (L-s)E_R^{1D} &= -\varepsilon VR\frac{dE_R^{1D}}{ds}, \\ \varepsilon VR\frac{dE_R^{1D}}{ds} + s\frac{p_1}{E} + E_R^{1D}L &= 0. \end{aligned} \tag{4.71}$$

Solving the above differential equation for E_R^{1D} gives

$$E_R^{1D} = \frac{p_1 VR}{L^2} - \frac{p_1}{L\varepsilon}s + c'\exp\left(-\frac{L}{\varepsilon VR}s\right), \tag{4.72}$$

where the constant c' can be determined by the initial condition $E_R^{1D}(s=0) = 0$ because $V^{1d}(s=0) = 0$. Finally, using (4.69) this leads to

$$\begin{aligned} & E_R^{1D} = -\frac{p_1 s}{L\varepsilon} + \frac{p_1 VR}{L^2}\left(1 - \exp\left(-\frac{L}{\varepsilon VR}s\right)\right) \\ \Rightarrow \qquad & I^{1D}(s) = \frac{p_1 V}{L}\left(1 - \exp\left(-\frac{L}{\varepsilon VR}s\right)\right). \end{aligned} \tag{4.73}$$

The expression (4.73) shows that the current follows an exponential profile achieving a steady value for large s. Since the maximum value of s can only be L, the highest current can be achieved only when the entire material has depolarized. The current also increases with increasing p_1 and decreasing sample length L. Finally, increase in the speed of the phase boundary increases the current magnitude and decreases the rise time.

4.4 Shock wave propagation in ferroelectric materials

In Section 4.2, governing equations for large deformation, dynamic behavior of ferroelectric material under generalized electromechanical loading were derived. In this section, these equations will be used to study a canonical uniaxial plate impact problem in the field. Following the analysis in Section 4.3, complete electro-thermomechanical coupling is studied in this section.

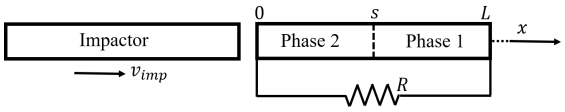

Figure 4.6: Schematic of the canonical uniaxial impact problem. A phase boundary propagates in a one dimensional system after being impacted by a flyer. The two ends of the ferroelectric material are connected through a resistor R. Current flowing through R is tracked.

Problem description

Figure 4.6 shows the schematic of the plate impact problem under consideration. The geometry of the problem ensures that the problem is uniaxial. A thermoelastic flyer of length L_f traveling at speed v_{imp} hits a ferroelectric target of length L. The moment of impact is set as time $t = 0$, while the point of impact is set at $x = 0$ in the Lagrangian frame. A phase boundary $x = s$ propagates into the material upon impact. It is assumed that thin electrodes are placed at $x = 0, L$. The electrodes are connected via a resistance R, and the current I flowing through it is tracked. To further simplify the analysis, small strain conditions are assumed which simplify the jump equations to

$$\begin{aligned} [\![t]\!] + \dot{s}[\![\rho v]\!] &= 0, \\ [\![v]\!] + \dot{s}[\![\varepsilon]\!] &= 0, \\ [\![p - \varepsilon_0 \phi_{,x}]\!] &= \sigma, \end{aligned}$$

where t, $\dot{s}$, ρ, v, ε, p, ϕ and σ denote the overall traction, speed of the phase boundary, density of the material, particle speed, strain, polarization, Maxwell potential and surface charge density on the phase boundary respectively. For simplicity of this analysis, the surface charge density is ignored. It should be noted that the governing equations account for the surface charges, and it can be solved for by making an appropriate choice of the constitutive law for W_σ. The model for the flyer and the ferroelectric material is explained in the next section. As explained earlier, a kinetic relation between the driving force d and the speed of the phase boundary is needed to obtain a unique solution. Conventionally, this is expressed as

$$\dot{s} = f(d). \tag{4.74}$$

Material model description

In this section, the material models for the flyer and the target will be described.

Ferroelectric material

The Helmholtz energy of the ferroelectric material is chosen as follows:

$$H_0(\varepsilon, p_0, \theta) = H_p(p_0) + H_\varepsilon(\varepsilon, \theta). \tag{4.75}$$

In other words, the Helmholtz energy is assumed to be a combination of two terms: one purely dependent on polarization and the other a combined function of strain and temperature. Typically, for a ferroelectric material undergoing FE-AFE transition, strain is considered to be the primary order parameter [30]. As such, H_ε is taken to be a double welled potential in strain with energy wells changing with temperature. H_p is also taken to be a double welled potential with spontaneous polarization appearing in the ferroelectric phase. Further, ordinary electrostriction is ignored because it is an order of magnitude smaller. The shock loading is inducing a phase transition, and as such AFE phase is referred to as shocked phase while FE phase is the unshocked phase.

$$H_p(p_0) = \begin{cases} \frac{\alpha_p}{2} p_0^2 & \text{in shocked phase} \\ \frac{\alpha_p'}{2}(p_0 - p_1)^2 & \text{in unshocked phase,} \end{cases} \quad \text{and} \tag{4.76}$$

$$H_\varepsilon(\varepsilon, \theta) = \begin{cases} \frac{E}{2}\varepsilon^2 - \alpha E \varepsilon(\theta - \theta_T) - c_1 \theta \log(\theta/\theta_T) & \text{in unshocked phase} \\ \dfrac{E'}{2}\left((\varepsilon - \varepsilon_T)^2 + \varepsilon_T M(\theta - \theta_T)\right) & \\ -\alpha E' \varepsilon(\theta - \theta_T) - c_1 \theta \log(\theta/\theta_T) & \text{in shocked phase,} \end{cases} \tag{4.77}$$

where p_1 refers to the spontaneous polarization in the ferroelectric phase. E, E', α, θ_T, c_1 and ε_T denote elastic modulus in unshocked phase, elastic modulus in the shocked phase, coefficient of thermal expansion, transformation temperature, specific heat capacity and transformation strain, respectively. Further, M is a material constant that relates the latent heat of the material (ΔH_ε in the Figure 4.7a). Following (4.63), the Cauchy stress can be defined as

$$\sigma_c = \begin{cases} E\left(\varepsilon - \alpha(\theta - \theta_T)\right) & \text{in unshocked phase} \\ E'\left(\varepsilon - \varepsilon_T - \alpha(\theta - \theta_T)\right) & \text{in shocked phase.} \end{cases} \tag{4.78}$$

The schematic of H_ε landscape and the Cauchy stress is represented in Figures 4.7a and 4.7b. As temperature changes the energy minima $\varepsilon_1(\theta)$ and $\varepsilon_2(\theta)$ change, keeping the transformation strain, ε_T, constant. Further, the difference in energy levels ΔH_ε changes as the temperature changes, making one phase more stable than

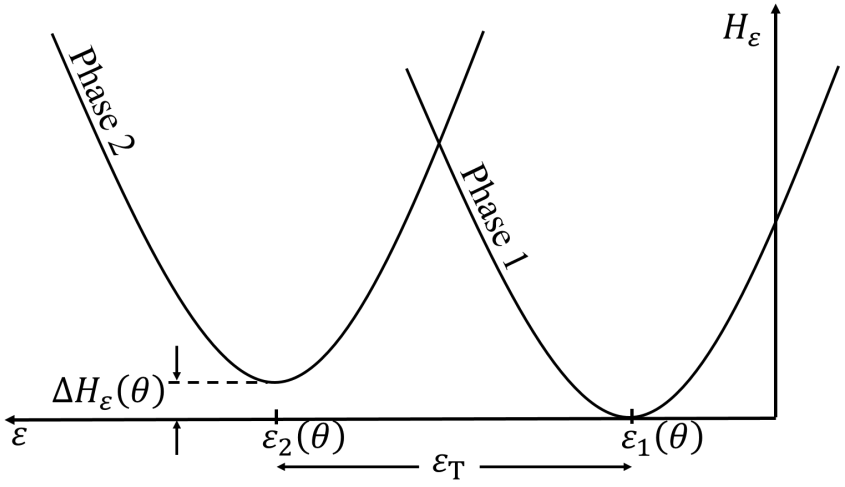

(a)

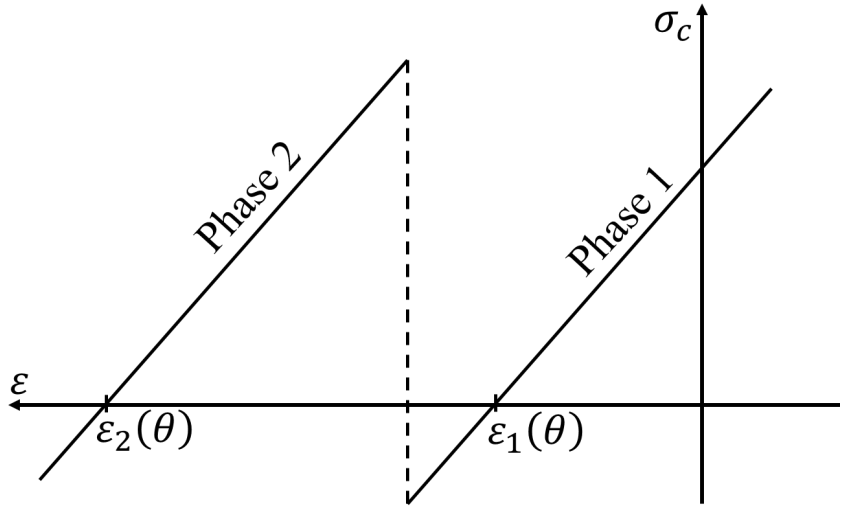

(b)

Figure 4.7: (a) H_ε energy landscape of the ferroelectric material. The energy wells change based on temperature, but ε_T is unchanged. (b) Schematic of Cauchy stress σ_c profile for the ferroelectric material.

the other beyond certain threshold. Following (4.59), the electrical field can be expressed as

$$E_p = \begin{cases} \alpha_p(p_0 - p_1) & \text{in unshocked phase} \\ \alpha_p p_0 & \text{in shocked phase.} \end{cases} \tag{4.79}$$

Similarly, entropy can be expressed as

$$\eta_0 = \begin{cases} \alpha E\varepsilon + c_1\left(1 + \log\left(\theta/\theta_T\right)\right) & \text{in unshocked phase} \\ \alpha E'\varepsilon + c_1\left(1 + \log\left(\theta/\theta_T\right)\right) - E'\varepsilon_T M & \text{in shocked phase.} \end{cases} \tag{4.80}$$

Impactor material

A material model for the flyer can be chosen along the lines of (4.77). The impactor is assumed to be purely thermoelastic, not capable of phase transitions. As such, only one energy well is needed to describe the material.

$$H_0^f = \frac{E_f}{2}\varepsilon^2 - \alpha_f E_f \varepsilon(\theta - \theta_{Tf}) - c_{1f}\theta\log(\theta/\theta_{Tf}), \tag{4.81}$$

where E_f, α_f, θ_{Tf} and c_{1f} represent elastic modulus, coefficient of thermal expansion, reference temperature for thermal expansion and specific heat capacity of the flyer.

Numerical method

In this section, the numerical method for solving the impact problem is presented. The method follows the ideas introduced by Zhong [88] and implemented by Purohit [64]. Due to the electro-thermomechanical coupling and the nonlinear nature of the problem, slight variations were made to the Gudonov scheme. The main idea is to track the moving phase boundary throughout the medium, and capture the elastic waves and other minor waves.

Mesh creation/discretization

For convenience, the calculations are performed in the reference configuration. Initially, the flyer and the target are descretized into N_f and N intervals, respectively, of equal lengths. This makes the intervals in the flyer and the target of lengths h_f and h, respectively. The technique involves capturing elastic waves by averaging states within every interval. This introduces some errors into the technique in the form of numerical dissipation. In order to prevent numerical instabilities due to averaging, care must be taken to avoid averaging across the two phases of the phase

boundary [88]. As such, a nodal point should always be present at the points of large discontinuities such as the phase boundary and material interfaces. Since the phase boundary keeps moving, the mesh needs to be updated after every time step to ensure that a nodal point lies on it.

Non-dimensionalization

Analyzing the expressions for the Helmholtz energy for ferroelectric and flyer material, it is possible to define following characteristic wave speeds

$$c = \sqrt{\frac{E}{\rho}}, \qquad c' = \sqrt{\frac{E'}{\rho}}, \qquad c_f = \sqrt{\frac{E_f}{\rho_f}}, \tag{4.82}$$

for the ferroelectric material in unshocked phase, the ferroelectric material in shocked phase and the flyer, respectively. Here ρ and ρ_f denote the density of the target and the flyer in the reference frame. The characteristic speeds can be used to introduce the following non-dimensional quantities,

$$\tilde{x} = \frac{x}{L}, \;\; \tilde{t} = \frac{tc}{L}, \;\; \tilde{v} = \frac{v}{c}, \;\; \tilde{p}_0 = \frac{p_0}{p_1}, \;\; \tilde{\theta} = \frac{\theta}{\theta_T}, \;\; \tilde{c'} = \frac{c'}{c}, \;\; \tilde{c}_f = \frac{c_f}{c}, \;\; \tilde{\rho}_f = \frac{\rho_f}{\rho}.$$

For notational purposes, the non-dimensional quantities are denoted by a tilde accent. Using the above non-dimensional quantities, it is possible to further non-dimensionalize energies as follows

$$\tilde{H}_0 = \frac{H_0}{E} = \begin{cases} \frac{1}{2}\varepsilon^2 - \tilde{\alpha}\varepsilon(\tilde{\theta}-1) - \tilde{c}_1\tilde{\theta}\log\tilde{\theta} + \frac{\tilde{\alpha}'_p}{2}(\tilde{p}_0-1)^2 & \text{in unshocked phase} \\ \frac{1}{2}\tilde{E}'\left((\varepsilon-\varepsilon_T)^2 + \varepsilon_T\tilde{M}(\tilde{\theta}-\tilde{\theta}_T)\right) - \tilde{\alpha'}\varepsilon(\tilde{\theta}-1) & \\ -\tilde{c}_1\tilde{\theta}\log\tilde{\theta} + \dfrac{\tilde{\alpha}_p}{2}\tilde{p}_0^2 & \text{in shocked phase,} \end{cases} \tag{4.83}$$

$$\tilde{H}_0^f = \frac{H_0^f}{E} = \frac{\tilde{E}_f}{2}\varepsilon^2 - \tilde{\alpha}_f\varepsilon(\tilde{\theta}-\tilde{\theta}_{Tf}) - \tilde{c}_{1f}\tilde{\theta}\log\left(\frac{\tilde{\theta}}{\tilde{\theta}_{TF}}\right), \tag{4.84}$$

where $\tilde{E}' = E'/E$, $\tilde{\alpha} = \alpha\theta_T$, $\tilde{\alpha'} = \alpha\theta_T\tilde{E}'$, $\tilde{c}_1 = c_1\theta_T/E$, $\tilde{\alpha}_p = \alpha_p p_1^2/E$, $\tilde{\alpha'}_p = \alpha'_p p_1^2/E$ and $\tilde{M} = M\theta_T$ are the non-dimensional constants for the ferroelectric material, while $\tilde{E}_f = E_f/E$, $\tilde{\alpha}_f = \alpha_f E_f\theta_t/E$, $\tilde{\theta}_{Tf} = \theta_{Tf}/\theta_T$ and $\tilde{c}_{1f} = c_{1f}\theta_T/E$ denote the non-dimensional constants for the flyer material. Next, electric field and entropy can be non-dimensionalized in a consistent way

$$\tilde{E}_p = \frac{\partial\tilde{H}_0}{\partial\tilde{p}_0} = \begin{cases} \tilde{\alpha'}_p(\tilde{p}_0-1) & \text{in unshocked phase} \\ \tilde{\alpha}_p\tilde{p}_0 & \text{in shocked phase,} \end{cases} \tag{4.85}$$

$$\tilde{\eta}_0 = -\frac{\partial \tilde{H}_0}{\partial \tilde{\theta}} = \begin{cases} \tilde{\alpha}\varepsilon + \tilde{c}_1(1 + \log(\tilde{\theta})) & \text{in unshocked phase} \\ -\varepsilon_T \tilde{M} + \tilde{\alpha'}\varepsilon + \tilde{c}_1(1 + \log(\tilde{\theta})) & \text{in shocked phase.} \end{cases} \tag{4.86}$$

Along the same lines, a non-dimensionalized electric displacement can be consistently defined as $\tilde{D}_p = D_p/p_1 = \tilde{p}_0 + \tilde{\varepsilon}_0\tilde{E}$ where $\tilde{\varepsilon}_0 = E\varepsilon_0/p_1^2$. Using this, non-dimensional Maxwell stress $\tilde{\sigma}_M = \tilde{E}_p\tilde{D}_p - \frac{\tilde{\varepsilon}_0}{2}\tilde{E}_p^2 = \frac{\sigma_M}{E}$ and Cauchy stress $\tilde{\sigma}_c = \frac{\partial \tilde{H}_0}{\partial \varepsilon} = \frac{\sigma_c}{E}$ can be defined.

Nucleation and initial conditions

An FE-AFE phase boundary is nucleated at $\tilde{x} = \tilde{h}_t = h_t/L$ at time $\tilde{t} = 0$. The ferroelectric phase lies to the right, $\tilde{x} \in [\tilde{h}_t, 1]$, and the anti-ferroelectric phase lies to the left, $\tilde{x} \in [0, \tilde{h}_t]$, of the phase boundary. Initially, there is no current (hence no voltage) across the resistor. This ensures a certain initial configuration of the polarization in the material, calculated by solving the following equations:

$$\tilde{p}_L + \tilde{\varepsilon}_0\tilde{\alpha}_p\tilde{p}_L = \tilde{p}_R + \tilde{\varepsilon}_0\tilde{\alpha'}_p(\tilde{p}_R - 1)$$
$$\tilde{V} = \tilde{h}_t\tilde{E}_L + (1 - \tilde{h}_t)\tilde{E}_R = \tilde{h}_t\tilde{\alpha}_p\tilde{p}_L + (1 - \tilde{h}_t)\tilde{\alpha'}_p(\tilde{p}_R - 1) = 0,$$

where $\tilde{p}_L$, $\tilde{p}_R$ and $\tilde{V}$ denote the non-dimensional polarization to the left of the phase boundary, non-dimensional polarization to the right of the phase boundary and the non-dimensional voltage across the resistor.

Riemann problems and conservation laws

The choice of Helmholtz energy and definition of characteristic speeds enable solving the phase boundary problem by solving Riemann problems at every node and time step. Riemann problems are solved to obtain information of the states at the next time step. The method is as follows: At any node $\tilde{x}_i$ in the target at time $\tilde{t}$, the domain $\omega_i^t = [a, b]\times[\tilde{t}, \tilde{t}+\Delta\tilde{t}]$ is considered in the $X-t$ plane, where $a = \frac{1}{2}(\tilde{x}_i+\tilde{x}_{i-1})$ and $b = \frac{1}{2}(\tilde{x}_i + \tilde{x}_{i+1})$. The first step is to solve the conservation of momentum problem in the domain ω_i^t by keeping the temperature $\tilde{\theta}_i$ constant. Next, the temperature is updated by solving the conservation of energy equation. Finally the states in the interval for the next time step are obtained over the interval. The exact procedure and Riemann problems are explained below.

Ferroelectric material

Quantities like strain ε_i, polarization $\tilde{p}_i$, and particle velocity $\tilde{v}_i$, are defined on

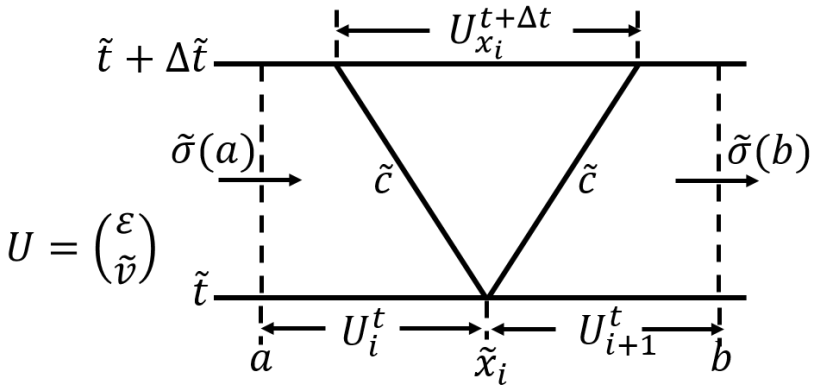

(a)

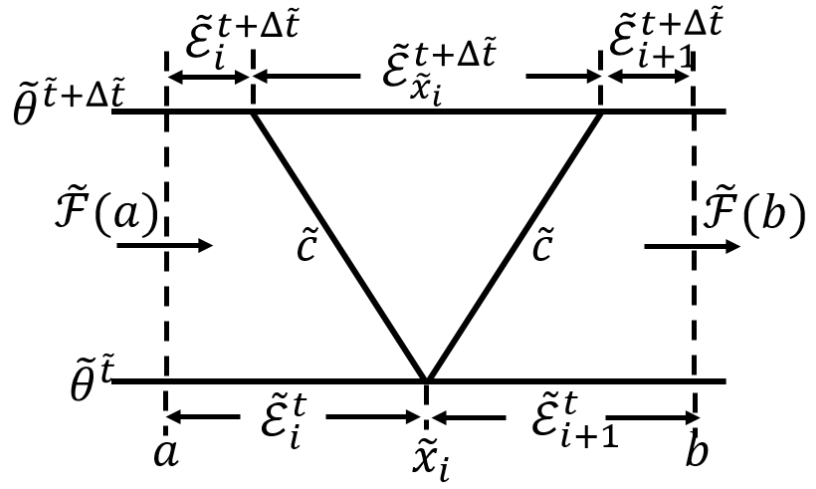

(b)

Figure 4.8: (a) Riemann problem at the node $\tilde{x}_i$ other than at a phase boundary or at either of the ends of the material. The problem is solved keeping the temperature constant. (b) Temperature update at the node following conservation of energy equations.

the intervals $(\tilde{x}_i, \tilde{x}_{i+1})$ of the target, while the temperature $\tilde{\theta}_i$ is defined at node $\tilde{x}_i$. Since there is no ordinary electrostriction in this analysis, the polarization is piecewise constant across the phase boundary for every time step. The non-dimensional polarization to the left and the right of the phase boundary is denoted by $\tilde{p}_L$ and $\tilde{p}_R$. Figure 4.8a shows the Riemann problem at a node other than the phase boundary and the physical boundary of the material. For this Riemann problem, the polarization remains constant. As such the unknown U is just strain and particle velocity as shown in Figure 4.8a. The following conservation equations are solved

in the domain ω_i^t for ε and $\tilde{v}$ [64]:

$$\int_{\tilde{t}}^{\tilde{t}+\Delta\tilde{t}} \left(\frac{d}{d\tilde{t}} \int_a^b \tilde{v}\, dx \right) d\tilde{t} = \int_{\tilde{t}}^{\tilde{t}+\Delta\tilde{t}} \tilde{\sigma}|_a^b \, d\tilde{t}$$

$$\Rightarrow \quad \left[\int_a^b \tilde{v}\, dx \right]_{\tilde{t}}^{\tilde{t}+\Delta\tilde{t}} = \int_{\tilde{t}}^{\tilde{t}+\Delta\tilde{t}} \tilde{\sigma}|_a^b \, d\tilde{t}, \tag{4.87}$$

$$\int_{\tilde{t}}^{\tilde{t}+\Delta\tilde{t}} \tilde{v}|_a^b + \int_a^b \varepsilon|_{\tilde{t}}^{\tilde{t}+\Delta\tilde{t}} = 0. \tag{4.88}$$

The Riemann problem at the phase boundary consists of two elastic waves and a phase boundary as represented by Figure 4.9a. In this problem, polarization is also important due to spontaneous polarization associated with the phase transition. Hence, polarization is also updated with every time step. Aside from (4.87) and (4.88), the following equations are also present across the phase boundary at time $\tilde{t} + \Delta\tilde{t}$:

$$\begin{aligned}
\tilde{\sigma}(\varepsilon_{x_{iL}}^{\tilde{t}+\Delta\tilde{t}}, \tilde{\theta}^{\tilde{t}}, \tilde{p}_L^{\tilde{t}+\Delta\tilde{t}}) - \tilde{\sigma}(\varepsilon_{x_{iR}}^{\tilde{t}+\Delta\tilde{t}}, \tilde{\theta}^{\tilde{t}}, \tilde{p}_R^{\tilde{t}+\Delta\tilde{t}}) + \tilde{\dot{s}}(\tilde{v}_{x_{iL}}^{\tilde{t}+\Delta\tilde{t}} - \tilde{v}_{x_{iR}}^{\tilde{t}+\Delta\tilde{t}}) &= 0, \\
\tilde{v}_{x_{iL}}^{\tilde{t}+\Delta\tilde{t}} - \tilde{v}_{x_{iR}}^{\tilde{t}+\Delta\tilde{t}} + \tilde{\dot{s}}(\tilde{\varepsilon}_{x_{iL}}^{\tilde{t}+\Delta\tilde{t}} - \tilde{\varepsilon}_{x_{iR}}^{\tilde{t}+\Delta\tilde{t}}) &= 0, \\
\tilde{D}_p(\tilde{p}_L^{\tilde{t}+\Delta\tilde{t}}) - \tilde{D}_p(\tilde{p}_R^{\tilde{t}+\Delta\tilde{t}}) &= 0, \\
\tilde{d}(\tilde{\varepsilon}_{x_{iL}}^{\tilde{t}+\Delta\tilde{t}}, \tilde{\varepsilon}_{x_{iR}}^{\tilde{t}+\Delta\tilde{t}}, \tilde{p}_L^{\tilde{t}+\Delta\tilde{t}}, \tilde{p}_R^{\tilde{t}+\Delta\tilde{t}}, \tilde{\theta}^{\tilde{t}}) &= f(\tilde{\dot{s}}), \\
\tilde{V} = \tilde{s}^{\tilde{t}+\Delta\tilde{t}} \tilde{E}_p(\tilde{p}_L^{\tilde{t}+\Delta\tilde{t}}) + (1 - \tilde{s}^{\tilde{t}+\Delta\tilde{t}}) \tilde{E}_p(\tilde{p}_R^{\tilde{t}+\Delta\tilde{t}}) &= -\tilde{R} \frac{d\tilde{D}_p(\tilde{p}_R^{\tilde{t}+\Delta\tilde{t}})}{d\tilde{t}}.
\end{aligned}$$

The first two equations above correspond to the non-dimensionalized stress jump equation and non-dimensional compatibility equation across the phase boundary. The third equation corresponds to the continuity of electrical displacement across the phase boundary. The fourth equation is the non-dimesionalized version of the kinetic relation, where $\tilde{d} = d/E$. Finally, Ohm's law governs the flow of current in the external circuit. Here $\tilde{s} = \tilde{x}_i$ is the position of the phase boundary and $\tilde{R} = \frac{p_1^2 cR}{EL^2}$ is the non-dimensional equivalent of R. These equations are solved to obtain $\varepsilon_{x_{iL}}^{\tilde{t}+\Delta\tilde{t}}$, $\varepsilon_{x_{iR}}^{\tilde{t}+\Delta\tilde{t}}$, $\tilde{v}_{x_{iL}}^{\tilde{t}+\Delta\tilde{t}}$, $\tilde{v}_{x_{iR}}^{\tilde{t}+\Delta\tilde{t}}$, $\tilde{p}_L^{\tilde{t}+\Delta\tilde{t}}$, $\tilde{p}_R^{\tilde{t}+\Delta\tilde{t}}$ and $\tilde{\dot{s}}$.

The next step is to update the temperature using conservation of energy equations. Figures 4.8b and 4.9b show the temperature update problem corresponding to the Riemann problems in Figures 4.8a and 4.9a, respectively. Here $\tilde{\mathcal{E}}$ and $\tilde{\mathcal{F}}$ represent the non-dimensional total energy at a point and the non-dimensional rate of work

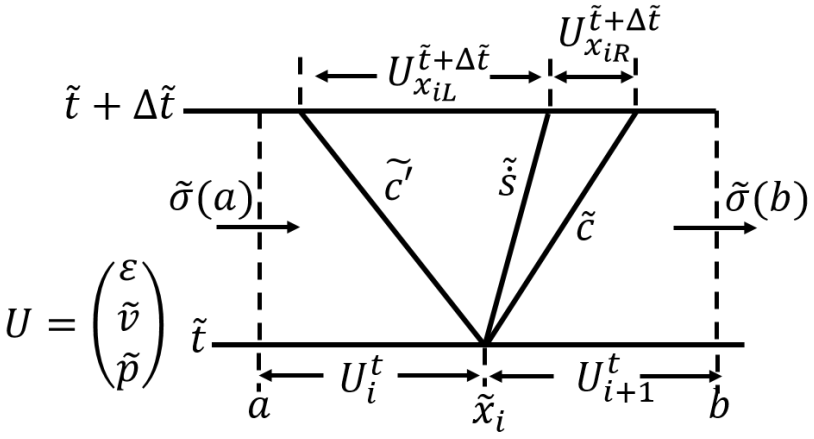

(a)

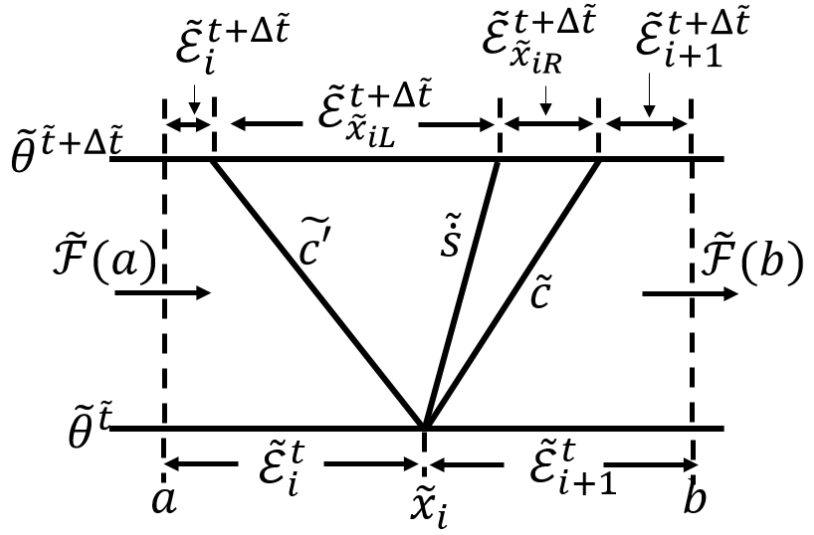

(b)

Figure 4.9: (a) Riemann problem to be solved at the phase boundary. The speed of the phase boundary is also unknown. This is where the kinetic relation comes into equation. (b) Temperature update at the phase boundary.

done on the domain, given by

$$\tilde{\mathcal{E}} = \tilde{E}_0 + \frac{1}{2}\tilde{v}^2 + \frac{1}{2}\tilde{\varepsilon}_0\tilde{E}_p^2,$$
$$\tilde{\mathcal{F}} = \tilde{\sigma}\tilde{v} + \tilde{\phi}\frac{d\tilde{D}}{d\tilde{t}}.$$

At time $\tilde{t}$, $\tilde{\mathcal{E}}$ and $\tilde{\mathcal{F}}$ are calculated using the temperature $\tilde{\theta}^{\tilde{t}}$. For time step $\tilde{t} + \Delta\tilde{t}$, the temperature is taken as $\tilde{\theta}^{\tilde{t}+\Delta\tilde{t}}$, and $\tilde{\mathcal{E}}$ for this time step is calculated using the new temperature. The general energy balance in the domain is given by

$$\int_{\tilde{t}}^{\tilde{t}+\Delta\tilde{t}} \left(\frac{d}{dt}\int_a^b \tilde{\mathcal{E}}\, dx\right) d\tilde{t} = \int_{\tilde{t}}^{\tilde{t}+\Delta\tilde{t}} \tilde{\mathcal{F}}|_a^b\, d\tilde{t} + \text{dissipation}$$
$$\Rightarrow \left[\int_a^b \tilde{\mathcal{E}}\, dx\right]_{\tilde{t}}^{\tilde{t}+\Delta\tilde{t}} = \int_{\tilde{t}}^{\tilde{t}+\Delta\tilde{t}} \tilde{\mathcal{F}}|_a^b\, d\tilde{t} + \text{dissipation}. \tag{4.89}$$

The above equation is solved in the domain ω_i^t for $\tilde{\theta}^{\tilde{t}+\Delta\tilde{t}}$. It is important to note that the dissipation term is absent in the problem in Figure 4.8b because elastic waves do not cause any dissipation. Further, the electrical components of the energy and the rate of work done are absent because the polarization is constant. The dissipation term is present across the phase boundary, and is given by $\int_{\tilde{t}}^{\tilde{t}+\Delta\tilde{t}} \tilde{d}\tilde{s}\, d\tilde{t}$. For simplicity, this is approximated as $\tilde{d}\tilde{s}\Delta\tilde{t}$. The driving force and the speed of the phase boundary are already known after solving the problem in Figure 4.9a. Across the phase boundary, electrical terms also start to play a role in the energy balance.

Target-flyer interface

Figure 4.10a represents the Riemann problem at the target-flyer interface. The conservation of momentum problem remains the same as earlier, except that the stresses for $\tilde{x} < 0$ are calculated using the material properties of the flyer. Once again, the polarization is kept constant during this calculation. Since the interface is always to the left of the phase boundary, the polarization is kept at $\tilde{p}_L^{\tilde{t}}$. The temperature update problem represented in Figure 4.10b is solved along similar lines. Once again, the electrical terms are not important for this problem. Finally, since the interface is stationary in the Lagrangian frame, there is no dissipation in the conservation of energy equation (4.89).

Flyer material

The flyer material is purely thermoelastic with no phase transitions or electrical coupling. As such, the only Riemann problem that occurs can be represented by

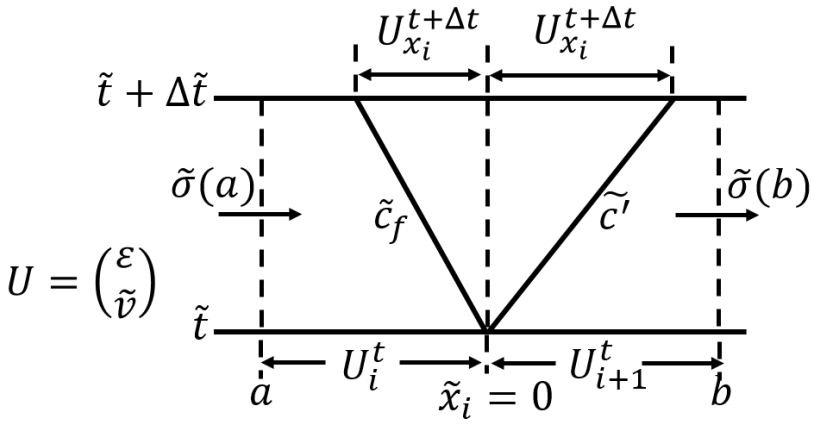

(a)

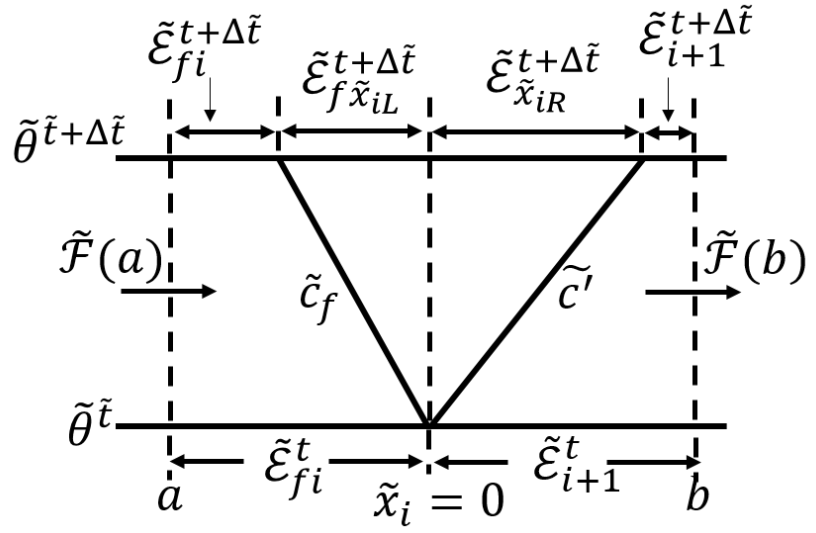

(b)

Figure 4.10: (a) Conservation of momentum problem at the flyer target interface. (b) Temperature update using the conservation of energy equations.

Figure 4.8a with $\tilde{c} = \tilde{c}_f$. Conservation of momentum (4.87) and compatibility (4.88) are solved to determine ε and $\tilde{v}$. Finally, temperature is updated (Figure 4.8b) by solving conservation of energy (4.89) equation with no dissipation.

Averaging and mesh updates

After solving the Riemann problems, the strains and particle velocity at the intervals for the next time step are obtained by averaging within the intervals. As explained earlier, it is important to keep a node point on the phase boundary to avoid averaging over different phases. Since the phase boundary has moved, the mesh needs to be updated at every time step to ensure that a node point lies on the phase boundary.

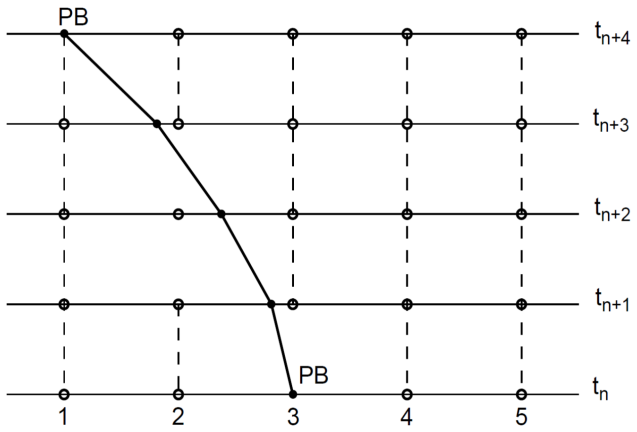

Figure 4.11: Schematic of the mesh update procedure [64]. As the phase boundary gets closer to a node, the node is removed and the mesh is resized. Once the phase boundary gets further away, the node is reinserted.

Further, the mesh size $\tilde{h} = h/L$ should be of certain minimum length $2c'\Delta\tilde{t}$. This is evident from the Riemann problem in Figure 4.8a, where the elastic waves can travel at speeds c'. In order to avoid information 'leaking' out of the domain, leading to numerical instabilities, the length of interval $[a, b]$ should be larger than $2c'\Delta\tilde{t}$. Further, in order to separate the Riemann problem at one node from the Riemann problem at another node, the nodes must be at least $2c'\Delta\tilde{t}$ distance apart. Since the phase boundary moves, the length of the intervals neighboring the phase boundary will change. As such the mesh needs to be updated with nodes added and/or removed to ensure the minimum critical length.

The procedure is same as the one followed by Purohit [64]. Figure 4.11 shows the schematic of the process of mesh update used. As the phase boundary moves, the node (node 3 in the figure) moves to follow the phase boundary. In other words, node 3 is removed and a new node is defined on the phase boundary. Once the phase boundary gets close to node 2, the mesh is updated and node 2 is removed. As the phase boundary moves further away, node 3 is reinserted and the mesh gets updated. The resizing of the nodes also effects the averaging of states. This introduces some numerical dissipation, which should be small because the averaging involves elastic waves.

Results: Parameter study

In this section, a quantitative analysis of the problem is presented. Over the years, various material properties have been reliably characterized via experiments ([34], [32], [69], [72], [78]). These values were taken as fixed. Some quantities are only

Parameters	Values
$\alpha_p,\ \alpha'_p$	$10^7\ \mathrm{PaC^{-2}m^4}$
p_1	$0.33\ \mathrm{C/m^2}$
$E,\ E'$	$100\ \mathrm{GPa}$
ρ	$5000\ \mathrm{kg\,m^{-3}}$
α	$10^{-6}\ \mathrm{K^{-1}}$
θ_T	$258\ \mathrm{K}$
c_1	$10^6\ \mathrm{JK^{-1}/m^3}$
ε_T	-0.005
M	$-4\times10^{-5}\ \mathrm{K^{-1}}$

Table 4.1: Choice of ferroelectric material parameters

Parameters	Values
ρ_f	$7800\ \mathrm{kg\,m^{-3}}$
c_f	$3200\ \mathrm{ms^{-1}}$
α_f	$10^{-6}\ \mathrm{K^{-1}}$
θ_{Tf}	$298\ \mathrm{K}$
c_{1f}	$10^6\ \mathrm{JK^{-1}/m^3}$

Table 4.2: Choice of flyer material parameters

Parameters	Values
L	$1\ \mathrm{mm}$
L_f	$1\ \mathrm{mm}$
N	100
N_f	150
Δt	$10^{-9}\ \mathrm{s}$
v_{impact}	$50-125\ ms^{-1}$
R	$10^{-4}\ \mathrm{ohm}$

Table 4.3: Choice of parameters in setting up the problem

known up to an order of magnitude under shock conditions. Consistent values are chosen for these, listed in Tables 4.1 and 4.2. Due to the lack of information on the kinetic relations for such materials, two broad classes - linear and stick-slip linear kinetics - are studied in detail. Different experimental configurations were also explored, starting from base values presented in Table 4.3.

Linear Kinetics

In this section, a linear kinetic relation between the driving force and the speed of the phase boundary is chosen as shown in Figure 4.12a:

$$d = d_s \dot{s}, \tag{4.90}$$

where d_s is chosen to be 10^3. Figure 4.12b shows the strain map on the $X - t$ diagram of the impact problem for an impact speed of 75 ms^{-1}. Upon impact ($t = 0$), an elastic precursor travels into the target followed by a phase boundary marked by a large change in strain. It should be noted that the elastic wave is not sharp. This is because the computational method involved captures the elastic wave into the averaging process. To the contrary, the phase boundary is tracked by mesh updating and hence appears sharp in Figure 4.12b. The elastic precursor travels into the material, and reflects off the free edge of the target as a tensile wave. This tensile wave then interacts with the phase boundary. Figure 4.13a shows the current output through the external circuit for an impact speed of 75 ms^{-1}. The current output has an exponential profile with a steady current pulse, which is consistent with experimental observations. The profile is also consistent with the expression (4.73) derived using a simple one-dimensional uncoupled analysis in Section 4.3. The sharp decline corresponds to the time the reflected elastic precursor interacts with the phase boundary in Figure 4.12b. In real experiments, the sample used is ceramic, which gets damaged by the time the reflected wave comes back. As such, there is no current output after the sharp decline. Figure 4.13b shows the temperature map on the $X - t$ diagram of the problem. Initially, both flyer and target are kept at room temperature of 298 K. It can be seen that the temperature rise associated with elastic waves is small, and can be barely seen in the flyer. The temperature increase across the phase boundary is around $5 - 10$ K.

The next step is to change the impact velocity of the flyer and study the current output in the external circuit. Figure 4.14a shows variation of current profiles with different impact speeds. It can be seen that the profiles are exponential with increasing current amplitude with impact speeds. This is consistent with various experimental observations [27], [34], [69]. Further, the rise times associated with the current profiles decrease with increasing impact speeds. Figure 4.14b shows the current profiles for different d_s values for same impact speed of 75 ms^{-1}. It can be seen that current decreases as d_s increases. This is because the speed of the phase boundary is directly related to the driving force via a kinetic relation. As

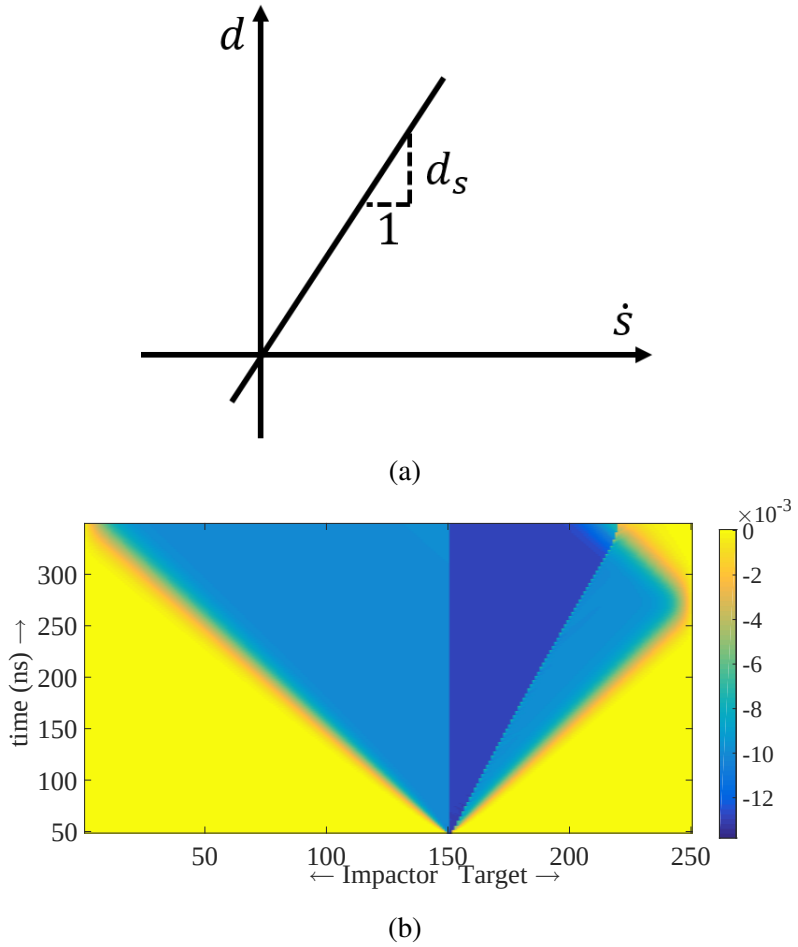

Figure 4.12: (a) Linear kinetic relation. (b) $X - t$ diagram of the impact problem. The colors correspond to the strain in the flyer and the ferroelectric target. The speed of the impact is 75 m/s.

d_s increases, the speed of the phase boundary decreases. Since the current profile is directly influenced by the speed of the phase boundary, the current amplitude decreases.

Figure 4.15a shows the variation of current profiles with target length, impacted upon by same impactor traveling at speed 75 ms^{-1}. It can be observed that the peak or steady current magnitude increases with decreasing length. This is because the fields generated are higher in the smaller sample, resulting in a higher voltage difference across the two ends. Further, the pulse obtained is shorter for shorter specimens. This is because the phase boundary travels a shorter distance before reaching the end of the sample. In other words, there is physically less material to depolarize. This is again consistent with experimental observations made by

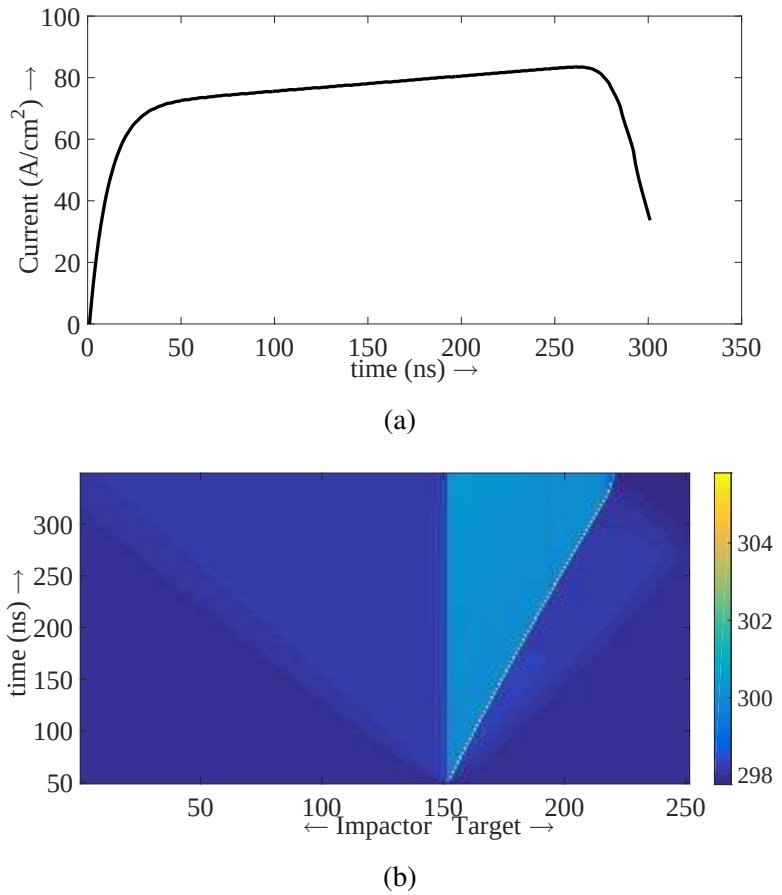

Figure 4.13: (a) Current profile obtained flowing through the resistor R for an impact speed of 75 ms^{-1}. (b) $X-t$ diagram of the impact problem. The colors correspond to the temperature in the flyer and the ferroelectric target.

[27]. Next, the flyer length is changed keeping the target length constant. Figure 4.15b shows the variation of current profiles with different flyer lengths. Here the profiles for different flyer lengths overlap. This effect is attributed to the interaction of the unloading release wave from the impactor free end with the moving phase boundary. For lengths $L_f = 0.7mm$ and $1mm$, the release wave comes after the phase boundary has already interacted with the reflected wave from the target free end. As such, the current drop seen for these profiles are because of the interaction between the phase boundary and the reflected elastic wave from the target free end. For $L_f = 0.1mm$ and $0.4mm$, the interaction between the release wave with the phase boundary happens before the reflected wave (from target end) comes back. As such, the current drop is observed much earlier here. Figure 4.16 shows the variation of current profiles with the resistance R in the external circuit. As R decreases the magnitude of steady current increases. This is indicative of inverse

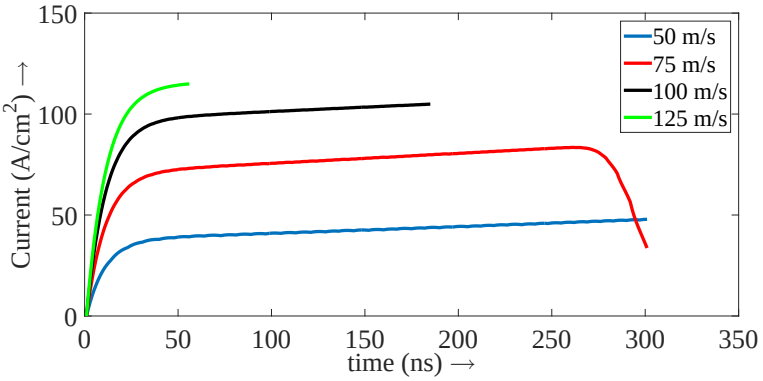

(a)

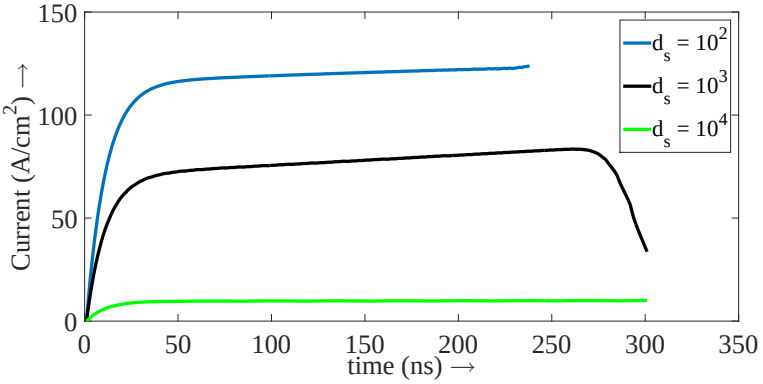

(b)

Figure 4.14: (a) Variation of current profile with increasing impact speeds. (b) Variation of current profiles with changing values of d_s for impact speed of 75 m/s.

proportionality with R. Further, the steady current is achieved faster as R decreases. This indicates the dependence of rise time in current over R.

Stick-slip Linear Kinetics

Next, a combination of stick-slip and linear kinetic relation is explored. A schematic of the stick-slip linear kinetic relation is shown in Figure 4.17a. In this analysis, $d_c = 10^6$, while $d_s = 10^3$. The strain map of the impact of a flyer traveling at speed 75 ms^{-1} is presented on the $X - t$ diagram of the problem. The strain map is very similar to the linear kinetics case presented in Figure 4.12b. Just as in Figure 4.12b, in this case, the phase boundary is clearly visible by the large change in strains. The phase boundary is again preceded by an elastic precursor which reflects off the free edge of the target and interacts with the propagating phase boundary. The temperature map for this impact process as shown in the $X - t$ diagram is presented

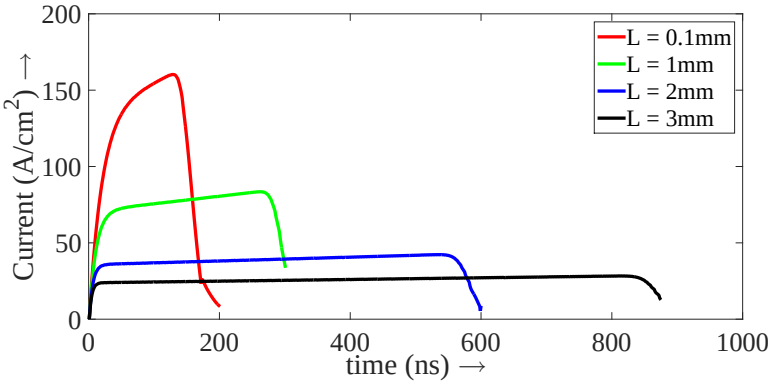

(a)

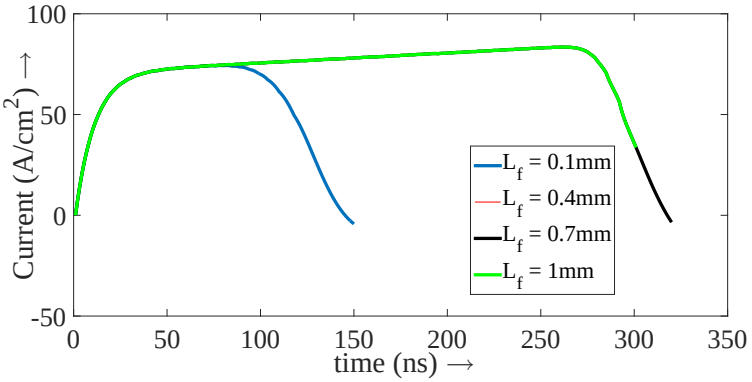

(b)

Figure 4.15: (a) Variation of current profile with increasing impact speeds. (b) Variation of current profiles with changing values of d_s for impact speed of 75 m/s.

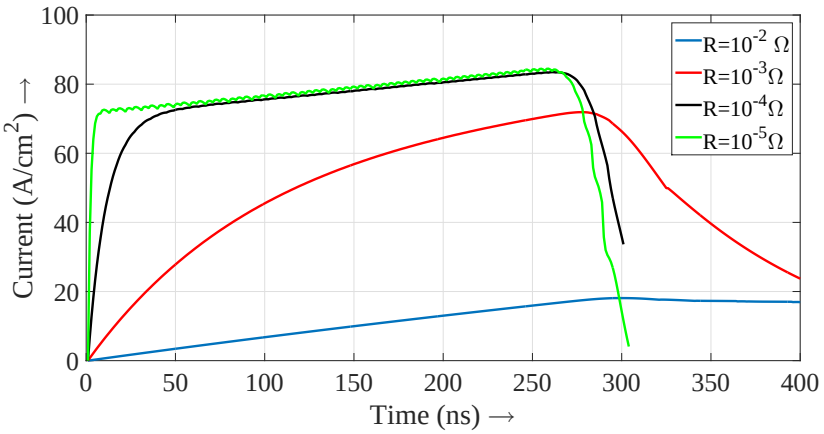

Figure 4.16: Variation of current profiles with R in the external circuit for the same impact speed 75 ms^{-1}.

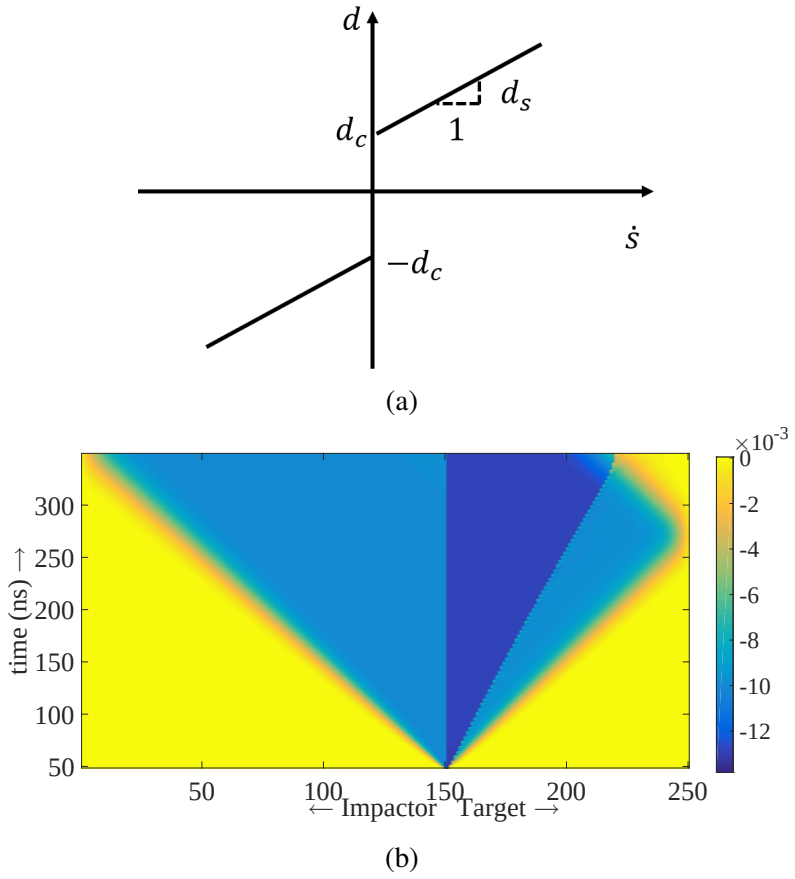

Figure 4.17: (a) Combination of Stick-slip and Linear kinetic relation. (b) $X - t$ diagram of the impact problem. The colors correspond to the strain in the flyer and the ferroelectric target. The speed of the impact is 75 m/s.

in Figure 4.18b. Again, the temperature rise associated with elastic waves is very small, while the temperature increase across the phase boundary is around $5K$. A comparison between the current profiles for linear and stick-slip linear kinetics is presented in Figure 4.18a. The current profile is for this kinetic law is also exponential, with a smaller steady magnitude and rise time than is the case with linear kinetics. This is because a portion of the driving force is gone to overcome the barrier d_c. The decrease in the speed of the phase boundary also explains the decrease in rise time of the current.

Comparison with experiments

In this section, the numerical results are compared to the experimental observations made by Furnish [34]. Since complete depolarization was observed for the impact speed of 65 ms^{-1} in experiments [34], a numerical study will be conducted for 65 ms^{-1} impact speed. Parameters for experimental setup and material properties

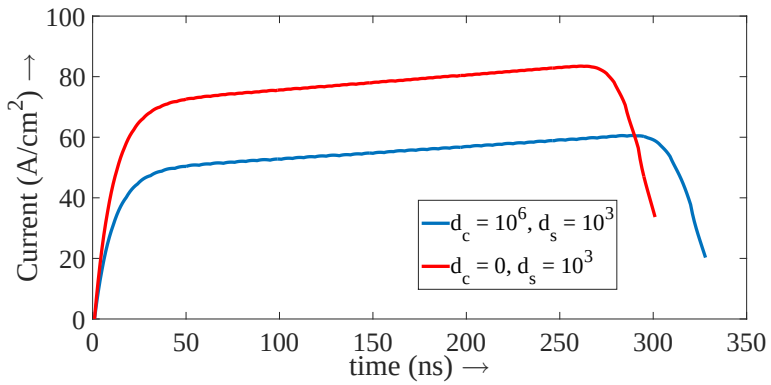

(a)

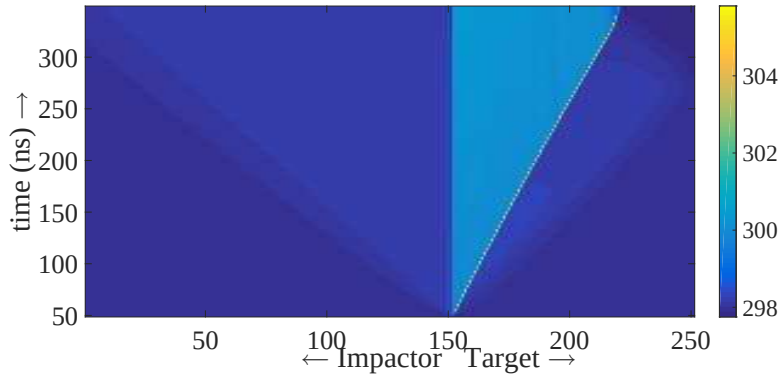

(b)

Figure 4.18: (a) Comparison of current profiles for Linear and Stick-Slip Linear Kinetic relation. (b) $X - t$ diagram of the impact problem. The colors correspond to the temperature in the flyer and the ferroelectric target.

presented in [34] are listed in Table 4.4. In order to obtain a close match to the experimental observations, parameters chosen for the material model and experimental setup are listed in Table 4.5. Further, an stick-exponential slip relation is employed for the kinetic law between the driving force and the phase boundary speed. The exact expression is given by

$$\dot{s} = \begin{cases} 0 & \text{when } |d| \leq d_c \\ c\left(1 - \exp\left(\frac{|d|-d_c}{\tau}\right)\right)\text{sign}(d_c) & \text{when } |d| > dc, \end{cases} \tag{4.91}$$

where c is the characteristic wave speed and d_c and τ are parameters for the kinetic relation. For this analysis, these parameters are chosen to be 10^6 and 8×10^6 respectively. Physically, this kinetic relation ensures that a critical force is required to move the phase boundary, and the speed of the phase boundary can never exceed the characteristic wave speed in the material. The charge profiles are computed for

Parameters	Values
L	4 mm
L_f	6 mm
ρ	$7300\,kg/m^3$
c	$4163\,ms^{-1}$
p_1	$\approx 0.30\,\mu C/cm^2$
v_{impact}	$65\,ms^{-1}$
R	1 ohm

Table 4.4: Setup and material parameters in experiments by Furnish [34]

Parameters	Values
α_p	6×10^7 PaC^{-2}m^4
α'_p	2×10^9 PaC^{-2}m^4
p_1	0.28 C/m^2
$c,\ c'$	$4163\,ms^{-1}$
ρ	7300 kg m^{-3}
α	10^{-6} K^{-1}
θ_T	198 K
c_1	10^7 JK^{-1}/m^3
ε_T	-0.008
M	8×10^{-4} K^{-1}

Parameters	Values
ρ_f	7800 kg m^{-3}
c_f	3200 ms^{-1}
α_f	10^{-6} K^{-1}
θ_{Tf}	298 K
c_{1f}	10^6 JK^{-1}/m^3
L	5 mm
L_f	6 mm
v_{impact}	$65\,ms^{-1}$
R	1 ohm

Table 4.5: Choice of material and setup parameters for simulations

the parameters listed in Tables 4.5 and compared to the experimental observations by Furnish [34], as shown in Figure 4.19b. It can be seen that the numerical simulations are able to capture experimental observations very closely. The charge profiles are exponential, and achieve a constant value close to p_1 indicating complete depolarization of the material. Numerical simulations capture the slope of the charge profiles (or the current) very accurately, with peak currents reaching 37 A/m^2. Finally, the time-scale of the depolarization process is also captured in the simulation.

It is a common practice to specify the Hugoniot of the material in the form of shock speed and particle velocity. As explained in Section 2.3, experimental investigation conducted over a broad range of materials point to a linear relationship between shock speed and particle velocity in the material. This is commonly expressed in terms of two parameters, C_0 and S, as expressed in equation (2.18). Figure 4.20 shows the shock speed vs particle speed Hugoniot over the range of seven orders of magnitude of resistance R in the external circuit. Most of the material properties

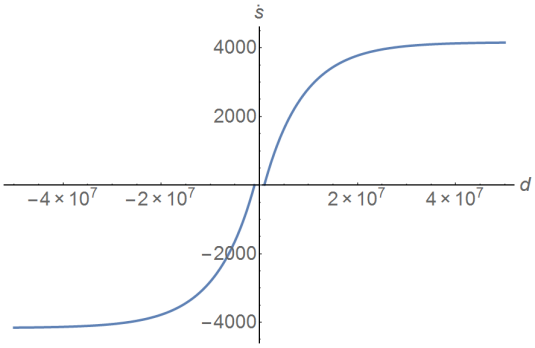

(a)

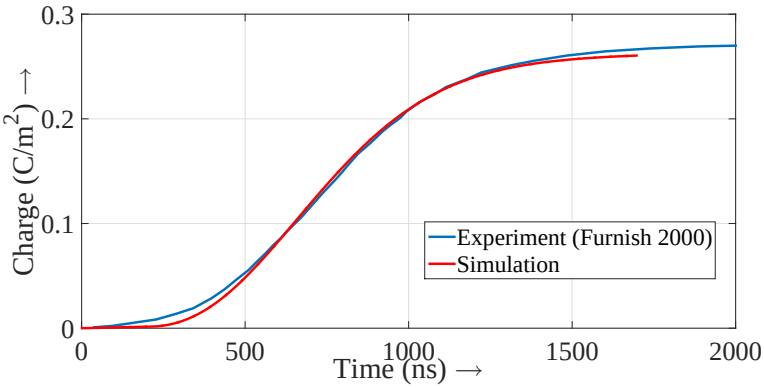

(b)

Figure 4.19: (a) Stick-exponential slip kinetic relation (b) Comparison of charge profiles from experiments and simulations

were taken from Table 4.5, except for p_1 and α'_p which were taken to be 0.33 C/m^2 and 10^9 PaC^{-2}m^4, respectively. The Hugoniot was generated for six impact speeds ranging from 55 ms^{-1} to 55 ms^{-1} with equal intervals. For a particular impact speed and R, the shock speed was averaged over a period of steady motion to remove numerical oscillations. Figure 4.20 shows a linear relationship between the shock speeds and particle velocity, which is consistent with the widely observed linear law.

Table 4.6 lists the numerically observed constants C_0 and S for the $U_s - v$ Hugoniot (2.18) of the ferroelectric material. The dependence on R can be clearly seen from Figure 4.20 and Table 4.6. As R increases, the electrical boundary condition for the material changes from a short-circuit configuration to an open-circuit configuration. The dependence of material behavior on the electrical boundary conditions has been observed in experiments [14], [27], [38], [51], [54].

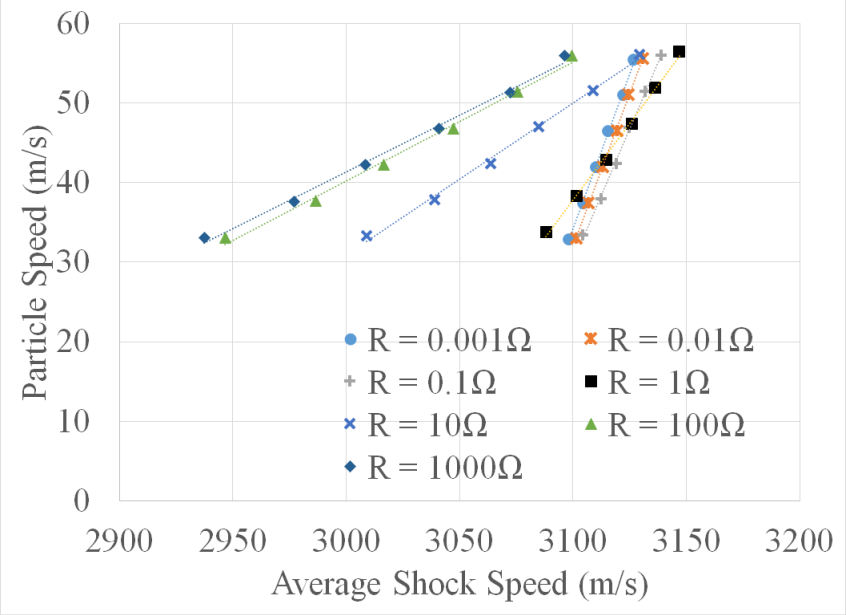

Figure 4.20: Shock speed vs Particle speed Hugoniot of the ferroelectric material for different R in the external circuit. The figure shows a clear difference between short-circuit and open-circuit case.

R	C_0	S
0.001 Ω	3056.18 ms^{-1}	1.28
0.01 Ω	3057.88 ms^{-1}	1.31
0.1 Ω	3054.85 ms^{-1}	1.50
1 Ω	3002.07 ms^{-1}	2.59
10 Ω	2838.44 ms^{-1}	5.25
100 Ω	2731.17 ms^{-1}	6.69
1000 Ω	2711.34 ms^{-1}	7.00

Table 4.6: Variation of Hugoniot parameters of the ferroelectric material for different values of R in the external circuit. The Hugoniot, and hence the material behavior, shows strong dependence on the external circuit which is consistent with experimental observations.

4.5 Conclusions

In this chapter, the nonlinear electro-thermomechanical coupling of a ferroelectric material is explored. The application under consideration is that of a ferroelectric generator, where the nonlinear coupling between electrical, thermal and mechanical responses is exploited to generate a large pulse of power through shock loading. The shock loading induces a ferroelectric to anti-ferroelectric phase transition in the material. A continuum model was developed to study the large deformation dynamic behavior of the material under adiabatic conditions. The analysis is carried out under

the conventional assumption of quasistatic electromagnetic approximation and an added assumption of a sharp moving phase boundary. The motion of the propagating phase boundary is studied through this analysis. The high amplitude stress loading due to shock waves generate a high electric field in the material, leading to formation of surface charges on the propagating phase boundary. Using the conservation laws, Maxwell equations and the second law of thermodynamics, governing equations for the process are derived. Further, an expression for the driving force acting on the phase boundary is derived using the second law.

The expression for the driving force (4.65) contains terms corresponding to electro-thermomechanical coupling of the material. In a classical continuum analysis, the driving force is related to the jump in Eshelby tensor. Here, there are more terms due to the electrical coupling involved. It can be seen that the driving force contains a contribution from the product of electrical conjugates - polarization and electric field - which tries to slow down the phase boundary. There is also a contribution from Maxwell stress introducing volumetric strain into the material. The stress tensor, which appears in the classic Eshelby tensor, is now modified to include the contribution of Maxwell stress. This is consistent with classic electromechanical analysis where the total stress is the combination of Cauchy stress and Maxwell stress. Finally, an added term containing the curvature κ of the phase boundary appears due to the presence of surface charges on the phase boundary. It should be noted that due to the presence of surface charges on the phase boundary, it is difficult to define the exact definition of traction on an arbitrary subdomain containing the phase boundary. Conventionally, the traction is defined as the normal projection of a stress tensor. In a purely thermomechanical analysis, the stress tensor is the Cauchy stress. In this case, due to the electro-thermomechanical coupling, the stress tensor is the sum of Cauchy and Maxwell stress tensors.

A standard canonical problem of plate impact on an axially poled ferroelectric sample is studied. In Section 4.3, a simple uncoupled one-dimensional analysis is conducted before electro-thermomechanical coupling is introduced into the model. A one-dimensional ferroelectric material is considered with the two ends connected by a resistor R. A phase boundary moving at constant speed V is introduced into the system and the current output in the external circuit is studied. The resulting expression of current profile shows an exponential growth achieving a steady value after long time. The analysis sheds light onto different parameters governing the current profile, such as remnant polarization, V, length of the sample, external

resistance R and relative permittivity of the material. The expression is useful in providing qualitative explanations for many experimental observations. A nonlinear electro-thermomechanically coupled model was introduced in Section 4.4. The Helmholtz energy considered was a combination of two components - two welled in polarization and two welled in strain with dependence on temperature. Due to the lack of available kinetic relation data, two classes of kinetic relations were studied. The results obtained showed the exponential profile of the current, consistent with experiments. The current magnitude increases with increasing impact speeds, decreasing sample length, and decreasing R.

Finally, charge profiles obtained by Furnish [34] were recreated through numerical simulations by choosing parameters consistent with available literature data and an stick-exponential slip kinetic relation. It can be seen that the model closely matches the observed charge profiles with correct current output prediction. Shock speed-particle speed Hugoniot relation is also generated by studying different impact speeds and different R in the external circuit. It is observed that the material exhibits a linear relationship between shock speeds and particle velocities. Hugoniot data was generated for seven orders of magnitude of R to study the dependence on boundary conditions. As R increases, the boundary conditions change from short-circuit to open-circuit configuration leading to different material behavior. Parameters characterizing the linear relation are presented in Table 4.6.

Chapter 5

SUMMARY AND FUTURE DIRECTIONS

In this thesis the phenomenon of shock wave propagation is explored in composites and ferroelectric materials. In order to understand the process of scattering in heterogeneous materials, a canonical problem of plate impact on a layered material was studied in Chapter 3. The piecewise linear approximation to the stress-strain Hugoniot allowed collapsing of rarefaction wave fans on to a single wave. This assumption also preserved the nonlinearity of the problem. The choice of piecewise linear stress strain curves allowed a complex problem to be broken down into classes of more tractable Riemann problems. In order to obtain a unique solution, added information was needed to replace linear $U_s - v$ Hugoniot and Lax entropy criteria in this case. It was argued that shocks are dissipative by nature. Hence, a maximally dissipative kinetic relation was chosen to obtain a unique solution to the jump equations.

The solution to the Riemann problem corresponding to the interaction of a shock wave at the interface of two nonlinear layers gives rise to a backward propagating elastic wave and a forward moving shock wave. The speed of the new shock wave is determined by contrast between the properties of the two layers. If the compliant strain of the material ahead of the shock is larger than the neighboring layer, the resulting shock is slower (or weaker). On the other hand, if the contrast between the two adjacent layers is too large, the release wave from the flyer can lead to formation of a spall zone or cause delamination in the material. This has important implications in a design problem where the objective is to achieve shock attenuation. In this case, the design of the laminate should be such that the layers with lesser compliant strain should be at the front while the layers with larger compliant strain should be at the back. However, in order to avoid delamination, the gradient of properties along the length of the laminate should not be too large. In fact, most armor designs are based on this general principle. Other laminates can be designed with periodic layer arrangement designed to capture energy within softer layers.

The analysis presented in this thesis involves many simplifying assumptions for the material model, such as piecewise linear approximation of the Hugoniot, elastic homogeneity of the constituent layers, and an isothermal environment. These

assumptions were made to make the problem accessible, while still being able to capture the complexity of the scattering process. As the next step, extensions can be made in many directions including different modulus in shocked and unshocked regions, different layer densities, different layer moduli and different yield stresses. These extensions can be studied by introducing more classes of Riemann problems into the system. Further, the temperature plays an important role in the process of shock propagation. In order to account for temperature, the analysis needs to modified to a finite-volume shock capturing scheme following the ideas presented in Chapter 4. Finally, in order to extend the problem from a piecewise linear model to a Hugoniot material model, the corresponding Riemann problems will be replaced by Cauchy problems with non-piecewise constant initial conditions. Solutions to these problems are obtained by solving integral equations instead of jump equations for Riemann problems. In this case, the interactions happen within a region of the $X - t$ plane instead of at a point, which further complicates the problem.

The process of shock induced phase transitions and the associated nonlinear electro-thermomechanical coupling of ferroelectric material is studied in Chapter 4. A comprehensive continuum model is developed to study large deformation dynamic behavior of such materials in adiabatic environments. Using conservation laws, Maxwell equations and the second law of thermodynamics, governing equations are derived for the motion of the phase boundary in the material under generalized electromechanical loading. The continuum analysis conducted resulted in a constitutive relation for the Helmholtz energy of the material. Additionally, an expression is derived for the driving force acting on the phase boundary. Aside from traction terms, the driving force has a contribution from electrical terms including volumetric change due to Maxwell stresses and product of electrical conjugates - polarization and electrical field.

A canonical problem of a plate impact on an axially poled ferroelectric material with a resistance R connecting two ends of the material is studied. A one-dimensional uncoupled analysis gives an exponential profile of current output with time. This simple analysis explains the dependence of current on parameters like remnant polarization, speed of the phase boundary, length of the material, external resistance and dielectric permittivity. Numerical simulations conducted for a nonlinearly coupled electro-thermomechanical material model show results consistent with experiments. The $U_s - v$ Hugoniot generated through numerical analysis showed different material response for open and short-circuit boundary conditions. A broad parameter

study is conducted which provides valuable information on current pulse shaping. The peak current magnitude, current rise time and pulse width can be controlled by changing parameters such as external resistance, impact speeds, flyer and target lengths. Further, current profiles can be controlled by changing material properties like dielectric permittivity, remnant polarization and elastic modulus. The material properties can be changed by changing chemical composition through doping.

The analysis presented in Section 4.4 can be extended in many directions. The numerical method to solve the canonical problem of a plate impact on a single layer of ferroelectric material can be extended to study the case of layered materials. This requires adding more Riemann problems and modifying the mesh-update portion of the algorithm to account for the case when the phase boundary gets too close to a material interface. The extension from a homogeneous material to a layered composite provides valuable information into the role of scattering in pulsed power generation process. Additionally, by using different materials (ferroelectric and non-ferroelectric layers) optimal composite design can be explored for pulse modulation. Understanding the role of heterogeneity is important because the samples used in experiments are ceramic in nature. The pulsed power generation process is typically accompanied by pore collapse and the crushing of grains. In order to understand the role of heterogeneity at the mesoscale, it is important to study the interaction of domain walls with heterogeneities. This requires a multiscale formulation. The case of dielectric breakdown also needs to be studied to better understand the decline of current at very high impact speeds. This requires a model for an energy functional associated with volumetric and surface charge distribution in the body.

BIBLIOGRAPHY

[1] R. Abeyaratne and J. Knowles. "Kinetic relations and the propagation of phase boundaries in solids". In: *Archive for Rational Mechanics and Analysis* 114 (2 1991), pp. 119–154.

[2] R. Abeyaratne and J. Knowles. "On the driving traction acting on a surface of strain discontinuity in a continuum". In: *Journal of the Mechanics and Physics of Solids* 38 (3 1990), pp. 345–360.

[3] R. Abeyaratne and J.K. Knowles. "Implications of viscosity and strain-gradient effects for the kinetics of propagating phase boundary in solids". In: *SIAM Journal of Applied Mathematics* 51.5 (1991), pp. 1205–1221.

[4] R. Abeyaratne and J.K. Knowles. "On the propagation of maximally dissipative phase boundaries in solids". In: *Quarterly of Applied Mathematics* 50 (1992), pp. 149–172.

[5] R. Ahluwalia and W. Cao. "Influence of dipolar defects on switching behavior in ferroelectrics". In: *Phys. Rev. B* 63 (1 Dec. 2000), p. 012103. DOI: 10.1103/PhysRevB.63.012103. URL: http://link.aps.org/doi/10.1103/PhysRevB.63.012103.

[6] R. Ahluwalia and W. Cao. "Size dependence of domain patterns in a constrained ferroelectric system". In: *Journal of Applied Physics* 89.12 (2001), pp. 8105–8109.

[7] L.L. Altgilbers et al. *Explosive Pulsed Power*. London: Imperial College Press, 2010.

[8] L. V. Al'tshuler. "Phase transitions in shock waves (review)". In: *Journal of Applied Mechanics and Technical Physics* 19.4 (1978), pp. 496–505. ISSN: 1573-8620. DOI: 10.1007/BF00859398. URL: http://dx.doi.org/10.1007/BF00859398.

[9] R.W. Armstrong, W. Arnold, and F.J. Zerilli. "Dislocation mechanics of shock induced plasticity". In: *Metallurgical and Materials Transactions A* 38 (2007), pp. 2605–2610.

[10] J.R. Asay and M. Shahinpoor. *High-Pressure shock compression of solids*. New York: Springer-Verlag, 1993.

[11] W. Band. "Studies in the theory of shock propagation in solids". In: *Journal of Geophysical Research* 65 (1960), pp. 695–719.

[12] L.M. Barker. "A Model for Stress Wave Propagation in Composite Materials". In: *Journal of Composite Materials* 5.2 (1971), pp. 140–162.

[13] L.M. Barker et al. “Nonlinear viscoelasticity and the evolution of stress waves in laminated composites: a comparison of theory and experiments”. In: *Journal of Appied Mechanics* 41 (1974), pp. 1025–1030.

[14] D. Berlincourt and H.A Krueger. “Domain processes in lead titanate zirconate and barium titanate ceramics”. In: *Journal of Applied Physics* 30 (1959), pp. 1804–1810.

[15] A.V. Bushman et al. *Intense dynamic loading of condensed matter*. CRC Press, 1993.

[16] W. Cao and L.E. Cross. “Theory of tetragonal twin structures in ferroelectric perovskites with a first-order phase transition”. In: *Phys. Rev. B* 44 (1 July 1991), pp. 5–12. DOI: 10.1103/PhysRevB.44.5. URL: http://link.aps.org/doi/10.1103/PhysRevB.44.5.

[17] P. Cermelli, E. Fried, and M. E. Gurtin. “Transport relations for surface integrals arising in the formulation of balance laws for evolving fluid interfaces”. In: *Journal of Fluid Mechanics* 544 (Dec. 2005), pp. 339–351. ISSN: 1469-7645. DOI: 10.1017/S0022112005006695. URL: http://journals.cambridge.org/article_S0022112005006695.

[18] X. Chen, N. Chandra, and A.M. Rajendran. “Analytical solution to the plate impact problem of layered heterogeneous material systems”. In: *International Journal of Solids and Structures* 41.16–17 (2004), pp. 4635–4659.

[19] R.J. Clifton. “On the analysis of elastic/visco-plastic waves of finite strain”. In: *Shock waves and the mechanical properties of solids*. Ed. by J.J. Burke and V. Weiss. Syracuse, NY: Syracuse University Press, 1971, p. 73.

[20] R.E. Cohen and H. Krakauer. “Electronic structure studies of the differences in ferroelectric behavior of $BaTiO_3$ and $PbTiO_3$”. In: *Ferroelectrics* 136.1 (1992), pp. 65–83.

[21] J. Thomas Cutchen. “Polarity Effects and Charge Liberation in Lead Zirconate Titanate Ceramics under High Dynamic Stress”. In: *Journal of Applied Physics* 37.13 (1966), pp. 4745–4750.

[22] D. Damjanovic. In: *Reports on Progress in Physics* 61 (1998), pp. 1267–1324.

[23] L.W. Davison. *Fundamentals of shock wave propagation in solids*. Berlin: Springer, 2008.

[24] A.F. Devonshire. “Theory of barium titanate - Part II”. In: *The London, Edinburgh, and Dublin Philosophical Magazine and Journal of Science* 42.333 (1951), pp. 1065–1079.

[25] A.F. Devonshire. “Theory of barium titanate: Part-I”. In: *The London, Edinburgh, and Dublin Philosophical Magazine and Journal of Science* 40.309 (1949), pp. 1040–1063.

[26] A.F. Devonshire. “Theory of ferroelectrics”. In: *Advances in Physics* 3 (1954), pp. 85–130.

[27] J.J. Dick and J.E. Vorthman. “Effect of electrical state on mechanical and electrical response of a ferroelectric ceramic PZT 95/5 to impact loading”. In: *Journal of Applied Physics* 49.4 (1978), pp. 2494–2498.

[28] G. E. Duvall and R. A. Graham. “Phase transitions under shock-wave loading”. In: *Rev. Mod. Phys.* 49 (3 July 1977), pp. 523–579. DOI: 10.1103/RevModPhys.49.523. URL: http://link.aps.org/doi/10.1103/RevModPhys.49.523.

[29] B. Erzar and P. Forquin. “Experiments and mesoscopic modelling of dynamic testing of concrete”. In: *Mechanics of Materials* 43.9 (2011), pp. 505–527.

[30] Fatuzzo F. and Merz W.J. *Ferroelectricity*. Amsterdam: North Holland, 1967.

[31] I.J. Fritz. “Uniaxial-stress effects in a 95/5 lead zirconate titanate ceramic”. In: *Journal of Applied Physics* 49.9 (1978), pp. 4922–4928.

[32] I.J. Fritz and J.D. Keck. “Pressure-temperature phase diagrams for several modified lead zirconate ceramics”. In: *Journal of Physics and Chemistry of Solids* 39.11 (1978), pp. 1163–1167. ISSN: 0022-3697. DOI: http://dx.doi.org/10.1016/0022-3697(78)90090-2. URL: http://www.sciencedirect.com/science/article/pii/0022369778900902.

[33] A. I. Funtikov and M. N. Pavlovsky. “High-Pressure Shock Compression of Solids VII: Shock Waves and Extreme States of Matter”. In: ed. by V. E. Fortov et al. New York, NY: Springer New York, 2004. Chap. Shock Waves and Polymorphic Phase Transformations in Solids, pp. 197–223. ISBN: 978-1-4757-4048-6. DOI: 10.1007/978-1-4757-4048-6_6. URL: http://dx.doi.org/10.1007/978-1-4757-4048-6_6.

[34] M.D. Furnish et al. “Dynamic electromechanical characterization of axially poled PZT 95/5”. In: *AIP Conference Proceedings* 505.1 (2000), pp. 975–978.

[35] D. Grady. “Scattering as a mechanism for structured shock waves in metals”. In: *Journal of Mechanics and Physics of Solids* 46 (1998), pp. 2017–2038.

[36] D.E. Grady. “Structured shock waves and the fourth power law”. In: *Journal of Applied Physics* 107 (2010), p. 013506.

[37] W.J. Halpin. “Current from a shock loaded short-circuited ferroelectric ceramic disk”. In: *Journal of Applied Physics* 27 (1966), pp. 153–163.

[38] W.J. Halpin. “Resistivity estimates for some shocked ferroelectrics”. In: *Journal of Applied Physics* 39 (1968), pp. 3821–3826.

[39] Hong-Liang Hu and Long-Qing Chen. "Computer simulation of 90 ° ferroelectric domain formation in two-dimensions". In: *Materials Science and Engineering: A* 238.1 (1997). Microstructure Evolution in Bulk Phases F, pp. 182–191. ISSN: 0921-5093. DOI: http://dx.doi.org/10.1016/S0921-5093(97)00453-X. URL: http://www.sciencedirect.com/science/article/pii/S092150939700453X.

[40] R.D. James. "Configurational forces in magnetism with application to the dynamics of a small-scale ferromagnetic shape memory cantilever". In: *Continuum Mechanics and Thermodynamics* 14.1 (2002), pp. 55–86. ISSN: 1432-0959. DOI: 10.1007/s001610100072. URL: http://dx.doi.org/10.1007/s001610100072.

[41] J.N. Johnson and L.M. Barker. "Dislocation dynamics and steady plastic wave profiles in 6061-T6 aluminum". In: *Journal of Applied Physics* 40 (1969), pp. 4321–4334.

[42] F. Jona and G. Shirane. *Ferroelectric crystals*. New York: Dover, 1993.

[43] G.I. Kanel, V.E. Fortov, and S.V. Razorenov. *Shock wave phenomena and the properties of condensed matter*. New York: Springer-Verlag, 2004. ISBN: 978-1-4419-1916-8.

[44] J.K. Knowles. "On the relation between particle velocity and shock wave speed for thermoelastic materials". In: *Shock Waves* 12.2 (2002), pp. 137–144.

[45] A. Kontsos and C.M. Landis. "Phase-field modeling of domain structure energetics and evolution in ferroelectric thin films". In: *Journal of Applied Mechanics* 77 (2010).

[46] E. H. Lee and Wei H. Yang. "On Waves in Composite Materials with Periodic Structure". In: *SIAM Journal on Applied Mathematics* 25.3 (1973), pp. 492–499.

[47] P.G. Lefloch. *Hyperbolic systems of conservation laws: The theory of classical and nonclassical shock waves*. Birkauser, 2002. ISBN: 978-3764366872.

[48] Y. L. Li et al. "Phase-field model of domain structures in ferroelectric thin films". In: *Applied Physics Letters* 78.24 (2001), pp. 3878–3880.

[49] Y.L. Li et al. "Effect of substrate constraint on the stability and evolution of ferroelectric domain structures in thin films". In: *Acta Materialia* 50.2 (2002), pp. 395–411. ISSN: 1359-6454. DOI: http://dx.doi.org/10.1016/S1359-6454(01)00360-3. URL: http://www.sciencedirect.com/science/article/pii/S1359645401003603.

[50] C.D. Lundergan and D.S. Drumheller. "Dispersion of shock waves in composite materials". In: *Shock waves and mechanical properties of solids*. Ed. by J. Burke and V. Weiss. New York: Syracuse University Press, 1971, pp. 141–154.

[51] P. C. Lysne and L. C. Bartel. “Electromechanical response of PZT 65/35 subjected to axial shock loading”. In: *Journal of Applied Physics* 46.1 (1975), pp. 222–229.

[52] P.C. Lysne. “Dielectric breakdown of shock-loaded PZT 65/35”. In: *Journal of Applied Physics* 44.2 (1973), pp. 577–582.

[53] P.C. Lysne. “Prediction of dielectric breakdown in shock loaded ferroelectric ceramics”. In: *Journal of Applied Physics* 46.1 (1975), pp. 230–232.

[54] P.C. Lysne and C.M. Percival. “Electric energy generation by shock compression of ferroelectric ceramics: Normal-mode response of PZT 95/5”. In: *Journal of Appied Physics* 46.4 (1975), pp. 1519–1525.

[55] S.P. Marsh. *LASL shock Hugoniot data*. Berkeley: University of California Press, 1980.

[56] R.J. McQueen et al. “The equation of state of solids from shock wave studies”. In: *High-Velocity Impact Phenomena*. Ed. by R. Kinslow. Academic Press, pp. 293–417. ISBN: 978-0-12-408950-1. DOI: 10.1016/B978-0-12-408950-1.50012-4.

[57] B. Meyer and David Vanderbilt. “*Ab initio* study of ferroelectric domain walls in $PbTiO_3$”. In: *Phys. Rev. B* 65 (10 Mar. 2002), p. 104111. DOI: 10.1103/PhysRevB.65.104111. URL: http://link.aps.org/doi/10.1103/PhysRevB.65.104111.

[58] A. Molinari and G. Ravichandran. “Fundamental structure of steady plastic shock waves in metals”. In: *Journal of Applied Physics* 95 (2004), pp. 1718–1732.

[59] A.J. Moulson and J.M. Herbert. *Electroceramics: Materials, Properties, Applications*. 2nd ed. New York: Wiley, 2003.

[60] Shinji Nambu and Djuniadi A. Sagala. “Domain formation and elastic long-range interaction in ferroelectric perovskites”. In: *Phys. Rev. B* 50 (9 Sept. 1994), pp. 5838–5847. DOI: 10.1103/PhysRevB.50.5838. URL: http://link.aps.org/doi/10.1103/PhysRevB.50.5838.

[61] A.H. Nayfeh. *Wave propagation in layered anisotropic media: with applications to composites*. North Holland, 1995.

[62] J. Niemczura and K. Ravi-Chandar. “On the response of rubbers at high strain rates - II. Shock waves”. In: *Journal of Mechanics and Physics of Solids* 59 (2011), pp. 442–456.

[63] Y. Oved, G.E. Luttwak, and Z. Rosenberg. “Shock wave propagation in layered composites”. In: *Journal of Composite Materials* 12 (1978), pp. 84–96.

[64] Prashant K. Purohit and Kaushik Bhattacharya. "Dynamics of strings made of phase-transforming materials". In: *Journal of the Mechanics and Physics of Solids* 51.3 (2003), pp. 393–424. ISSN: 0022-5096. DOI: http://dx.doi.org/10.1016/S0022-5096(02)00097-2. URL: http://www.sciencedirect.com/science/article/pii/S0022509602000972.

[65] M. Rauls. "Shock wave behavior of particulate composites". PhD thesis. Pasadena, California: California Institute of Technology, 2015.

[66] Z Rosenberg, Y Partom, and Y Yeshurun. "Determination of the Hugoniot elastic limits of differently treated 2024 Al specimens". In: *Journal of Physics D: Applied Physics* 15.7 (1982), p. 1137.

[67] Leonid Ryzhik, George Papanicolaou, and Joseph B. Keller. "Transport equations for elastic and other waves in random media". In: *Wave Motion* 24.4 (1996), pp. 327–370.

[68] J. F. Scott et al. "Device models for PZT/PT, BST/PT, SBT/PT, and SBT/BI ferroelectric memories". In: *Ferroelectrics* 225.1 (1999), pp. 83–90.

[69] R.E. Setchell. "Recent Progress in Understanding the Shock Response of Ferroelectric Ceramics". In: *AIP Conference Proceedings* 620.1 (2002), pp. 191–196.

[70] R.E. Setchell. "Shock wave compression of the ferroelectric ceramic $Pb_{0.99}(Zr_{0.95}Ti_{0.05})_{0.98}Nb_{0.02}O_3$: Depoling currents". In: *Journal of Applied Physics* 97.1, 013507 (2005).

[71] R.E. Setchell. "Shock wave compression of the ferroelectric ceramic $Pb_{0.99}(Zr_{0.95}Ti_{0.05})_{0.98}Nb_{0.02}O_3$: Microstructural effects". In: *Journal of Applied Physics* 101.5, 053525 (2007).

[72] Robert E. Setchell. "Shock wave compression of the ferroelectric ceramic $Pb_{0.99}$ $(Zr_{0.95}Ti_{0.05})_{0.98}Nb_{0.02}O_3$: Hugoniot states and constitutive properties". In: *Journal of Applied Physics* 94.1 (2003), pp. 573–588.

[73] Y. C. Shu and K. Bhattacharya. "Domain patterns and macroscopic behaviour of ferroelectric materials". In: *Philosophical Magazine Part B* 81.12 (2001), pp. 2021–2054.

[74] C.T. Sun, J.D. Achenback, and G. Hermann. "Continuum theory for a laminated medium". In: *Journal of Applied Mechanics* 35 (1968), pp. 467–475.

[75] J.W. Swegle and D. Grady. "Shock viscosity and prediction of shock wave rise times". In: *Journal of Applied Physics* 58 (1985), pp. 692–701.

[76] L. Tan and K. Bhattacharya. "Length scales and pinning of interfaces". In: *Proceedings of the Royal Society London A.* (in press).

[77] Richard Toupin. "The Elastic Dielectric". In: *Indiana University Mathematics Journal* 5 (6 1956), pp. 849–915. ISSN: 0022-2518.

[78] J. C. Valadez, David M. Pisani, and C. S. Lynch. "Coupled effects of hydrostatic pressure and bipolar electric field on the FE-AFE phase transformation in 95/5 PZT". In: *Proc. SPIE, Behavior and Mechanics of Multifunctional Materials and Composites* 8689 (2013),

[79] T.J. Vogler, J.P. Borg, and D. Grady. "On the scaling of steady structured waves in heterogeneous materials". In: *Journal of Applied Physics* 112 (2012), p. 123507.

[80] T.J. Vogler and J.D. Clayton. "Heterogeneous deformation and spall of an extruded tungsten alloy: plate impact experiments and crystal plasticity modeling". In: *Journal of the Mechanics and Physics of Solids* 56.2 (2008), pp. 297–335.

[81] Haiying Wang et al. "Effects of microstructural heterogeneity on the spallation behavior of materials". In: *Journal de Physique IV France* 134 (2006), pp. 903–907.

[82] Jie Wang et al. "Phase-field simulations of ferroelectric/ferroelastic polarization switching". In: *Acta Materialia* 52.3 (2004), pp. 749–764. ISSN: 1359-6454. DOI: http://dx.doi.org/10.1016/j.actamat.2003.10.011. URL: http://www.sciencedirect.com/science/article/pii/S135964540300627X.

[83] N.A. Winfree. "Impact-induced phase transformations in elastic solids : a continuum study including numerical simulations for GeO2". PhD thesis. Pasadena, California: California Institute of Technology, 1999.

[84] Yu Xiao and Kaushik Bhattacharya. "A Continuum Theory of Deformable, Semiconducting Ferroelectrics". In: *Archive for Rational Mechanics and Analysis* 189.1 (2008), pp. 59–95.

[85] Y. Xu. *Ferroelectric materials and their applications*. Amsterdam: North-Holland, 1991.

[86] W. Zhang and K. Bhattacharya. "A computational model of ferroelectric domains. Part I: model formulation and domain switching". In: *Acta Materialia* 53.1 (2005), pp. 185–198. ISSN: 1359-6454. DOI: http://dx.doi.org/10.1016/j.actamat.2004.09.016. URL: http://www.sciencedirect.com/science/article/pii/S1359645404005580.

[87] W. Zhang and K. Bhattacharya. "A computational model of ferroelectric domains. Part II: grain boundaries and defect pinning". In: *Acta Materialia* 53.1 (2005), pp. 199–209. ISSN: 1359-6454. DOI: http://dx.doi.org/10.1016/j.actamat.2004.09.015. URL: http://www.sciencedirect.com/science/article/pii/S1359645404005579.

[88] Xiaoguang Zhong, Thomas Y. Hou, and Philippe G. LeFloch. "Computational Methods for Propagating Phase Boundaries". In: *Journal of Computational Physics* 124.1 (1996), pp. 192–216. ISSN: 0021-9991. DOI: http://dx.doi.

org/10.1006/jcph.1996.0053. URL: http://www.sciencedirect.com/science/article/pii/S0021999196900534.

[89] S. Zhuang, G. Ravichandran, and D. Grady. “An experimental investigation of shock wave propagation in periodically layered composites”. In: *Journal of Mechanics and Physics of Solids* 51 (2003), pp. 245–265.